



Zachodniopomorski
Uniwersytet Technologiczny
w Szczecinie

FACULTY OF CHEMICAL TECHNOLOGY AND
ENGINEERING

Department of Polymer and Biomaterials Science

(Christian Götz)

**Dynamic creep and fatigue properties of novel nano-
structured biomaterials using network structures**

Doctoral dissertation

Doctoral thesis completed under the supervision of

Prof. dr hab. inż. Mirosława El Fray

Co-supervisor:

Prof. dr. Judit Eva Puskas

Szczecin, 2024

Acknowledgments

I would like to express my deepest gratitude to all those who have contributed to the successful completion of my Ph.D. thesis.

First and foremost, I am immensely thankful to my supervisor, Prof. dr hab. inż. Mirosława El Fray, for their unwavering guidance, invaluable insights, and continuous support throughout the research process. Her expertise and encouragement have been instrumental in shaping and finalizing the direction of my work.

I extend my heartfelt thanks to the co-supervisor, Prof. dr. Judit Eva Puskas, for the constructive feedback and valuable suggestions that significantly enhanced the quality of my research.

Furthermore, I am grateful to the Polymer Engineering Department at the Faculty of Applied Science of the University of Bayreuth (Germany) for providing the necessary resources and a conducive academic environment for my research endeavors. The German Science Foundation (under AI 474/12-1) deserves special mention for their financial support, which played a crucial role in the successful execution of this project.

I would like to acknowledge the collaborative efforts of my research colleagues, technical co-workers, and students during my research journey at the Polymer Engineering Department (University of Bayreuth). Their intellectual exchange as well as the wonderful times during and outside the office-hours have enriched my academic and personal experiences. In addition, I owe special thanks to Dr. Goy Teck Lim who always supported me in each phase of my research journey with endless patience and scientific advice.

To my family, friends, and loved ones, thank you for your permanent support, understanding, and patience. Your encouragement has been my pillar of strength throughout this long and challenging journey.

Finally, I express my gratitude to all the participants and individuals who willingly participated in my research, contributing their time and insights to the advancement of knowledge in this field.

This thesis represents the culmination of years of hard work, and I am profoundly thankful to each and every one who has played a role in shaping this academic endeavor.

Thank you.

Abstract:

Due to the documented biocompatibility and the long-lasting experience with using thermoplastic urethanes (TPUs) and Silicones as biomaterials, these are currently qualified as the most widely used biomaterials in medical devices. However, their susceptibility to dynamic fatigue creep is a clear disadvantage. The loss of mechanical properties under oscillatory loading can translate to deteriorated efficiency of the host medical device. For implants such a failure of the device leads to a re-operation, which results in an additional risk for the health of the patient. In order to overcome this issue, the present work pursues different approaches to reduce the dynamic creep of two new classes of thermoplastic elastomers, which are already considered as biocompatible with cells and tissues. Chemically cross-linked poly(aliphatic/aromatic-ester)s multiblock copolymers (PEDs) and poly(isobutylene-b-styrene) (IBS) block copolymers will be investigated. Firstly, the influence of the chemical structure on the respective structure-property relationships is systematically assessed using appropriate test methods. Afterwards, the synergistic effect of nanoscaled additives and chemically cross-linked block copolymers on the dynamic creep properties of these thermoplastic elastomers is presented. Hence, this study shows the successful preparation of IBS polymer nanocomposites. Especially combining dendritic IBS copolymers with carbon black nanoparticles provides thermoplastic elastomers with an excellent overall fatigue performance, outperforming current commercial grades. In summary, this study introduces the addition of nano-additives as a powerful tool towards the production of innovative biomaterials with excellent creep resistance and good *in vitro* as well as *in vivo* biocompatibility.

Streszczenie:

Ze względu na udokumentowaną biokompatybilność oraz wieloletnie doświadczenie w stosowaniu termoplastycznych poliuretanów (TPU) i silikonów jako biomateriałów, zalicza się je obecnie do najpowszechniej stosowanych biomateriałów w wyrobach medycznych. Wyraźną wadą jest jednak ich podatność na dynamiczne pełzanie zmęczeniowe. Utrata właściwości mechanicznych pod obciążeniem oscylacyjnym może przełożyć się na gorszą jakość wyrobu medycznego. W przypadku implantów, powstały defekt wyrobu prowadzi do ponownej operacji, co wiąże się z dodatkowym zagrożeniem dla zdrowia pacjenta. Aby przezwyciężyć ten problem, w niniejszej pracy zastosowano różne podejścia do ograniczenia dynamicznego pełzania dwóch nowych klas elastomerów termoplastycznych, które są uważane za biokompatybilne z komórkami i tkankami. W pracy przedstawiono badania chemicznie usieciowanych kopolimerów multiblokowych poli(alifatyczno/aromatycznych estrów) (PED) i kopolimerów blokowych poli(izobutylenu-b-styrenu) (IBS). Po pierwsze, za pomocą odpowiednich metod badawczych, systematycznie oceniono wpływ budowy chemicznej na poszczególne zależności pomiędzy strukturą a właściwościami mechanicznymi. Następnie przedstawiono synergistyczny wpływ nano dodatków i chemicznie usieciowanych kopolimerów blokowych na właściwości dynamicznego pełzania elastomerów termoplastycznych. Dlatego też niniejsza praca potwierdza skuteczność tak wytworzonych nanokompozytów polimerowych IBS do zmniejszenia pełzania zmęczeniowego. Zwłaszcza dzięki połączeniu dendrytycznych kopolimerów IBS z nanocząsteczkami sadzy otrzymano elastomery termoplastyczne o doskonałej ogólnej wytrzymałości zmęczeniowej, przewyższającej obecnie komercyjnie dostępne biomateriały. Podsumowując, w niniejszej pracy udowodniono, że dodanie nanomateriałów jest skutecznym sposobem uzyskania innowacyjnych biomateriałów o doskonałej odporności na pełzanie i dobrej biokompatybilności *in vitro* i *in vivo*.

Kurzfassung:

Aufgrund der belegten Biocompatibilität und der langjährigen Erfahrung mit Thermoplastischen Urethanen (TPUs) und Silikonem als Biomaterialien, werden diese derzeit am häufigsten in Medizinprodukten verwendet. Ein Nachteil des Einsatzes dieser Materialien ist jedoch deren Ermüdungsverhalten unter dynamischer Belastung. Während der Anwendung an dem Patienten führt dieses Verhalten zu dem Verlust der mechanischen Eigenschaften. Bei Implantaten erfordert solch ein Materialversagen meist eine Re-Operation des Patienten, was mit einem zusätzlichen gesundheitlichen Risiko einhergeht. Um dieses Problem zu lösen, verfolgt diese Arbeit verschiedene Ansätze zur Reduzierung des dynamischen Kriechens. Zwei neuen Klassen von thermoplastischen Elastomeren, welche ebenfalls als sehr biokompatibel gelten sind Gegenstände der Untersuchungen. Diese chemisch vernetzte Poly (aliphatische / aromatische Ester) Multiblock-Copolymere (PEDs) und Poly (Isobutylene-b-styrol) (IBS) –Blockcopolymeren werden in dieser Studie untersucht. Zuerst wird mit Hilfe geeigneter Prüfmethode systematisch der Einfluss des chemischen Netzwerks auf die jeweiligen Struktur-Eigenschaftsbeziehungen betrachtet. Im Anschluss wird der synergetische Effekt von nanoskaligen Additiven und chemisch vernetzten Blockcopolymeren auf das dynamische Kriechverhalten der thermoplastischen Elastomere dargestellt. Diese Studie zeigt somit die erfolgreiche Herstellung von IBS Polymer-Nanokompositen. Besonders die Kombination der dendritischen IBS-Copolymere mit Ruß-Nanopartikeln führt zu einem hervorragendem Ermüdungsverhalten, welches das der kommerziellen Biomaterialien übertrifft. Zusammenfassend demonstriert diese Studie, dass die Verwendung von Nano-Additiven zur Verbesserung der Kriechbeständigkeit als eine sehr gute Möglichkeit angesehen werden kann, um innovative Biomaterialien mit guter *in vitro* sowie *in vivo*-Biokompatibilität herzustellen.

Table of contents

1	Introduction	1
1.1	Motivation and problem statement	1
1.2	Structure of the work	3
2	State of the art	4
2.1	Investigations of fatigue	4
2.1.1	Fatigue of materials and constructions	4
2.1.2	Approaches to analyze the mechanical fatigue properties	5
2.2	Biomaterials	14
2.2.1	Biomaterials used for medical applications	14
2.2.2	Elastomeric biomaterials	15
2.2.3	Modification of the mechanical performance of elastomers / biomaterials	21
2.3	Fatigue of polymeric biomaterials	22
3	Objective and strategy	26
4	Materials	27
4.1	Poly(aliphatic/aromatic-ester)s multiblock copolymers (PEDs)	27
4.2	Poly(isobutylene- <i>b</i> -styrene) (IBS) block copolymers	27
4.3	Benchmarking materials	28
4.4	Nano-particles	29
5	Experimental procedure	30
5.1	Sample preparation	30
5.1.1	Poly(aliphatic/aromatic-ester)s (PEDs)	30
5.1.2	Poly(isobutylene- <i>b</i> -styrene) (IBS) block copolymers	30
5.1.3	Composite materials	31
5.1.4	Benchmarking materials	32
5.2	Morphological characterization	32
5.2.1	Transmission electron microscopy (TEM)	32
5.2.2	Atomic force microscopy (AFM)	33
5.3	Thermal characterization	33
5.3.1	Differential scanning calorimetry	33
5.3.2	Dynamic mechanical thermal analysis (DMTA)	33
5.3.3	Thermal gravimetric analysis (TGA)	33
5.4	Mechanical characterization	33

5.4.1	Quasi-static mechanical testing	33
5.4.2	Dynamic fatigue testing.....	34
6	Results and discussion.....	35
6.1	Influence of e-beam cross-linking on fatigue properties of Poly(aliphatic/aromatic-ester) copolymers (based on [178])	35
6.1.1	Polymer morphology.....	35
6.1.2	Thermal properties.....	36
6.1.3	Mechanical characterization	38
6.1.4	Summary	45
6.2	Influence of a chemical network structure on the material performance of (soft) polyisobutylene-based thermoplastic elastomers (based on [188]).....	47
6.2.1	Polymer morphology.....	48
6.2.2	Thermal properties.....	49
6.2.3	Mechanical characterization	51
6.2.4	Summary	57
6.3	Influence of a secondary network structure on the material performance of dendritic polyisobutylene-based thermoplastic elastomers using nano-scaled additives (based on [199] and [200])	59
6.3.1	Composites – carbon black.....	59
6.3.2	Composites – nanoclay.....	73
7	Conclusions.....	79
8	Outlook.....	81
9	Bibliography	83
10	Curriculum Vitae.....	89
11	List of publications.....	90

List of abbreviations:

1-D	1-dimensional
AFM	Atomic force microscopy
CB	Carbon black
da/dN	Crack growth rate
$\Delta\varepsilon$	Absolute creep
ΔK	Stress intensity factor
D_IBS	Dendritic poly(isobutylene-b-styrene) block copolymers
DLA	Dilinoleic acid
DMTA	Dynamic mechanical thermal analysis
DSC	Differential scanning calorimetry
ε_d	Dynamic creep
E	Young's modulus
E_{dyn}	Dynamic Young's modulus
E'	Storage modulus
E''	Loss modulus
FDA	Food and Drug Administration
IBS	Poly(isobutylene-b-styrene) block copolymers
kGy	KiloGray, where one Gray is defined as one joule per kilogram
L_SIBS	Linear poly(isobutylene-b-styrene) block copolymer
M_n	Number-averaged molecular weight (M_n)
NC	Nanoclay
PBT	Poly(butylene terephthalate)
D	Disparity index
PDMS	Poly(dimethyl siloxane)
PED	Poly(aliphatic/aromatic-ester)
PEEK	Poly(ether-ether-kethone)
PIB	Polyisobutylene
PMS	Para-methyl styrene
PS	Polystyrene
PTFE	Poly(tetrafluoroethylene)
PTMO	Poly(tetramethylene oxide)
SAXS	Small angle x-ray scattering
SEM	Scanning electron microscopy
σ_c	Critical stress
σ_{ult}	Ultimate tensile strength
SIBS	Poly(styrene-b-isobutylene-b-styrene) block copolymer
SILT	Stepwise increasing load test
SIST	Stepwise increasing strain test
SLT	Single load test
$\tan \delta$	Damping factor
TEM	Transmission electron microscopy
T_g	Glass transition temperature
TGA	Thermal gravimetric analysis
TPU	Thermoplastic polyurethane

TPE	Thermoplastic elastomer
UHMWPE	Ultra high molecular weight polyethylene
UTS	Ultimate tensile strength
WAXS	Wide angle x-ray scattering

1 Introduction

1.1 Motivation and problem statement

The global medical device industry is currently estimated to be between US\$ 220 and \$ 250 billion in value and continues to grow at a healthy rate despite many economic downturns or slowdowns. The National University of Ireland Galway showed the development of the medical device sector to be grown from about US\$ 100 billion in 2000 to almost US\$ 440 billion by 2018 [1;2] as shown in Figure 1.1.

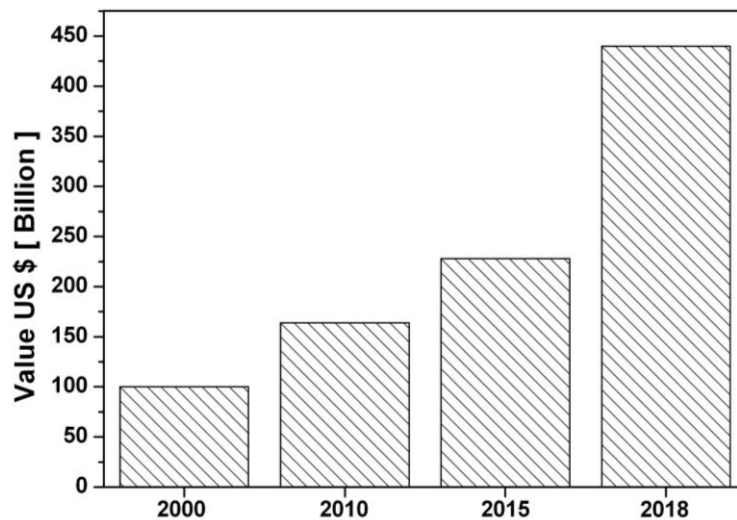


Figure 1.1: Development of the global medical device market from 2000 until 2018.

Recent investigations of the global medical device market showed in 2022 the medical device market was estimated to be at US\$ 512.29 billion and is expected to grow up to US\$ 799.67 billion until 2030 [3].

The global market for medical devices can be divided into four main regions, which are highlighted in Figure 1.2.

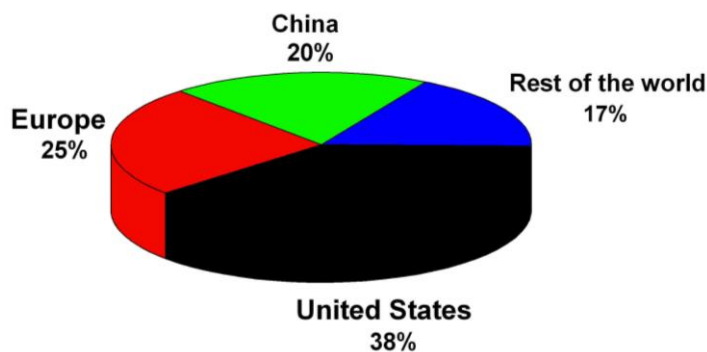


Figure 1.2: The global medical device market share by region.

The United States are the global market leader with 38 % of the market share, followed by Western Europe (25 %) and China (15 %) [1;2]. The remaining 17 % are distributed between the rest of the world, including Japan, India and Latin America. A major contributing factor to this rapid development of the medical device market is the ongoing growth of the world

population. The Population Reference Bureau predicts that in 2050 close to 10 billion people will live all over the world [4]. Besides the increasing population, the demand for health care and medical devices will be further influenced by the demographic development of the world population. The amount of people over 65 years will dramatically increase within the next 10 to 20 years [4]. Therefore, more and affordable healthcare diagnostics and surgical procedures like cardiovascular and orthopedic operation will be required not only for the Western world. For the interest of public safety, these new medical devices are expected to be safer in cutting down hospital stays and reducing the rate of infections during and after treatment, thereby giving patients a better healthcare and a speedier recovery to a productive life.

In the midst of all the development and documented growth in the medical device industry around the globe, a “medical crisis” is brewing that can cripple many economies if left unchecked. It is the fight against the different types of cancers, including breast cancer. Unfortunately, breast cancer is the most common cancer diagnosed among German women in recent years [5], with a projected incidence rate of 158 cases per 100,000 people in 2016, that is alarmingly higher than in many other parts of Europe, USA and the world. With that, more than 71.000 new cases of invasive breast cancer have been diagnosed in women in Germany already for the year 2019 [6] and the amount is still increasing.

Many of these women would consider to undergo breast reconstruction, where the only prostheses available to them in the market today are made of a silicone rubber shell that is filled with either saline or silicone gel. Although no medical device is 100 % safe and effective [7], the complications associated with silicone rubber breast prostheses are numerous especially for breast reconstruction patients, which include gel bleed, capsular contracture, implant calcification, hematoma, necrosis and others [8, 9, 10, 11, 12, 13, 14, 15, 16, 17, 18]. Those complications do not change because there is no alternative surgery or medical device available on the market. The severity of these complications can result in a reoperation to remove or replace the implants over the life span of the patients [19]. In addition to these breast reconstruction patients, there are 279,000 individuals who opted for breast augmentation as a cosmetic procedure in USA and have to bear with the material deficiency of silicone rubber breast prosthesis, as reported by the American Society of Plastic Surgeons in 2015 [20].

A contributing reason for the poor performance of these implants is the cyclic loading experienced by them due to our body movement that fatigue cracks can develop and grow in the silicone rubber shell to form more convenient pathways for more gel bleed. In the extreme case, the fatigue crack growth can lead to an eventual rupture of the implant. While damages to implants can be detected by mammography screening and/or magnetic resonance imaging, ruptures in silicone gel-filled implants are known to be more difficult to identify than saline-filled ones [7]. During the course of implantation, the silicone rubber shell can be subjected to abrasion wear and tear to negatively impact its mechanical stability [21].

While silicone rubber has been extensively used as the material of choice by the biomedical industry for implants and biomedical devices, the unique problems in the design of gel-filled silicone rubber breast prosthesis has called for better alternative shell materials integrated with specific barrier technologies to resist fatigue damage and reduce the occurrence of gel bleed. This above described “medical crisis” in its worst case where the failure of implants or grafts would require reoperation and can lead to the loss of human lives if not discovered earlier. Currently, thermoplastic polyurethanes (TPUs) and silicones are the most commonly used biomaterials for artificial tendons and breast implants. The inherent viscoelastic nature of polymers, like creep, is regarded as a disadvantage for biomaterials, due to the loss of mechanical properties or degradation under oscillatory loading during the course of usage. However, the investigation of the fatigue behavior of polymers can be a complex challenge. Unlike ceramics, metals and conventional composites, the conventional long-term creep testing approach needs to be tailored or redesigned for polymers, like elastomers and

thermoplastic elastomers (TPE), since the ductility and compliance of polymers can be several orders higher than those of traditional materials.

1.2 Structure of the work

The work is structured into several main chapters. After the Introduction presented in Chapter 1, an overview of the theoretical background is provided in Chapter 2. General aspects concerning the fatigue of materials and measuring techniques are summarized. Subsequently, the state-of-the-art of biomaterials used for medical applications, elastomeric biomaterials, and approaches on improving their mechanical performance is presented. Finally, different methods and approaches to evaluate the fatigue properties of biomaterials are summarized. The following section (Chapter 3) defines the aim of the work and provides the research hypothesis, before Chapter 4 and 5 describe the different materials and the experimental procedures used in this work, respectively. Chapter 6 includes all experimental results and their discussion, before Chapter 7 presents an overall summary of the work, while Chapter 8 discusses future steps in developing innovative biomaterials using nano-scaled network structures.

2 State of the art

In the following chapters, an overview about different fatigue measurement approaches, biomaterials, and fatigue of biomaterials will be given. The first part of the overview covers general issues about fatigue testing and different approaches to analyze the mechanical fatigue properties. Afterwards, currently used biomaterials, their specific applications and properties will be presented. The strategies on how to improve the mechanical performance of elastomeric materials and biomaterials will also be discussed. In the last part, approaches on how to investigate the fatigue behavior of polymeric biomaterials will be shown. Finally, the need for further developments of current methods to evaluate the fatigue performance of biomaterials will be reviewed in detail.

2.1 Investigations of fatigue

2.1.1 Fatigue of materials and constructions

The reliability of device components is a big concern for many applications for safety reasons and can depend on several critical parameters. Especially for long-term applications, the materials of choice are responsible for the lifetime of a certain component to affect the reliability of the overall structure or system. This has motivated engineers and material scientists to focus on the fatigue performance of materials [22], as demonstrated by the replacement cost of approximately US\$ 100 billion in 2003 from the pre-mature failure of materials in certain man-made constructions and products [23]. Therefore, the fatigue limit seems to be one of the most quality-sensitive property of engineering materials, because it is nearly impossible to account for all the different factors that can impact the fatigue process of materials [24]. To begin with, most engineering materials show some forms of inhomogeneities, which can lead to large deviations in fatigue life tests, despite the same batch of material, testing methodology and environmental conditions were applied [24]. Even with these multitudes of factors, companies developing products still bear the social responsibility to ensure the quality and safety of these products for the public benefit. So, testing the fatigue response of materials under real-life or simulated loading conditions provides the important key to estimate the lifetime of products. This and an in-depth understanding of structure-property relationships of materials lead to the development of high quality and safer products. To achieve the aforementioned, one specific test would not be sufficient, but rather a combination of mechanical fatigue testing approaches, physical characterization (like thermal analysis), and morphological examination of the materials would be required for fruitful outcomes [24].

As already mentioned, the fatigue problem can be complex and depends on the type of material, structural design, production variables, load spectrum, and environments. The *a priori* prediction of the fatigue performance of a material or any construction involves a series of analytical and experimental procedures with a set of reasonable assumptions made for simplification. This means that the accuracy of the final prediction can remain limited, and then it may be necessary to apply statistical tools to account for randomness. The reliability of predictions should be carefully evaluated. It was reiterated in [25] that a physical understanding of the fatigue phenomena is essential for the evaluation of fatigue predictions. Without some satisfactory understanding of all physical or material aspects involved, predictions of the fatigue behavior of any construction or product may become futile.

2.1.2 Approaches to analyze the mechanical fatigue properties

2.1.2.1 Wöhler-Curves (S/N-Curves)

In the 19th century, Wöhler carried out his experiments to obtain $\sigma - N$ curves, which for a long time, were called Wöhler curves. Later, during the 20th century, a huge number of fatigue tests were done to produce numerous $\sigma - N$ curves. First, it was common to use rotating beam tests on un-notched specimens with a constant mean stress and amplitude. This was followed by the production of fatigue-testing machines for loading in tension, torsion, and bending until 1940. Today, equipment is used, inducing cyclic loading by mechanical or hydraulic systems, which established high frequency fatigue tests. Figure 2.1 depicts a scheme of a typical $\sigma - N$ curve and its characteristics.

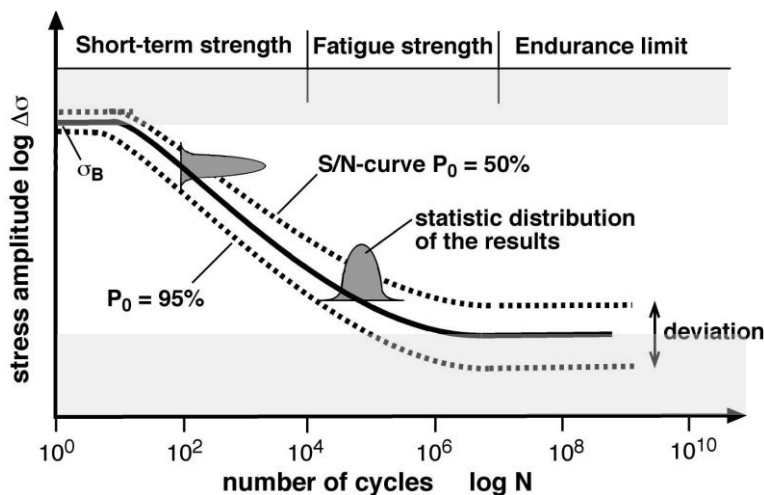


Figure 2.1: Schematic $\sigma - N$ curve showing the short-term strength, fatigue strength and the endurance limit.

When looking at low stress amplitudes (high-cycle fatigue), the $\sigma - N$ curve shows a horizontal asymptote, which ascribes the lower limit, where no fatigue failure is expected even after large numbers of loading cycles. This lower limit of the $\sigma - N$ curve is called the fatigue limit/strength. Similar to the lower limit, a second horizontal asymptote can be observed for large stress amplitudes (low-cycle fatigue). Thus, if failure does not occur in the first cycle, e.g. when the load exceeds the quasi-static strength (σ_B), then the fatigue life can be as long as several hundreds of cycles.

The above described short fatigue life is interesting only for structures/materials with load spectra formed by small numbers of severe loading cycles. For instance, this is the case with high-pressure vessels. For these applications, it became more interesting to investigate the influence of cyclic straining, which in the '60s led to the appearance of $\epsilon - N$ curves, where ϵ is the relative strain. Similar to $\sigma - N$ curves, which have varying stress amplitudes, $\epsilon - N$ curves have a region of short-term strength which can also be determined, whereby macroplastic deformation occurs in each cycle. Furthermore, when $\epsilon - N$ curves were plotted in the low-cycle regime on the log-log scale, it turned out to be a linear function (see Eq. 2.1), known as the Coffin-Manson relation [26, 27]:

$$\epsilon_a N^\beta = \text{const.} \quad \text{Eq. 2.1}$$

with ϵ_a , N and β representing the strain amplitude, number of cycles and an experimental constant, respectively.

In contrast to the high stress or strain amplitudes, the process of macroplastic deformation does not occur when looking at lower stress/strain amplitudes. Hence, this kind of fatigue phenomenon is called high-cycle fatigue (see Figure 2.1) and scientists assume that cyclic deformations on the macroscale are still elastic and recoverable [28]. From the work with $\sigma - N$ curves, two interesting questions arise:

- Is it possible to consider high- and low-cycle fatigue as similar fatigue phenomena?
- What is the physical meaning of the fatigue limit?

To answer the first question correctly, one should keep in mind that crack initiation and crack propagation are both significant for the fatigue life and will be described in Chapter 2.1.2.2. In the case of high-cycle fatigue and the presence of the fatigue limit, the process of crack initiation can very easily be affected by many characteristics of the material surface, like surface roughness, surface damage, surface treatments, soft surface layers, and residual surface stresses. But in general, these characteristics are overruled when the low-cycle fatigue is considered, as plastic deformations on the material surface occur anyway. Furthermore, under the condition of low-cycle fatigue, the propagation of macrocracks is rather limited due to the fact that even small cracks may lead to fracture for high levels of stresses.

For $\sigma - N$ curves, it is very important to mention the fatigue limit of a material or structure, which according to its formal definition, is the stress amplitude when the fatigue life becomes infinite. But from the point of view of an engineer, the fatigue limit should be defined as the highest stress amplitude without fracture after very large numbers of loading cycles. Hence, the design levels of stresses must remain below the fatigue limit in order to obtain safe operation [28].

The indicated two definitions for the fatigue limit do not refer to the physical aspects of the fatigue phenomenon. In order to answer the previously mentioned second question, a more physically-based definition should be established considering microcracks. Generally, one can state, if no microcracks are initiated, there should be no fatigue failures which occur. However, it is possible that cyclic slip occurs for stress amplitudes just below the fatigue limit, and initiates several microcracks, but the growth of said microcracks will be stopped. In all, the fatigue limit should be regarded as the threshold stress amplitude required for the nucleation of a microcrack and its subsequent propagation into a macrocrack.

2.1.2.2 Fatigue crack propagation

As previously described, in former times fatigue damage was associated with a mysterious crystallizing of a fibrous structure, and was not defined in physical terms. In the first half of the 20th century, cyclic slip was considered to be essential for microcrack initiation. In 1933, Gough postulated that fatigue crack initiation is a consequence of exceeding the limit of local strain hardening [29]. This idea was picked up first by Orowan and later by Head to obtain an equation for fatigue crack growth [30, 31].

In 1955, Stroh [32] started to analyze the stress field around a piled-up group of dislocations and claimed that local stress can become sufficiently high to cause local cleavage. From that point of view, it was difficult for them to understand why high local stresses cannot be relaxed near the material surface by plastic deformation in a basically ductile material. Therefore, the ductility exhausting theory did not become a credible crack initiation model, until striations were detected in the late 50s, which indicated that crack propagation occurs in a cycle-by-cycle sequence instead of jumps after intervals of cycles required for an increasing strain-hardening mechanism [33, 34]. Based on the intersecting slip systems [35] and on the generation of vacancies [36] interesting dislocation models were proposed by Cottrell, Hull and Mott and several papers of historical interest were collected by Mott and Averbach [36; 37]. It was the microscopic work of Forsyth [38] on extrusions and intrusions in slip bands, which established the fundamental aspects of the process of fatigue crack initiation:

- the significance of the free material surface,
- the irreversibility of cyclic slip, and
- the environmental effects on microcrack initiation.

It was described that microcracks usually start on the free surface of the material, for notched as well as unnotched specimens with nominally homogeneous distributions of stresses tested under cyclic tension. The restraint on cyclic slip is lower than inside the material because of the presence of the free surface. Furthermore, Backofen also showed that microcracks can start more easily in slip bands with slip displacements normal to the material surface [39]. From these works, it was concluded that there are two main reasons for the irreversibility of cyclic slip:

- not all dislocations return to their original positions because of (cyclic) strain hardening and,
- the new created surface of the material (slip steps) is especially for metal surfaces rapidly covered with a thin oxide layer or some chemisorptions of foreign atoms of the environment.

Furthermore, these conclusions led to the valid and important understanding that fatigue crack initiation is a surface phenomenon.

In general, the fatigue life under cyclic loading can be distinguished into two phases: the crack-initiation life, and a period of crack propagation until fracture (Figure 2.2).

The first phase can cover a large percentage of the fatigue life under the conditions of high-cycle fatigue, for example, when stress amplitudes just above the fatigue limit are applied. Alternatively, for higher stress amplitudes, the part of crack propagation can be mainly responsible for the fatigue life. Hence, a special problem evolved: how to define the transition from the period of crack initiation to the period of crack propagation.

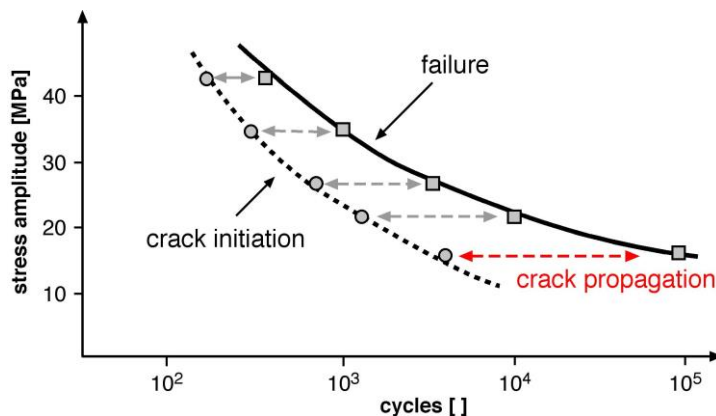


Figure 2.2: Different stages of fatigue until fracture of the sample (crack initiation, crack propagation and failure, acc. [40, 41]).

With the introduction of the stress intensity factor by Irwin and Paris [40, 41], a correlation between the crack propagation rate da/dN and the range of the stress intensity factor, ΔK at the crack tip was established in the late 60s:

$$\frac{da}{dN} = C(\Delta K)^m \quad \text{Eq. 2.2}$$

where C and m represent experimental constants, which are not yet readily associated with the physical properties of the material but are suitable to characterize its crack growth resistance.

Furthermore, it has to be noted that the correlation between da/dN and ΔK strongly depends on the stress ratio

$$R = \frac{\Delta K_{\min}}{\Delta K_{\max}} \quad \text{Eq. 2.3}$$

Figure 2.3 shows a scheme of a typical result of crack propagation tests, which reveals systematic deviations from the Paris equation for relatively high and low values of ΔK . These deviations lead to the split of the da/dN - ΔK dependencies into three major regions also depicted on Figure 2.3.

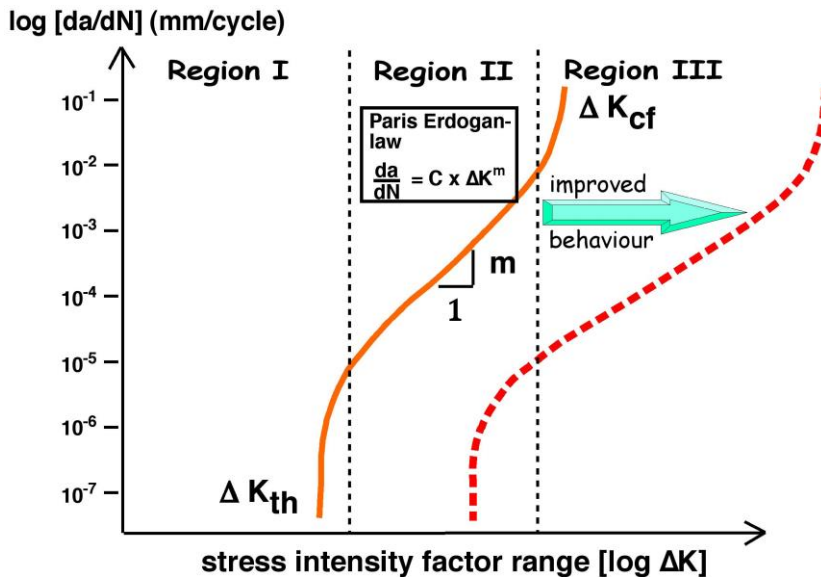


Figure 2.3: The three regions of crack growth: (I) threshold region, (II) Paris region, (II) critical region (acc. [40, 41]).

The vertical asymptote on the upper boundary of Region III appears to be logical. When K_{\max} is as great as or even greater than the fracture toughness of a material (either K_C or K_{1C}), quasi-static failure occurs, which prevents the process of fatigue crack propagation. Using the viewpoint of fracture mechanics, the lower boundary in Region I is not so obvious, but the presence of a singular stress field suggests the formation of a microplasticity at the crack tip, which leads to crack propagation in the material.

In summary, it is important to mention that for the determination of the fatigue limit using fatigue tests, a large number of cycles is necessary. Therefore, they are very time consuming and, thus, expensive, because in order to obtain the statistical variability of the fatigue limit, a reasonably large number of tests need to be performed. Some statistical procedures for this purpose were standardized, e.g., the Staircase method (steady increase of the load, when samples do not fracture) [42]. Using this method, an approximate determination of the fatigue limit can be realized with a small number of specimens by increasing the stress amplitude in small steps [43].

However, from the previous discussion on the fatigue phenomenon and with respect to the complex topic of crack initiation and propagation, it can be concluded that correlations as discussed above are up to now elusive. Therefore, it would be very interesting to have a measurement method, which besides recording cycles to fracture, is also able to monitor changes in the material during the dynamic loading.

2.1.2.3 Hysteresis measurements

For all of the benefits and information gleaned from the previous fatigue tests (Fatigue crack propagation and S-N curves), there still remain several drawbacks. Due to the inherently destructive nature of these tests, many samples are required for complete testing. In addition, it is not uncommon for a single sample to require more than 24 hours before it is completed, leading to the aforementioned long testing times. Finally, while immensely useful, traditional fatigue tests reveal limited information about the structural changes occurring during sample failure.

Therefore, in 1988 Renz et al. [44] introduced a new fatigue test named the “hysteresis method”. Beside the cycles to fracture, this method provides information about the structure of a sample while being tested, and hence requires less destructive tests and can be conducted in less time.

The hysteresis analysis is based on the theory of viscoelasticity of polymeric materials. Due to the viscoelastic nature of polymers, imposing a sinusoidal deformation (stress/strain) results in the development of a time-delayed sinusoidal strain/stress on the sample (Figure 2.4). The resulting stress wave can be decomposed into two waves; one in-phase and the other 90° out-of-phase with the strain wave. When these tests are conducted in the extensional mode of deformation, the in-phase component is described as the storage modulus (E' for extension – Eq. 2.4), while the out-of-phase component is the loss modulus (E'' for extension – Eq. 2.5) [45]. Traditionally, these values are reported against frequency:

$$E'(\omega) = \frac{\text{stress (in – phase)}}{\text{strain (maximum)}} = \frac{\sigma_0' \sin(\omega t)}{\varepsilon_0} \quad \text{Eq. 2.4}$$

$$E''(\omega) = \frac{\text{stress (out – of – phase)}}{\text{strain (maximum)}} = \frac{\sigma_0'' \cos(\omega t)}{\varepsilon_0} \quad \text{Eq. 2.5}$$

where ε_0 is the strain amplitude, σ_0' , the in-phase stress component, σ_0'' , the out-of-phase stress component, ω , the frequency of oscillation and t represents time. When plotting stress and strain versus time without decomposing them into an in-phase and out-of-phase component, the two sinusoidal curves oscillate at the same frequency, but are shifted by a phase angle, δ , for a single cycle. By plotting stress versus strain, this phase angle manifests itself by creating an ovoid shape, or “hysteresis loop”. Hookean solids, e.g. metals, have no delay, and consequently produce a “hysteresis loop” as a straight line, while Newtonian fluids are 90° out-of-phase and therefore, produce a perfect circle-like hysteresis loop. Figure 2.4 demonstrates an ideal strain controlled hysteresis loop, where the delay in stress is caused by the damping properties of the polymeric material [46].

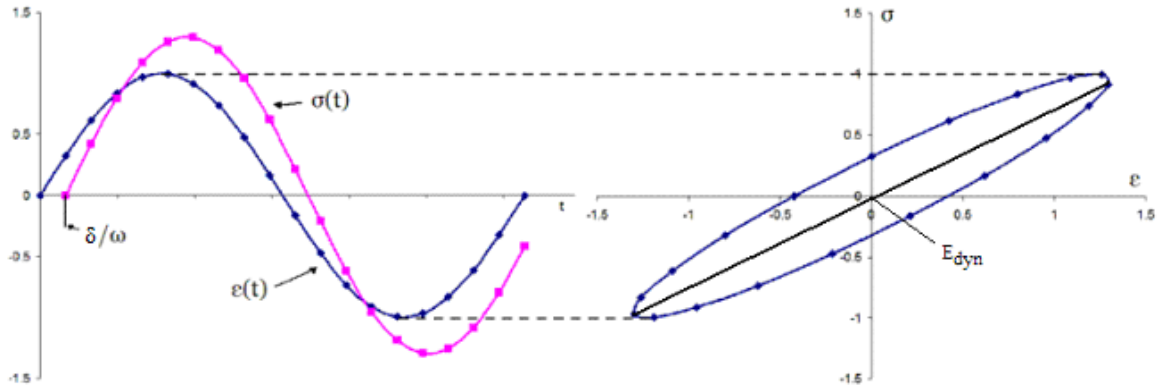


Figure 2.4: Representative Hysteresis loops. Left Hand Side – Strain controlled ($\varepsilon(t)$) measurements leads the delayed (δ/ω – phase angle divided by frequency for plotting on a time scale) stress measurement ($\sigma(t)$). Right Hand Side – A hysteresis loop is created when plotting stress versus strain.

From the maximum, minimum and mid points of the stress and strain data depicted in Figure 2.5 (maximum stress - σ_{max} , minimum stress - σ_{min} , midpoint stress - σ_m , maximum strain - ε_{max} , minimum strain - ε_{min} , midpoint strain - ε_m), the overall, upper and lower dynamic modulus can be defined by Eq. 2.6, Eq. 2.7 and Eq. 2.8, respectively [47]:

$$E_{dyn,0} = (\sigma_{max} - \sigma_{min}) / (\varepsilon_{max} - \varepsilon_{min}) \quad \text{Eq. 2.6}$$

$$E_{dyn,U} = (\sigma_{max} - \sigma_m) / (\varepsilon_{max} - \varepsilon_m) \quad \text{Eq. 2.7}$$

$$E_{dyn,L} = (\sigma_{min} - \sigma_m) / (\varepsilon_{min} - \varepsilon_m) \quad \text{Eq. 2.8}$$

For tests done in tension mode, overall modulus is the most important parameter of these characteristics and will be referred to simply as E_{dyn} , the dynamic modulus.

The stiffness of a material, as determined by Eq. 2.9, is the ratio of the upper and lower dynamic moduli and represents a good indicator for internal damage. In case of a symmetric hysteresis loop, the stiffness is well described by the E_{dyn} .

$$E_{dyn,U} / E_{dyn,L} = \tan\alpha_U / \tan\alpha_L \quad \text{Eq. 2.9}$$

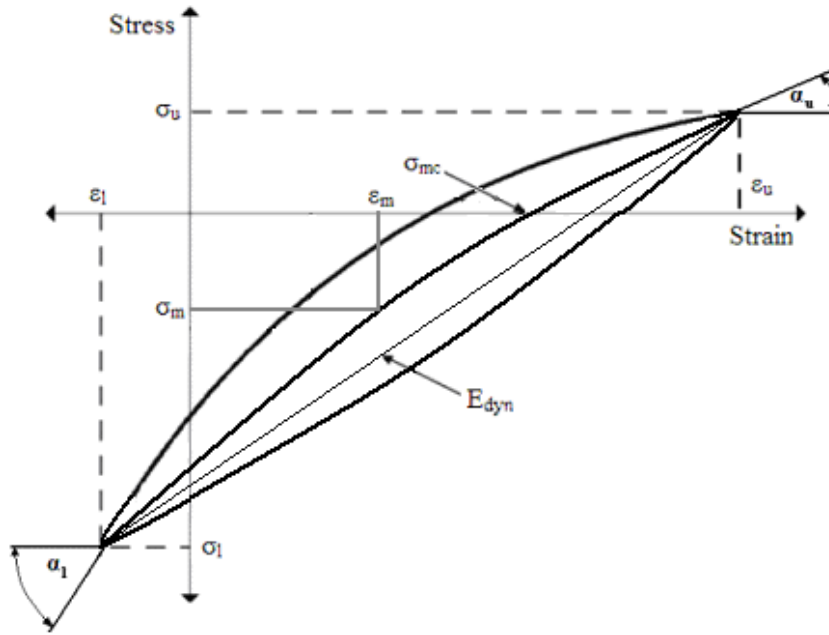


Figure 2.5: Determination of the dynamic modulus from the hysteresis loop. σ_{mc} represents the curve of the midpoint for stress as determined by the average of the upper and lower stress as a function of strain.

Using hysteresis loops, Orth et al., [47] further provided equations for the loss energy, w_L (Eq. 2.10) and stored energy, w_S (Eq. 2.11) as a function of area. In extension, the damping factor of the material, representing the ratio of loss energy over stored energy, is represented by Eq. 2.12. By comparison, in torsion, damping is represented by the value of $\tan \delta$, as described in Eq. 2.13.

$$w_L = \frac{1}{2} \left(\oint \sigma d\epsilon - \oint \epsilon d\sigma \right) \quad \text{Eq. 2.10}$$

$$w_S = \oint \sigma_{mc} d\epsilon \quad \text{Eq. 2.11}$$

$$\text{Extensional Damping} = w_L/w_S \quad \text{Eq. 2.12}$$

$$\tan \delta = \frac{E''}{E'} \quad \text{Eq. 2.13}$$

The basis of the traditional fatigue test is the determination of the fatigue limit. The definition of the fatigue limit is the largest stress/strain at which failure will never occur via cyclic loading. Once found, in-depth analysis close to the point of failure for a sample is beneficial to examine how physical properties change when failure occurs. Hence, a method is provided to predict failure and examine samples under a “worst case” scenario. The analysis of the hysteresis loops therefore involves first the determination of the fatigue limit and secondly long-term analysis at the fatigue limit. Of course, these tests can either be conducted in tension, compression or a combination of compression and tension as defined by the load ratio, R . The R -ratio is defined as the ratio between lower stress and upper stress limit.

In addition, the hysteresis method can be carried out either in the strain-controlled, or stress-controlled mode. The former employs a sinusoidal deformation applied to the sample, and the resulting stress is recorded; with the latter, a sinusoidal stress is applied, and the corresponding strain is recorded. The fatigue limit can be determined by a stepwise increasing

strain test (SIST) when the strain-controlled mode is applied. In the case of stress-controlled mode, the endurance limit, which is the equivalent of the fatigue limit, is determined by doing a stepwise increasing load test (SILT) [48]. The detailed methodologies for these tests will be described in the next two sub-sections.

Stepwise Increasing Load Tests (SILT)

SILT is carried out to obtain load limits for long time dynamic loading. El Fray [48] has described stress-controlled dynamic creep tests involving stepwise increasing load tests (SILT), where each step was run for a specific number of cycles at low frequency (1-4 Hz) to limit the amount of hysteretic heating [48] and a constant R-ratio of 0.1. The R-ratio is defined as the ratio between lower stress and upper stress limit.

The maximum stress employed in the test is set at a value corresponding to stress levels in the range of 5–50 % of the ultimate tensile stress (UTS) of the respective sample. At intervals of 1000 cycles, the stress load is increased by 5 %. Throughout the procedure, stress and strain are monitored as a function of time to produce hysteresis loops. From the hysteresis loops, dynamic modulus, damping and energy properties are determined. A representative SILT is portrayed in Figure 2.6 where the stress during each cycle is held constant.

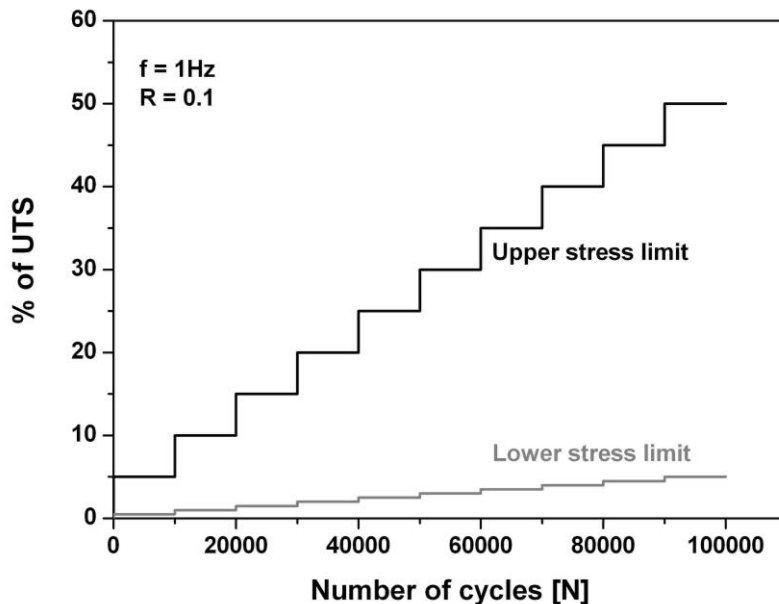


Figure 2.6: Representative SILT. Each level of stress is held for 10,000 cycles. Stress is represented in percentage of the UTS (σ_{ult}) for the sample being tested.

El Fray used the software to track the dynamic modulus and noted that a drop of more than 5 % was observed at a unique loading level, which corresponds to the endurance limit. This agreed with earlier work [49], which suggested that this drop was a result of internal damage. Using afterwards a single load test (SLT) over 100,000 cycles at the endurance limit, the change in the damping properties, strain, loss and stored energy were all obtained from the hysteresis loops. These tests paved the way for strain-controlled and further fatigue measurements.

Stepwise Increasing Strain Test (SIST)

Strain-controlled measurements are similar to stress-controlled ones, except that the maximum strain is held constant rather than the maximum stress. Stepwise increasing strain tests (SIST) are also performed at low frequency (1-4 Hz) to limit the amount of heating [50]. In these studies, the maximum strain was increased by 5 % at each “step”, as shown in Figure

2.7. It is important to mention, that due to the enlargement of the samples during the dynamic loading, also named creep, the specimen will buckle in the unloading state, when the tests are performed using a constant load ratio (e.g. $R = 0.1$). In order to prevent the buckling of the specimens, a very low, but constant stress has to be realized during the unloading of each cycle, in order to keep the specimen during the whole test in a state of tension.

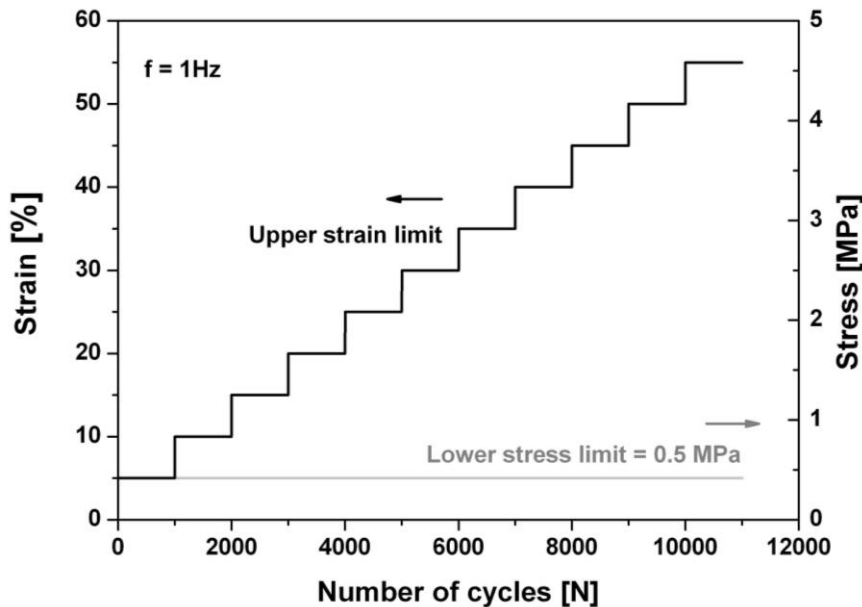


Figure 2.7: Representative SIST. Each level of strain is held for 10,000 cycles.

In a similar manner as the SILT tests, the dynamic modulus was tracked during the test. A drop of more than 5 % in the dynamic modulus signified the presence of internal damage. The loading (strain) before the dynamic modulus changes more than 5 % within one loading level is commonly accepted as the fatigue limit. Furthermore, it was also observed that prior to the fatigue limit, the dynamic modulus dropped quickly with increasing strain, but after the fatigue limit, the changes in dynamic modulus became less developed [48; 51]. Literature also suggests that a change in the slope of the dynamic modulus versus time signifies internal damage and hence, determines the fatigue limit [47].

In summary, Figure 2.8 compares once again the difference between the stress- and strain-controlled hysteresis approaches. Using the strain-controlled method leads to the characterization of the dynamic stress relaxation. The stress-controlled method in contrast describes the dynamic creep behavior of polymers, by monitoring the movement of the hysteresis loops along the strain axis. It is worth mentioning, that with both methods it is possible to obtain the corresponding stiffness and energy-related parameters in order to investigate the fatigue behavior.

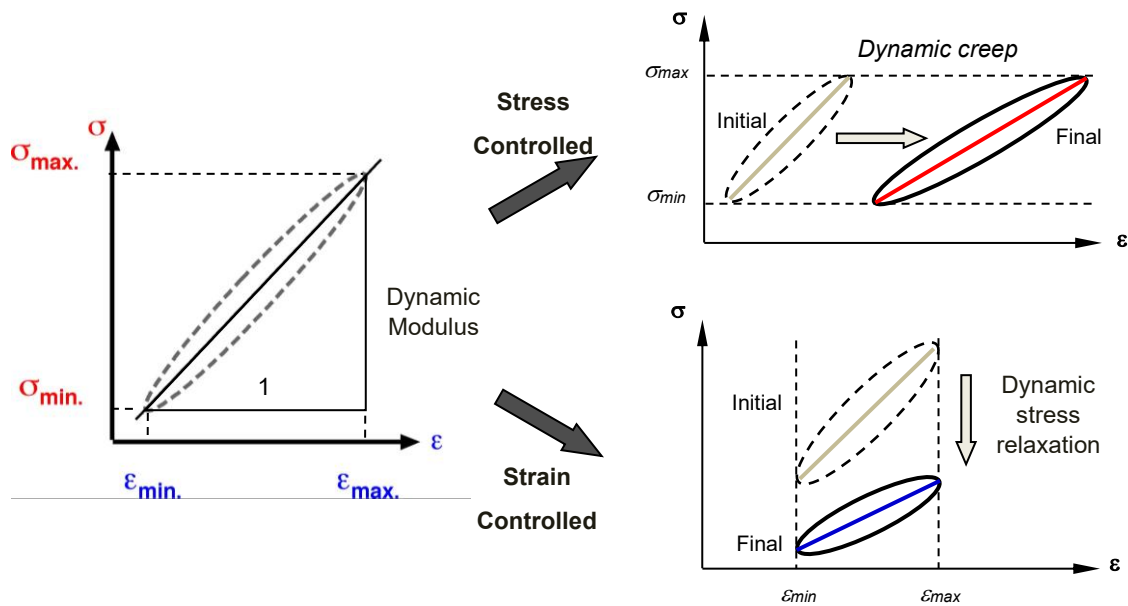


Figure 2.8: Comparison of stress- and strain-controlled hysteresis measurements.

Both SILT and SIST allow the simultaneous determination of several properties, such as stress, strain, stiffness, stored and loss energies and damping [44,46,47,48,49,50;51]. These advantages over the traditional methods make the hysteresis method very desirable for the determination of fatigue properties, especially for polymers. The hysteresis method is a dynamic test, similar to traditional fatigue tests, with the exception that stress and strain are monitored during each sinusoidal cycle.

The hysteresis approach is not only interesting in order to determine the fatigue/endurance limit, but by monitoring also the energy and stiffness parameter the final product can be modified to have not only similar tensile strength and strain, but also a similar stiffness and material damping. This is very interesting in the development of biomaterials, where implants are even more readily accepted by the human host body, when the properties of the implanted material are closer to those of the corresponding natural tissue. A material which is too stiff or a material without proper damping, can lead to degradation and even fracture of the surrounding tissue [53].

2.2 Biomaterials

2.2.1 Biomaterials used for medical applications

The term “biomaterials” designates synthetic or natural materials used to replace part of a living system or to function in intimate contact with living tissue. A biomaterial is intended to interact with biological systems to evaluate, treat, augment or replace any tissue, organ or function of the body [53, 54]. In order to qualify a material as a biomaterial, the major prerequisite, the biocompatibility, must be fulfilled [55]. Biocompatibility is generally described as the ability of a certain material to interact with an appropriate host response in a specific application [53]. Therefore, the criteria for determining the biocompatibility of materials are dependent on its practical application. Beside biological aspects, like being non-toxic or hypoallergenic, the issue of the mechanical stability and suitability of the materials for specific applications is important. Therefore, to qualify a material for biomedical applications, the necessary requirements can be divided in two main aspects, which are the biological response and the mechanical behavior, as demonstrated in **Figure 2.9** [53].

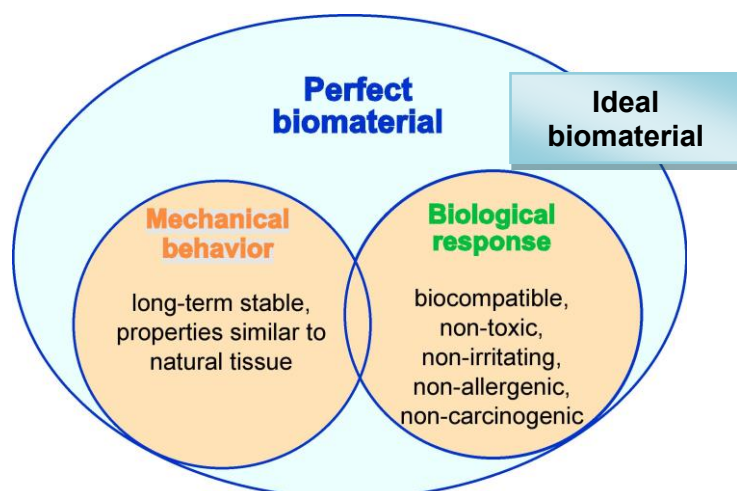


Figure 2.9: Requirements to qualify materials for biomaterials.

2.2.2 Elastomeric biomaterials

Tissues of the human body are usually classified as hard tissue or soft tissue [53,54,56,57, 58]. These structures were developed by nature in order to perform specific functions in the human body. Hard tissues, like bones and cartilages, will not further be described in details, as this work deals with biomaterials for soft tissues applications.

Among the soft tissues are four major categories: epithelium, muscle, nerve and connective tissue. Connective tissue can be segregated into loose tissue, which is cell rich (adipose, lymph nodes) and the dense tissue, dominated by fibers (skin, ligaments, tendons). From the above mentioned enumeration of the variety of different biological setups of human tissue, it is clear that for each tissue special requirements are necessary in order to replace or support it. Typical application areas for biomaterials in soft tissue replacement, which can be divided into the esthetic and orthopedic surgery are [57, 58, 59]:

- Cheek
- Skin
- Breast
- Blood vessels
- Tendons
- Cartilage
- Ligaments
- Artificial Hearts or heart valves

For most applications referenced above the biomaterial has to be soft, flexible or able to undergo high stresses and strains by simultaneously recover to their initial shape, hence being reversibly deformable. Therefore, elastomers are the materials of choice for these applications. A main characteristic feature of elastomers is the ability to withstand large deformations and strong forces without rupturing and returning to their original shape and size after the deformational forces are removed. From the group of elastomers, rubber and silicones are the most common materials, but the group of thermoplastic elastomers (TPEs) has developed to an appropriate alternative to rubbers and silicones in the field of medical applications. The major advantage of TPEs is that they may be treated like thermoplastic materials and therefore are re-moldable without losing their elastomeric characteristic [60].

As mentioned in Chapter 2.2.1 a biomaterial needs to behave similar to the tissue which is being replaced or supported. To give an overview about loadings and stiffness in the human

body, Table 2.1 presents the modulus and the tensile strength of several soft tissues of the human body and demonstrates the need to develop special biomaterials for each, shown by the variety of the mechanical properties of the specific human tissue.

Table 2.1: Mechanical properties of natural human tissue [61, 62, 63].

Tissue	Modulus of natural tissue [MPa]	Tensile strength of natural tissue [MPa]
Tendon	65 – 2300	50 – 100
Breast tissue	–*	–*
Ligaments	50 – 550	10 – 70
Skin	10 – 118	7 – 30

*no data available, due to the very complex construction of the human breast tissue

2.2.2.1 Silicone elastomers

Poly(dimethylsiloxane) is the most common siloxane polymer used in medical products, because it is an extremely versatile polymer [56]. In the following it will be referred to as silicone. It is unique in that it has a silicone-oxygen backbone and not carbon backbone like other polymers. The strong, very mobile bonds on its silicone-oxygen backbone are responsible to provide elevated chemical inertness and exceptional flexibility [60]. Furthermore, its properties are less temperature sensitive than other rubbers because of its low glass transition temperature (T_g). From these properties, silicones are used in many medical applications like catheter and drainage tubing, insulation for pacemaker leads and as a component in some vascular graft systems. Due to its high oxygen permeability, silicone is also used in membrane oxygenators. Its high tear strength, as well as its excellent flexibility and stability, qualifies silicone for a variety of prostheses, e.g. blood vessels, heart valves, outer ears or nose implants [56]. One of the most important medical applications for silicones are artificial breast implants for breast replacement or augmentation [53, 64]. The specific requirements and problems, which silicones in breast implants are faced with will be highlighted in the next section.

Artificial silicone breast implants

Silicone is the material of choice for artificial breast reconstruction and augmentation after mastectomy. Silicone breast implants came into existence with the creation of the first prototype by Cronin and Gerow in 1963 whose implant design consisted of a silica-reinforced silicone rubber shell, filled with silicone gel swollen in silicone oil [65]. Today the silicone rubber shell is reinforced with fumed nanosilica, and the filler material is either silicone gel or saline solution. The silicone gel implants are pre-filled and sealed before insertion into the body, while the saline implants can be filled via a valve after insertion similar to a tissue expander for breast reconstruction. The shell is expected to provide shape, strength and barrier properties, while the filling supplies bulk and consistency. Until today, the implant design concept itself was not changed. With time several severe health problems occurred with the silicone implant, like capsular contracture or implant fibrosis. To combat the capsular contracture, the shell thickness and gel viscosity were reduced in the second generation implants introduced in the early 1980s. However, the thinner shell resulted in an increased rate of implant rupture and/or gel bleed resulting in the diffusion of non-crosslinked silicone gel and silicone oil into the body. A third generation of breast implants was designed with shells of intermediate thickness and gels of medium viscosity [21].

Manufacturers also introduced various minor modifications to reduce capsular contracture and gel bleed, e.g. covering the silicone implant with polyurethane foam or inserting a barrier layer into the shell. Unfortunately, the results were generally poor with some even inducing further health complications and these multiple lumen implants were withdrawn from the market [21].

Currently, the majority of silicone implants available to the public continue to be a single silica-reinforced cross-linked silicone rubber shell filled with saline or silicone gel swollen with silicone oil. For all these years, the safety of breast implants has remained a controversial subject. In the literature related to explantation, various groups of scientists reported a failure rate of 12 – 53 % (total rupture) of silicone gel filled implants. Data shows that the rupture rate of these silicone implants clearly increases with the duration of implantation. Other than implant rupture, two other common reasons cited for explanations are capsular contracture and local or systemic symptoms. As the leading complication, capsular contracture commonly occurs during the initial months after surgery [21] and is frequently not reported because the patient is able and willing to tolerate the discomfort. Like capsular contracture, local or systemic symptoms occur as a result of immunological response to the foreign implant and substances. Gel bleed, i.e., the diffusion of non-crosslinked silicone liquid into the body from the silicone rubber shell, or from the silicone gel through the shell, was suspected to set off immunological responses [21; 66; 67]. In recent years, different modifications of implants developed and are still under investigation [68]. But up to now, the FDA warns that complications with silicone implants still occur and patients would probably need one repeat operation and should seek regular Magnetic Resonance Imaging (MRI) exams after implantation [69].

In order to understand the structure-property-relationship of silicone breast implants, it is important to review the chemistry and material properties of silicones. Silicone is a chemically inert synthetic polymer with repeated Si-O (siloxane) bonds in its polymer chain backbone. The number of repeat units along the silicone backbone can be controlled in the synthesis to change its viscosity and further properties. Silicone rubber used for the implant shell is obtained by crosslinking higher molecular weight siloxane chains at high temperature with peroxides, or at room temperature using platinum catalysts. Silicone gel is produced by crosslinking or vulcanizing low molecular weight polymer chains. Like most thermoset rubbers, uncrosslinked silicone rubber (“gum rubber”) is very weak and must be reinforced [70]. Medical grade silicone rubber is usually reinforced with silica (SiO₂) nanoparticles to reach a tensile strength of about 10 MPa with ~ 1000 % elongation [71], which is still less than half of the strength of other filled rubbers [72]. Silicone rubber is known to swell in oils and water, because it is highly permeable. Therefore, silicone rubber swells easily when in contact with silicone gel [70]. This creates a concentration gradient of silicone liquids between the shell and surrounding breast tissues to promote the diffusion mechanism for the onset of gel bleed where non-crosslinked polymer and silicone oil can seep into the human body. The extent of gel bleed depends on the molecular weight of the liquid fraction, the degree of crosslinking of the gel, shell thickness and the implant surface area. Swelling of the shell can cause mechanical weakening, but it should be stated that the ultimate tensile properties of soft tissues are relatively low (<3 MPa tensile strength and <100 % elongation [73]) so the ultimate properties of silicone rubber should be more than adequate, even in the swollen state. However, a recent study of Pukas and her co-worker showed that the tensile strength and the elasticity of silicone are reduced when explanted (after 2-week implantation) samples are compared versus neat sample [74]. Furthermore, the fatigue properties of silicone rubber are inferior to other thermoset rubbers as well as soft tissues. Due to the cyclic loading on the implant by body movement, fatigue cracks can develop and grow in the silicone rubber shell to form more convenient pathways for more gel bleed and the eventual occurrence of rupture.

In spite of advances made to improve the material formulation and the design of breast implants over the years, associated complications still exist. The above review suggests that a less permeable and especially more fatigue-resistant shell material would prevent gel bleed and rupture, which could lead to minimized capsular contracture.

2.2.2.2 Thermoplastic elastomers (TPEs)

Thermoplastic elastomers (TPEs) are an unique class of materials, which are “crosslinked” by self-assembly. Though being macroscopically homogeneous, these polymers phase-separate at a nanoscopic scale. Discreet plastic phases are embedded in the continuous elastomer phase and form physical crosslinks at the plastic/rubber interface. Hence, TPEs behave like cured rubbers at room temperature and can be processed as plastics at higher temperatures via standard processing methods, such as extrusion and injection molding. Upon cooling, the physical crosslinks are restored to reach a cured state. With no chemical crosslinkers like in the rubber vulcanisation step, TPEs have better recyclability and biocompatibility [75]. While blends of elastomers and thermoplastics are not compatible and show gross phase separation, block copolymers can only phase separate on a microscopic scale due to the connectivity of elastomeric and thermoplastic blocks.

Block-type TPEs contain at least two types of chemically attached thermodynamically incompatible polymeric blocks: a thermoplastic (A), with the option of the thermoplastic block being semicrystalline, and an elastomer (B) [75]. Linear A-B-A type TPEs have well-ordered nanostructures, while (A-B)_n type segmented block TPEs (e.g., poly(aliphatic/aromatic-ester) multiblock copolymers (=PED) have less ordered nanophases [76]. The phase morphology of block-type TPEs has been studied using electron microscopy, atomic force microscopy (AFM) and X-ray crystallography [77]. At 70 wt% soft phase content that yields optimal rubbery behavior, well-defined A-B-A type blocks have cylindrical hard phases with 20-40 nm diameter, distributed over the continuous soft phase under equilibrium conditions. However, commercial block-type TPEs of the same composition can have a mixture of spherical, cylindrical and lamellar hard phases [75, 77]. The size of the discreet hard phases ranges from 10 to 100 nm, based on TEM, SEM, SAXS and WAXS studies.

Common classes of segmented multiblock TPEs for biocompatible materials are poly(ester-urethane)s, poly(ester-ether-ester)s, and poly(ester-ether)s [75, 78]. Of all, commercially available polyurethane and polyester biomaterials include Pellethane®, Hytrel® and Arnitel™ [76]. In general, these materials exhibit outstanding elasticity, tear strength, solvent resistance, low-temperature flexibility, and strength at elevated temperatures [60]. Thermoplastic urethane elastomers (TPUs) possess a two-phase microstructure: hard and rigid isocyanate segments separating into glassy or semicrystalline domains dispersed in macrodiol soft segments that form an amorphous or semicrystalline matrix [79]. One of the earliest polyurethanes developed for biomedical applications was Biomer®, a poly(ether-urethane), with soft segments of poly(tetramethyleneoxide) (PTMO), hard segments of 4,4'-diphenylmethanediisocyanate and chain-extenders being a mixture of diamines, primarily with ethylene diamine [80]. It is characterized by excellent physical and mechanical properties and relatively good blood compatibility.

Furthermore, in the early 1980s, Medtronic Corporation (Minneapolis, MN) introduced the polyether urethane-insulated pacemaker lead, which was manufactured by Dow Chemical and called Pellethane 2363 80A, a thermoplastic aromatic polyether urethane. After the first reports about cracking of the polyether urethane insulator, the degradation of these polyurethanes became widespread and represented the limiting factor in the development of novel medical devices using polyether urethane. Shortly after these findings *Pinchuk et al.* showed that polyurethanes easily undergo biodegradation. Subcutaneous implants of TPUs in animals showed significant biodegradation in less than 4 weeks [81]. These findings lead to the investigation of many polyurethanes with soft segments including polydimethylsiloxane (PDMS) diols and fluorinated PDMS diols. Furthermore, surface treatment of conventional polyurethanes, such as with plasma polymerized polytetrafluoroethylene (PTFE) and surface-grafted PDMS, were also investigated [82, 83]. As a consequence, a variety of polyurethanes with various soft segments containing PDMS and surface modifying agents have appeared in the literature over the last decades; however, these materials exhibited similar biodegradation [84, 85, 86, 87, 88, 89]. These discussions finally lead to the development of polycarbonate

Linear triblock SIBS and triarm-star SIBS block copolymers can be considered as the first generation of PIB-based TPEs. Developed subsequently as the second generation [75, 96], multiarm-star branched blocks are attractive because of their higher moduli and lower viscosity, compared to the first generation polymers of similar molecular weight [97]. Multiarm-star blocks are also expected to impart good shear stability. Finally, novel arborescent PIB-PS block copolymers with TPE properties were introduced recently [98, 99] as the third generation of PIB-based TPEs. In addition, these arborescent copolymers have a “double-network” structure, where its thermolabile physical network derived from the self-assembly of PS blocks is superimposed on covalent branching points.

Figure 2.12 shows the various architectures of these PIB-based TPEs. The recent test marketing of PIB-based TPEs by Kuraray of Japan (TS Polymers®), Kaneka of Japan (SIBStar®) and BASF (Oppanol IBS®) demonstrates the potential of commercial viability of these materials [100]. SIBS block copolymers, being transparent and soft, have attracted attention as potential biomaterials for soft-tissue replacement. The first generation SIBS was confirmed to be biocompatible and received FDA approval in 2004 as polymeric coating on medicated coronary stents (Translute™) [101].

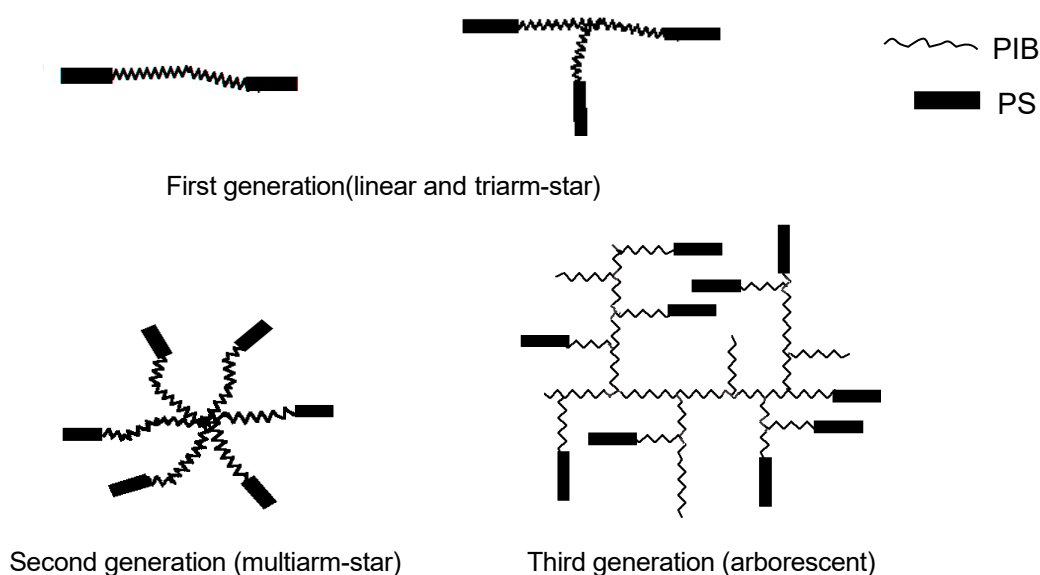


Figure 2.12: Architectures of SIBS block-type TPEs.

From the above review concerning the elastomeric biomaterials, it is clear that much has been done concerning the synthesis and morphological characterization of TPE based biomaterials. Their specific properties, like biocompatibility as well as static mechanical performance are well documented in the literature. However, besides the (bio-) degradation, these biomaterials have poor long-term fatigue behavior [91, 102]. But the long-term fatigue performance of these polymers is particularly important because during their lifetime the loading experienced by these devices is dynamic in nature. Over a long period of time, these dynamic loadings increase the creep and induce fatigue damage, like micro-cracks, in the polymers. It is reported that currently used biomaterials like thermoplastic polyurethane and linear triblock SIBS have poor creep resistance as well as medical grade silicone [91, 103, 104].

Therefore, from the review above, it became apparent that new polymers are needed for medical devices that require long-term implantation for load-bearing applications. It is essential to modify the currently used biomaterials to withstand the applied loadings during usage.

2.2.3 Modification of the mechanical performance of elastomers / biomaterials

In order to address the lack of the mechanical properties of elastomeric biomaterials there are several possibilities found in the literature. The first approach is to introduce a network, which can further reinforce the material with covalent crosslinks from high-energy irradiation or during the polymerization process itself [105]. Production of rubbery materials by high-energy crosslinking has been well established. For instance, excellent rubbery materials can be produced by cross-linking polyethylene with γ - or e-beam irradiation [106]. The use of e-beam irradiation improves the static mechanical behavior of polymers, but can also yield better dynamic creep and fatigue resistance [107]. For ultra high molecular weight polyethylene, radiation is known to improve mechanical properties [108, 109]. It is highly expected that fine structural changes (other than the cross-linking) are induced during the irradiation process and they must play an important role in modifying the physical properties [110, 111]. Nevertheless, systematic studies on the microstructures and their changes from the irradiation and their correlations with the physical properties are very rare [112]. Other than for medical applications, irradiation of polymers is also interesting for the food industry, for technical polymers like polypropylene, to accelerate aging as well as for radiation induced polymerization. The polymer afterwards may be protected against the effects of heat, oxygen, light, high energy radiation and so on [113].

However, one has to keep in mind that using irradiation of polymers to modify the structure, can also lead to material degradation, which can be avoided by a proper selection of radiation dosage or anti-oxidants [114, 115, 116].

The second approach to modify the structure of thermoplastic elastomers, besides changing the hard phase content, is the use of additives [75]. In the rubber industry, mineral fillers, like carbon black (CB), silica particles, and layered silicates or clay, are widely added to polymers for reinforcement or as processing aids [117]. It was the seminal work of Kojima and his co-workers in their successful development of nylon-clay nanocomposites at the Toyota research laboratory, [118] which demonstrated the synergistic benefit of using nano-scaled fillers, like nano-clay and carbon nanotubes, in polymers to modify the performance of the final materials. This nano-filler technology has opened up new possibilities for polymer formulation and established an entirely new area of research for polymer science and engineering. To fully harness the synergistic effect of polymer nanocomposites, one must disperse these nano-fillers uniformly throughout the polymeric matrix. Once a good filler-matrix surface interaction can be established, polymer nanocomposites can offer lighter materials with improved properties at a lower filler loading (and hence lower cost) over conventional composites with reinforcing fillers of sizes greater than the nanometer scale [119]. Particularly, with CB particles, this class of fillers has been extensively used in the rubber industry to make tires for color pigmentation, material reinforcement, heat dissipation and static discharge. CB fillers can also act as radical scavengers to prevent the thermal decomposition of polymers, like PIB, and thereby increase their onset temperature of thermal degradation [120]. For TPEs, Puskas and co-workers studied the incorporation of CB nanoparticles (N234 – Cabot Corporation) into dendritic poly(isobutylene-*b*-styrene) block copolymers (D_IBS) to show increased ultimate tensile strength (UTS) and domain size of secondary phase in all cases [121]. Improvements in mechanical properties (e.g. UTS, tear strength, and Young's modulus) of styrene butadiene rubber/high density polyethylene (HDPE) blends using CB and other fillers, like clay, silica and titanium dioxide, were also demonstrated by Jayasree and Predeep [122]. In the use of CB fillers, the transmission electron microscopy (TEM) evidence provided by Yamauchi et al. indicated that the CB fillers dominantly located in the elastomeric region of natural rubber/HDPE blends [123].

The review above indicates that there exist several approaches to modify the structure of polymers and especially of TPEs. Therefore, it is of scientific interest to evaluate the effect of cross-links as well as the use of nano-scaled additives on the morphology, physical properties

and respectively lead to a fundamental understanding of the structure-property-relationship of different innovative TPEs.

2.3 Fatigue of polymeric biomaterials

The mechanical performance of biomaterials for products like implants, and rubbery medical parts is scrutinized with the same importance as biocompatibility because their inadequate performance or even premature failure can create health issues for users and might, at its worst, lead to the loss of human lives. As a result, the durability or long-term mechanical performance of new biomaterials has also become a prime concern in their adoption for medical devices. Furthermore, for body implants, most of the loadings encountered are dynamic in nature and it is unacceptable for biomaterials to lose their mechanical properties under sustained loadings. To reduce the number of surgical operations on users, implants are expected to remain in the body for a long period of time [48]. In view of all these, the knowledge on the long-term dynamic properties of biomaterials as well as the later medical product is therefore of great importance.

In principle, all three material classes (ceramics, metals and polymers) are suitable for the use as biomaterials. But as the mechanical properties of these material classes are very different in terms of tensile stress/strain, stiffness, fracture toughness and damping behavior, it is clear that each material will have different uses in the human body, depending on the required properties. This also brings up the idea that for each material class, different methods of fatigue evaluations are necessary.

As this work covers the fatigue behavior of polymeric / elastomeric biomaterials the fatigue of polymeric materials will be described in detailed in the following subsection.

In the field of polymer engineering, the conventional S/N method using cyclic fatigue machines for determining the endurance stress limit faces two main difficulties. First, because of the low thermal conductivity of polymers, fatigue experiments can only be performed under low frequency because under high frequency the mechanism of failure is associated with localized thermal fatigue. Secondly, low frequency fatigue experiments are time consuming. Nevertheless, some researchers have termed such tests as static fatigue experiments. Previous works [124, 125, 126, 127, 128] have shown that the lower stress limits of many polymers can be obtained by non-linear computational modeling of creep rupture time using a three-element mechanical model having a rate activated dashpot to simulate plastic flow, in conjunction with a critical elastic energy criterion. Figure 2.13 shows some examples of the modeling for some polymers at 37°C in saline solution. Good fits can be observed in all cases.

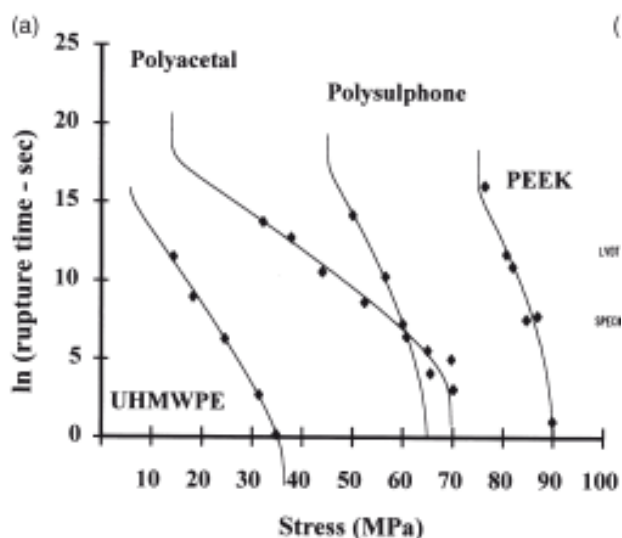


Figure 2.13: Creep rupture modeling of some medical plastics [128].

The results for UHMWPE and polyacetal reveal that the lower stress limits were no more than 12 MPa, in saline solution, 37°C. This may well account for the current problems in wear debris formation and failure of the acetabular UHMWPE cup used in many hip joint prostheses where the contact stresses can exceed 30 MPa. Some more potential medical polymers like polyethyletherketone (PEEK) and polysulphone were also modeled and led to S/N values of 75 and 45 MPa, respectively. The obtained values were much greater than for polyethylene and hence, these polymers are more suitable to be used as biomaterials, where high bearing stresses are concerned.

Considering the polymers mentioned above, UHMWPE is the most common polymer used, and has been employed for 40 years as a biomaterial in artificial hips and knees. Hence, UHMWPE represents also the most well-characterized polymer for medical applications [129]. It was the work of Pruitt and her co-worker who extensively studied the failure of UHMWPE implants as well as transferring technical plastic investigations methods like fatigue crack propagation to the characterization of biomaterials [130, 131, 132, 133, 134, 135, 136, 137, 138].

From then, Pruitt and her co-worker as well as other research groups, systematically started investigating the failure of UHMWPE implants by combining the method of fatigue crack propagation and the study of the wear due to cyclic loading [139; 140; 141] and showed that the crack initiation resistance of a UHMWPE component was governed by intrinsic material behavior, extrinsic design, and clinical factors. The material and design characteristics of importance depend on the physical model used to describe crack initiation. The viscous flow of the highly stressed material at a notch or crack tip has been proposed as the dominant deformation fracture mechanism in UHMWPE [142, 143; 144].

In 2007, Galetz and co-worker used the modern hysteresis approach to characterize the fatigue limit of cylindrical UHMWPE samples. They showed that during cyclic fatigue testing at high stresses three different cases can be distinguished depending on the load and on the heat dissipation (see Figure 2.14) [145, 146]:

If the load is higher than the ultimate compressive strength, failure occurs after the first cycle. If the load is above a critical value, it leads to failure within the first 100,000 cycles due to heat generation.

Below this critical value, and after an initial deformation, only very small deformation rates can be measured, which indicate that the samples have reached long term stability.

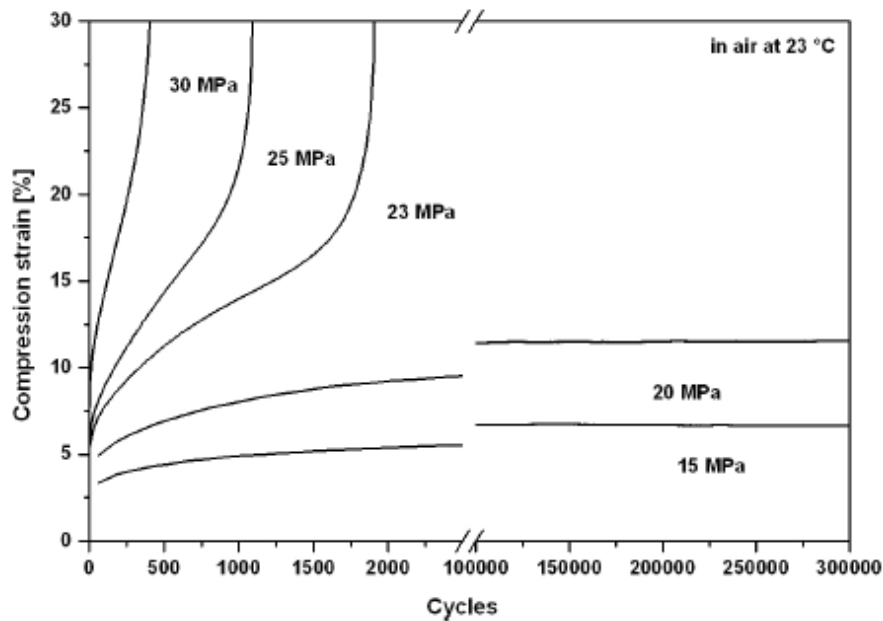


Figure 2.14: Strain *versus* cycles of the fatigue behavior tested in air at 23°C [145].

In 2003, El Fray and co-workers transferred the hysteresis approach into the field of biomaterial investigation. Using the evaluation of hysteresis loops, she studied the dynamic fatigue behavior of several thermoplastic elastomers. Therefore, with the help of servo-hydraulic testing equipment, a dynamic load or deformation was applied on S2 samples according to ASTM D 1708 [147]. The experiments were performed using a frequency range from 1-4 Hz and the selected R-ratio was 0.1 in value. With this approach, it was shown that poly(aliphatic/aromatic-ester) (PED) multiblock copolymers compare very well with commercial poly(ester-ethers) and have an improved performance than poly(ester-urethanes) when loaded at the same fatigue stress level relative to their ultimate tensile strength [48, 50, 52] (see Figure 2.15).

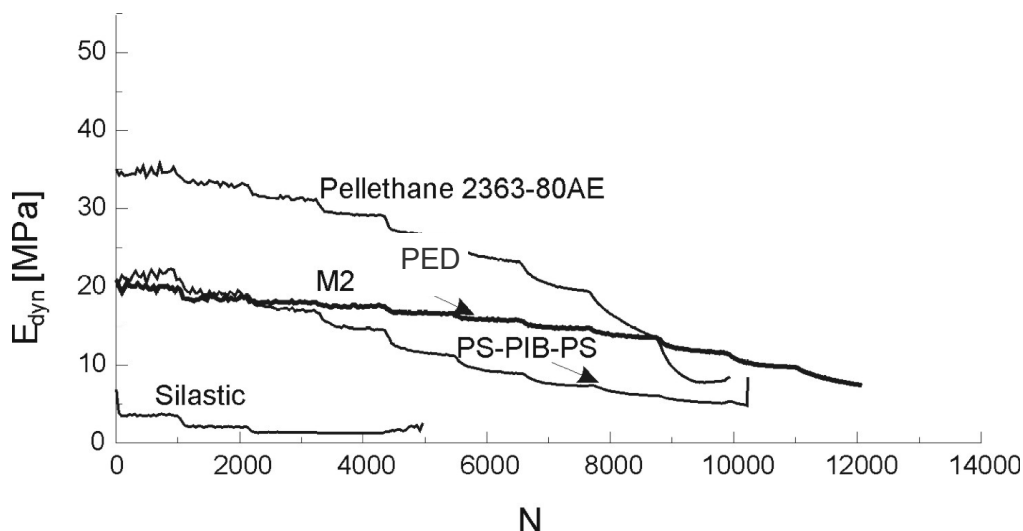


Figure 2.15: Dynamic modulus as a function of loading cycles (N).[51]

Figure 2.15 presents a comparison of the change in dynamic modulus with the loading cycles between silicone rubber (Silastic®), medical-grade polyurethane (Pellethane®), PED and linear triblock SIBS (similar to Translute™). For this study, both Silastic® and Pellethane®

have a Shore A hardness of about 85 while PED, with 70 wt% of soft segments was adopted for a comparable hardness. From Figure 2.15, the initial dynamic moduli of SIBS and PED are at a level of 20 MPa, while Silastic® has a lower initial value of 5 MPa. From then, the material degrades rapidly at higher loading cycles and fails earlier than others. On the other hand, Pellethane® has the highest initial dynamic modulus among all materials and remains so over a large number of loading cycles. Interestingly, as compared to Pellethane®, PED and SIBS have similar performance beyond 8000 cycles and exhibit lower degree of degradation relative to their initial dynamic moduli. This outlines the potential of PED and SIBS in terms of their fatigue performance to replace silicone rubbers in biomedical applications, and also highlights the needs to improve the stiffness to compete with medical-grade polyurethanes. The preliminary results presented here for SIBS are in line with several reports on their superior flexural-fatigue and trouser-tear properties compared to other rubbers [148, 149, 91]. Apart from the above-mentioned general approaches related to the material class, some standardized fatigue tests on specific surgical implant materials and devices have been developed over the years (see Table 2.2) and shows that most of them are for metallic or rigid plastic devices.

Table 2.2: Specific fatigue testing of surgical implant materials and devices.

Fatigue tests	ASTM ref.
Practice for cyclic fatigue testing of metallic stemmed hip arthroplasty femoral components without torsion	F 1440-92
Test method for bending and shear fatigue testing of calcium phosphate coatings on solid metallic substrates	F 1659-95
Test method for constant amplitude bending fatigue tests of metallic bone staples	F 1539-95
Test methods for static and fatigue for spinal implant constructs in a corpectomy model	F 1717-96
Guide for evaluating the static and fatigue properties of interconnection mechanisms and subassemblies used in spinal arthrodesis implants	F 1798-97
Practice for corrosion fatigue testing of metallic implant materials	F 1801-97
Test method for cyclic fatigue testing of metal tibial tray components of total knee joint replacements	F 1800-97
Practice for constant stress amplitude fatigue testing of porous metal-coated metallic materials	F 1160-98

To sum up, the above described shows, that for polymeric biomaterials, there are no standardized testing methods available, to evaluate the fatigue behavior of specific biomaterials. Especially, when talking about silicone breast implants, there exists a lack of knowledge how dynamic loading can affect the device. Testing ready-to-use devices in order to develop new medical devices seems to be more a trial and error method than a scientific approach, which will be expensive, as the whole device has to be tested. Therefore, the highlighted hysteresis approach to evaluate the stiffness, deformation, loss- and storework as well as the damping behavior of innovative polymeric biomaterials can be seen as a more effective method, because the material properties can be tailor-made, when the structure-property relationships are clarified. Although the hysteresis approach already was applied, there is much space for further development. Furthermore, a method would be necessary to investigate both hard biomaterials and soft biomaterials, which have a difference in stiffness as well as compliance.

3 Objective and strategy

Literature shows, the introduction of additional cross-links or chemical network structure in thermoplastics, obtained by irradiation or (nano-scaled) additives, can improve their dynamic creep and fatigue performance (e.g. Ultra high molecular weight polyethylene).

However, only limited studies are available providing an in-depth understanding of the effects of secondary chemical or physical networks on the properties of TPEs. A systematic evaluation of such materials could provide the essential link between the network structure and the physical as well as mechanical performance. Establishing structure-property relationships could provide a pathway for developing a new class of safer, high performance TPEs for soft tissue applications. Simultaneously, the synthesis of such TPEs as well as the production of the final devices needs to be cost efficient, without losing its superior mechanical behavior, to provide an innovative biomaterial.

The working hypothesis of this research is centered around investigating the dynamic mechanical behavior of newly developed advanced biomaterials for the challenging demands of current and future applications. As a novel approach, TPEs modified via chemical crosslinking and/or nano-scaled additives thereby altering the dynamic creep and fatigue properties of these TPEs will be developed. Particularly, focusing on the mechanical performance, the influence of the obtained secondary network structure on the material properties will be investigated in detail. In order to provide reliable data, the relationships between morphological, thermal, mechanical properties as well as the effect on the dynamic creep and fatigue properties will be fully elucidated.

The scope of the work will include:

1. The study of the effect of chemical network obtained via electron beam irradiation on the mechanical properties of poly(aliphatic/aromatic-ester) multiblock copolymers (PEDs). In particular, the feasibility of using e-beam cross-linking for improving the dynamic fatigue performance is discussed and correlated to the morphology as well as network structure.
2. Investigation of crosslinking of poly(isobutylene-b-styrene) (IBS) block copolymers introduced during polymerization into these soft TPEs. In order to account for the softness of the IBS polymers, novel characterization concepts are developed and discussed for analyzing the (long-term) mechanical performance. Both the effect of altering the hard/soft segment ratio, and block length of the TPEs is covered.
3. Investigation of the effect of additional network structure via adding nano-scaled additives (carbon black and nano-clay) in poly(isobutylene-b-styrene) (IBS) block copolymers. In order to assess the effect of these nano-additives on the morphology and especially on the mechanical performance, IBS block copolymers with different molecular weights, fillers as well as filler contents are studied to understand the correlation between secondary network structure and the (long-term) mechanical performance.

4 Materials

In order to achieve the challenging goal of clarifying the influence of different network structures on the mechanical performance of thermoplastic elastomers (TPEs), an appropriate choice of materials is essential, to finally tailor-make biomaterials for specific applications. Therefore, two different classes of TPEs were taken. A first class consists of TPEs cross-linked after the polymerization using e-beam irradiation and represents a rather hard TPE (poly(aliphatic/aromatic-ester)s multiblock copolymers (PEDs)). In contrast, the second class, the rather soft poly(isobutylene-*b*-styrene) block copolymers, is chemically cross-linked during the polymerization or modified using nano-scaled particles like carbon black (CB) or nanoclay (NC) after the polymerization.

The materials employed in this study are presented in more detail in the following sections.

4.1 Poly(aliphatic/aromatic-ester)s multiblock copolymers (PEDs)

Segmented poly(aliphatic/aromatic-ester)s multiblock copolymers (PEDs) contain discrete nanometric hard segments of semi-crystalline poly(butylene terephthalate) (PBT) embedded in a matrix of soft segments containing aliphatic dimer fatty acid (here dilinoleic acid (DLA)), that impart the elastomeric character to the copolymer.

These PED were obtained in a two-stage process of transesterification and polycondensation in the melt as described elsewhere [169]. Briefly, dimethyl terephthalate (DMT) and 1,4-butanediol (1,4-BD) were subjected to transesterification process to produce oligomer of butylene terephthalate (PBT) and using tetrabutoxy titanate as a catalyst. Then, oligomers of PBT were reacted with dimer fatty acid (here DLA) and a catalyst to initiate the polycondensation process at 250°C. The hot reaction mass was extruded into water using compressed nitrogen, granulated and then purified by Soxhlet extraction from methanol [114]. The use of thermal stabilizers for the synthesis is not required [114, 151, 152, 153] and the DLA component has a good oxygen and thermal stability. Furthermore, the biocompatibility of both PBT and DLA has been well established [51, 152]. The chemical structure of the segmented PED is shown in Figure 4.1.

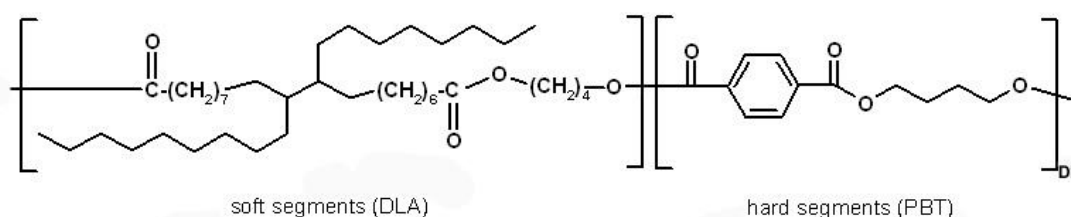


Figure 4.1: Chemical structure of poly(aliphatic/aromatic-ester) (PED) multiblock copolymers, composed of dilinoleic acid (DLA) as the soft segments and poly(butylene terephthalate) (PBT) representing the hard segments.

In this study, two hard/soft segment ratios of PED were investigated, PBT-26 and PBT-30, with PBT-26 containing 26 wt.-% PBT and 74 wt.-% DLA and PBT-30 containing 30 wt.-% PBT and 70 wt.-% DLA, respectively. The materials have been synthesized at the Department of Polymer and Biomaterials Science at the West Pomeranian University of Technology, Szczecin, Poland).

4.2 Poly(isobutylene-*b*-styrene) (IBS) block copolymers

Poly(isobutylene-*b*-styrene) (IBS) block copolymers are a relatively new class of TPEs that bear large potentials as biomaterial. Effectively, they display a favorable profile of properties as compared to conventional biopolymers like silicone rubber. These advantages are good

biocompatibility, *in vivo* biostability, and a better mechanical behavior [51, 102]. Synthesized by living carbocationic polymerization [154], the first generation of IBS polymers has a triblock architecture arranged in a linear form (designated as L_SIBS) [155], as shown in Figure 4.2(a). The good biocompatibility of L_SIBS earned the FDA approval in 2004 to be used as a polymeric coating on drug-eluting coronary stents [101, 156]. Newer generations of this material have evolved with various architectures given in Figure 4.2(b) and (c), like the second generation of multi-arm star polymers [96], and the third generation (named D_IBS) with dendritic or tree-like branched structure [73, 157, 158].

Novel chemical synthesis approaches were adopted to yield these three generations of IBS materials. The first and second generations of IBS were synthesized using di- and tri-functional initiators [77] respectively, to produce the desired linear and star-shaped block copolymers using the living carbocationic polymerization. For the dendritic D_IBS, its synthesis can be performed in one pot using 4-(2-methoxy-isopropyl)styrene as an inimer (initiator-monomer) to initiate the “chain growth” of an dendritic poly(isobutylene) (PIB) core [159] before adding styrene or styrenic derivatives, like para-methyl styrene (PMS) as the end-blocks [73,77; 159]. PMS is favored over styrene for its higher blocking efficiency and better reproducibility in the synthesis of D_IBS [160]. Recently, the fourth-generation of IBS polymer, D_IB-MS, was synthesized in one step by using 4-(1,2-oxirane-isopropyl)-styrene) to create a dendritic PIB core with primary hydroxyl groups at each branching point and with PMS end-blocks [159]. These hydroxyl groups were shown to preferentially go to the surface of the material to create a more hydrophilic surface in an effort to improve material-tissue interaction for better biocompatibility [161].

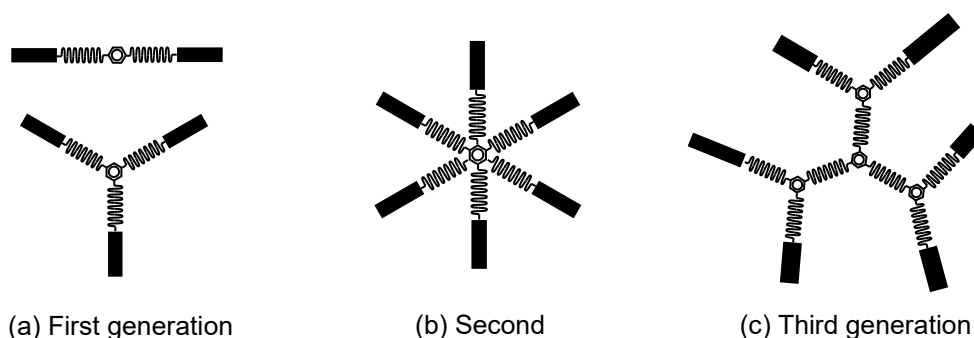


Figure 4.2: Schematic drawings of the architectures of (a) the first generation (L_SIBS), (b) the second generation and (c) the third generation (D_IBS) of IBS polymers (~~~~~ = PIB; \blacksquare = PS or other derivatives) [162].

Table 5.2 in the Chapter 5.1.2 summarizes the five dendritic IBS block copolymers, which were synthesized by Prof. Puskas et al. heading the “Department of Polymer Science” at the University of Akron (Ohio, USA) for this study.

4.3 Benchmarking materials

Dependent on the study, several materials were used as benchmarking materials. In particular two medical-grade silicone rubbers, one thermoplastic polyurethane and two linear SIBS block copolymer were used in this study.

The medical-grade silicone rubbers (MED 4050 and MED 4750) were supplied by NuSil Technology, while the medical-grade thermoplastic polyurethane (Pellethane® 2363-80A) was obtained from Dow Plastics. The linear SIBS (L_SIBS) polymers (SIBSTAR 073T/SIBSTAR 103T) used in this work were provided by the Kaneka Corporation. The material designations and some important mechanical properties (hardness, tensile strength and elongation at break) are shown on Table 4.1. The values are taken from the datasheet provided by NuSil Technology, Dow Plastics and Kaneka Corporation [163,164,165,166,167].

Table 4.1: Characteristics of the medical-grade silicone rubbers (MED 4050 and MED 4750), L_SIBS (SIBSTAR 073T and 103T) and TPU (Pellethane®-2363-80A) according to their datasheet.

Material	Material Designation	Hardness [Shore A]	Tensile strength [MPa]	Elongation at break [%]
MED 4050	Silicone	50	10.0	1,000
MED 4750	Silicone	50	10.0	1,000
SIBSTAR 073T	L_SIBS31	45	14.0	650
SIBSTAR 103T	L_SIBS34	46	18.0	620
Pellethane ® 2363-80A	TPU	80	35.8	550

4.4 Nano-particles

Mineral fillers, like carbon black, layered silicates or clay, are widely added to polymers for reinforcement or as processing aids. Therefore, selected IBS block copolymers were modified using carbon black (CB) and nanoclay (NC).

The CB nano-particles were obtained from the Cabot Corporation and the N234 grade was used. The key characteristics of N234 CB fillers are given in Table 4.2.

Table 4.2: Characteristics of CB featured in the current study.

ASTM #	Mean diameter [nm]	Heterogeneity Index	EMSA [m ² /g]
N234	20	1.57	124

EMSA: Estimated Mean Surface Area (Specific)

The clay filler used in this study was Cloisite®-20A provided by Southern Clay Products, Inc. Cloisite®-20A is a montmorillonite clay whose surface has been modified with dimethyl-dihydrogenated-tallow ammonium salt for improving its compatibility with non-polar polymeric matrices. This clay grade has a d_{001} spacing of 24.2 Å and a density of 1.77 g/cm³.

5 Experimental procedure

5.1 Sample preparation

5.1.1 Poly(aliphatic/aromatic-ester)s (PEDs)

After the synthesis of PED multiblock copolymers (see Chapter 4.1) the purified polymer was compression-moulded and e-beam irradiated in order to cross-link the PEDs. A linear electron accelerator Elektronika 10/10 was used to generate a 10 MeV electron beam for different dosages (25 kGy, 50 kGy, 75 kGy and 100 kGy). The irradiated samples have been prepared at the Institute of Nuclear Chemistry and Technology in Warsaw, Poland. Table 5.1 shows the materials of this study, the hard (wh) and soft (ws) phase contents, the weight and number average molecular weight (M_n and M_w), the disparity index \mathfrak{D} , the intrinsic viscosity number η and the hardness.

Table 5.1: Physical properties of synthesized and e-beam irradiated poly(aliphatic/ aromatic-ester) (PED) multiblock copolymers.

Designation	w_h (wt.-%)	w_s (wt.-%)	M_n (g/mol)	M_w (g/mol)	\mathfrak{D}	$[\eta]$ (dL/g)	Hardness [Sh A]
PBT-26	26	74	4,346	8,854	2.04	0.79	68 A
PBT-30	30	70	5,556	12,610	2.27	1.00	79 A

The samples did not show any water uptake at standard laboratory conditions. Finally, micro dumbbell-specimen were produced from the material with a cutting tool according to DIN 53504 [168].

5.1.2 Poly(isobutylene-*b*-styrene) (IBS) block copolymers

After the synthesis of, which is already described in Chapter 4.2, the D_IBS block copolymers were compression molded into 1 mm thick films. From these films, the samples for testing were obtained.

The investigated linear (L_) and dendritic (D_) IBS block copolymers are listed in Table 5.2. For convenience, the naming of material designation combines the type of IBS polymer (linear or dendritic) and the amount of hard phase (PS/PMS) content. So L_SIBS34 refers to the L_SIBS sample with 34 wt% of PS, while D_IBS27 stands for the branched polymer that contains 27 wt% of PS. In addition, the type of hard phase (polystyrene (PS) or polymethylstyrene (PMS)), the hard phase content, the number averaged molecular weight (M_n), the disparity index \mathfrak{D} and the average number of end blocks (N) in the branched samples (calculated as $B+2$ where B is the average number of branches per chain obtained from polymerization kinetics as reported [162]) is shown in the table.

Table 5.2: IBS materials used in the present work.

Material Designation	Hard phase	Hard phase content (wt%)	M _w (g/mol)	Đ	B+2
L_SIBS34	PS	34	78,000	-*	2
L_SIBS31	PS	31	67,000	1.2	2
D_IBS33	PS	33	70,000	4.5	4
D_IBS27	PS	27	178,000	2.7	4/5
D_IBS16	PS	16	119,000	2.4	3
D_IB-MS10	PMS	9.5	291,600	1.94	4
D_IB-MS17	PMS	16.7	146,600	1.46	5

* no data available

More details about the used materials are also presented in the respective chapter of the results and discussion section (Chapter 6).

5.1.3 Composite materials

In order to introduce a secondary network structure to the D_IBS block copolymers, nano-scaled fillers (carbon black and nanoclay) were added to the PIB-based TPEs.

5.1.3.1 Carbon black composites

The carbon black (N234) from Cabot Corporation was mixed at 60 phr (37.5 wt%) with D_IB-MS10 and D_IB-MS17 using a Brabender mixer at a fill factor of 78.8. 1 mm thick sheets were compression molded from the neat and carbon composites and micro-dumbbells were stamped out of these sheets. Neat D_IB-MS was compression molded at 120°C, while the filled D_IB-MS samples were molded at 145°C for 3 min at 0.304 MPa. The details of the D_IB-MS10 and D_IB-MS17 carbon black composites are listed in Table 5.3.

Table 5.3: IBS-carbon black systems.

Polymer Matrix	Filler	Processing Technique	Filler Content (wt%)	Material Designation
D_IB-MS10	Carbon black (N234)	Melt intercalation	37.5	D_IB-MS10_CB
D_IB-MS17	Carbon black (N234)	Melt intercalation	37.5	D_IB-MS17_CB

5.1.3.2 Nanoclay composites

The clay filler used in this study was Cloisite®-20A provided by Southern Clay Products, Inc. Cloisite®-20A is a montmorillonite clay whose surface has been modified with dimethyl-dihydrogenated-tallow ammonium salt for improving its compatibility with non-polar polymeric matrices. This clay grade has a d001 spacing of 24.2 Å and a density of 1.77 g/cm³. The clay filler was added at three different loadings (10, 20 and 30 wt%) to L_SIBS34 and D_IB-MS10. The solution blending approach was employed by first dissolving specific amounts of the polymer in a solvent mixture of tetrahydrofuran (THF) and methylcyclohexane at 20:80 (w/w) to yield to a polymer concentration of 25 wt%. The solutions in glass vials were

shaken on a shaker at a speed of 1000 rpm for 8 hours. The specified loadings of Cloisite®-20A were added and the mixtures were sonicated for 3 hours. To prevent an excessive temperature increase, the water bath was cooled with ice during the sonication. Then, the glass vials of polymer-clay solutions were again shaken for another 8 hours at 1000 rpm and sonicated for 15 min to remove any bubbles that formed during shaking. Finally, the polymer (or polymer-clay) solutions were poured into a Teflon® mould and dried overnight in a fume hood. After that, the moulds were covered with perforated aluminum foil and were transferred to a vacuum oven for further drying to constant weight. The entire drying process was conducted at room temperature. After drying, compression moulding was used to prepare films with a good surface finish. The neat D_IB-MS10 and its composites were moulded at 170°C. The final moulded sheets were 6 cm large and wide, with a thickness of 1 mm. The moulded sheets were cut into micro-dumbbells according to ASTM D 1708 [147] using a hydraulic press. The commercial grade of linear SIBS polymer (SIBSTAR 103T from Kaneka Corporation) was selected as the reference material for comparison of the clay-composites. Table 5.4 shows the detailed information about the various SIBS-clay systems.

Table 5.4: IBS nanoclay systems

Polymer Matrix	Filler	Processing Technique	Filler Content (wt%)	Material Designation
D_IB-MS10	Clay (Cloisite®-20A)	Solution blending	0	D_IB-MS10
			10	D_IB-MS10_C10
			20	D_IB-MS10_C20
			30	D_IB-MS10_C30
L_SIBS34	Clay (Cloisite®-20A)	Solution blending	0	L_SIBS34
			10	L_SIBS34_C10
			20	L_SIBS34_C20
			30	L_SIBS34_C30

5.1.4 Benchmarking materials

Pellethane® 2363-80A, representing the group of thermoplastic polyurethanes, and the linear SIBS (SIBSTAR 073T/SIBSTAR 103T) were taken as received and films of 1 mm thickness were compression molded using a hydraulic hot press (Webber PW10) according to their datasheets [165; 166, 167]. After cooling the film to room temperature, micro dumbbells were produced using a cutting tool according to the dimensions specified in ASTM D 1708 [147]. The two silicone based materials were delivered either in 1 mm (MED 4750) or 1.5 mm (MED 4050) flat sheets. These sheets were taken as received and micro dumbbells according to [147] were cut with a cutting tool.

5.2 Morphological characterization

5.2.1 Transmission electron microscopy (TEM)

PED samples were cut using a cryo-microtome into thin sections, which were subsequently stained with an aqueous solution of 0.2 wt.-% osmium tetroxide (OsO_4) at room temperature. Staining of the material was intended to affect the amorphous soft phase, which appears as the dark phase because of the reaction of DLA with OsO_4 [169, 170]. Similar approach was used to prepare thin sections of L_SIBS and D_IBS samples. In contrast to the PEDs these samples were then stained for 30 minutes using an aqueous solution of ruthenium tetroxide (RuO_4 - 0.5 wt%) at room temperature. Staining was intended to occur in the hard PS or PMS

phase through the chemical reaction between RuO₄ and the benzene ring [170]. All stained samples were examined using a Zeiss902 TEM at an applied voltage of 80 kV.

5.2.2 Atomic force microscopy (AFM)

A Dimension™ 3100M (Metrology) atomic force microscope (Veeco/Digital Instruments) was used. Images with a size of 1 × 1 μm² were acquired in tapping mode for all samples. The resolution was set to 512 × 512 points. The subsequent image processing includes image flattening using the software package Nanoscope 6.12r1.

5.3 Thermal characterization

5.3.1 Differential scanning calorimetry

Differential scanning calorimetry (DSC) measurements were performed using a DSC-Q1000 (TA Instruments, USA), with a triple cycle of heating-cooling-heating over the temperature range of -150 to 250°C at a heating/cooling rate of 10°K/min. The first heating cycle started at 23°C and is intended to remove the thermal history. All DSC measurements were conducted in a nitrogen environment at a flow rate of 50 ml/min.

The glass transition temperature (T_g) was determined from the thermogram of the second heating cycle as the temperature corresponding to the inflexion point of the curve. For the PED materials the crystallization temperature T_c was determined using the exothermic peak during the cooling cycle, while the melting temperature T_{m2} corresponds to the endothermic peak shown in the second heating cycle. In addition, the melting enthalpy ΔH_{m2} of PBT and the mass content of PBT crystallites $w_{c,h}$ were calculated [171; 172; 173].

5.3.2 Dynamic mechanical thermal analysis (DMTA)

DMTA was conducted using a Rheometrics RSA 2 instrument in tension mode. A frequency of 1 Hz over the temperature range of -100 to 170°C with a heating rate of 2K/min in nitrogen environment was used, according to ASTM D5026 [174]. The RSA 2 instrument requires rectangular bars with a thickness of about 0.5 - 0.9 mm. For that, the specimens were cut from the central portion of the micro-dumbbell for testing. The storage modulus (E'), loss modulus (E'') and damping factor ($\tan \delta$) were determined.

5.3.3 Thermal gravimetric analysis (TGA)

TGA was employed to assess the thermal stability of neat polymers and their nanocomposites. TGA was performed using a TA Instrument TGA 500 by heating the material from 25°C to 500 – 800°C at a heating rate of 10K/min with a flow rate of 6 ml/min. Both air and nitrogen were utilized as atmospheres to study thermal degradation with and without the presence of oxygen.

5.4 Mechanical characterization

5.4.1 Quasi-static mechanical testing

Quasi-static tensile tests were carried out with a Zwick Z2.5 universal test equipment with a load cell of 0.5 kN, using a cross-head speed of 100 mm/min for segmented PED multiblock copolymers and 500 mm/min for the IBS block copolymers and their composites. The initial grip distance was set to 10 mm. Measurements were made using automatic and self-tightening clamps to prevent slipping of the micro-dumbbells from the clamps. Tensile tests were performed on the materials under the standard laboratory conditions to evaluate ultimate tensile stress (σ_{ult}) and elongation at break (ϵ_{max}) and the stresses at specific elongation according [175]. All tensile results were averaged from at least three samples.

5.4.2 Dynamic fatigue testing

The hysteresis measurements were carried out on an Instron 8400/8800 servo-hydraulic testing equipment, a 50 N load cell, a 10 kN servo cylinder and a digital controller. The DynMat Hysteresis Measurement Software V.1.1.0.1 (BASF AG) was used for the evaluation of the hysteresis (loading-unloading) loops, as shown in Figure 5.1. The load ratio (R) was kept constant at 0.1. The strain was measured based on the real-time clamp-clamp displacement.

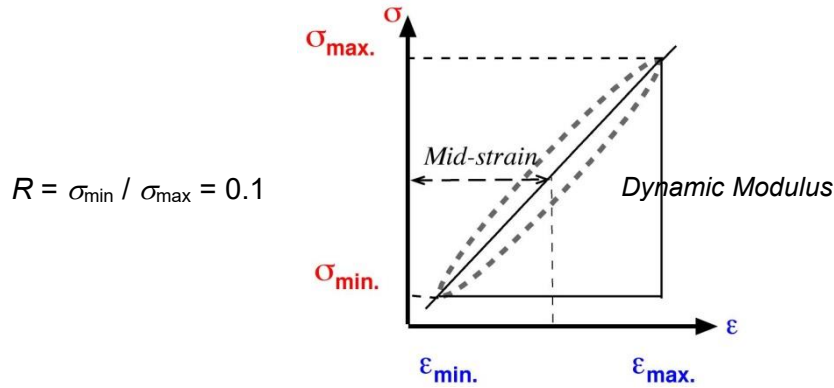


Figure 5.1: Evaluation of dynamic modulus E_{dyn} from a hysteresis loop during fatigue testing [44, 60].

Stepwise Increasing Load Testing (SILT).

Specimens were subjected to a stress-controlled sinusoidal oscillation with $R = 0.1$. The starting value was 5 % of the ultimate tensile stress (σ_{ult}). The stress was kept constant for 1000 cycles before raising it to the next level in 5% intervals. Between every step, an interval of 100 cycles was implemented to allow the controller to reach the higher loading level. The frequency of the cyclic loading was maintained at 1 Hz to simulate the physiological frequency experienced in the human body [104,176,177]. For IBS block copolymers a step size of 1 % in the SILT was chosen primarily to avoid “pinched” hysteresis loops at high strains, as known from Puskas et al. [162].

From the SILT, a critical stress level (σ_L) of a material is determined based on the criterion when the dynamic modulus (E_{dyn}) - the mean slope of the hysteresis loop (see Figure 5.1) decreases by 5% or more within a single stress level. This determined σ_L is then used for the single load test of the material. For testing of the PED multiblock copolymers, a similar procedure was applied, but instead of increasing the load with intervals of 1 % of σ_{ult} , the step size was chosen to be 5% of σ_{ult} , because the materials was more stiff and therefore pinching does not occur for that set of material.

Single Load Test (SLT).

Specimens were subjected to a stress-controlled sinusoidal oscillation of 100,000 cycles at their critical stress level (σ_L), $R = 0.1$ and a frequency of 1 Hz. From the SLT, the dynamic creep (ε_{dc}) was calculated by Eq. 5.1,

$$\varepsilon_{\text{dc}} = \varepsilon_{\text{final}} - \varepsilon_{\text{initial}} \quad \text{Eq. 5.1}$$

Where $\varepsilon_{\text{initial}}$ represents the mid-strain measured after the first 100 cycles, and $\varepsilon_{\text{final}}$ is the final mid-strain value at the end of 100,000 cycles and is also ascribed as the absolute creep [48; 52, 178].

6 Results and discussion

6.1 Influence of e-beam cross-linking on fatigue properties of Poly(aliphatic/aromatic-ester) copolymers (based on [178])

This part of the work focuses on the dynamic creep and fatigue behavior of novel nano-structured PEDs (PBT-26 and PBT-30). In order to enhance the short- and long-term mechanical behavior of PEDs through stiffening of the material, an additional cross-linked network structure was introduced. The cross-linking was achieved by using e-beam irradiation, which promotes cross-linking among polymer chains [114]. The use of e-beam irradiation (0 kGy, 25 kGy, 50 kGy, 75 kGy and 100 kGy) should improve the static mechanical behavior of polymers, but can also yield better dynamic creep and fatigue resistance [107]. First the morphology and the thermal properties of the investigated materials will be clarified, followed by the mechanical characterization in order to get the underlying structure-property-relationship. In addition, a comparison to the benchmark materials Pellethane® and a silicone rubbers will be taken.

6.1.1 Polymer morphology

Figure 6.1 shows the microstructure of PBT-26 and PBT-30 for non-irradiated and irradiated samples. The bright phase is related to the PBT hard phase, whereas the dark phase belongs to the DLA soft phase, which reacts with OsO_4 . In the two non-irradiated samples the phase separation is visible, which is responsible for the strength of the polymer [51, 75]. Different resolutions of TEM images of PBT-26 and PBT-30 are shown, because of the difficulties to stain the samples. In addition, it is worthwhile mentioning that the straight, dark and light regions in Figure 6.1 result from sectioning of the samples and do not reflect or belong to the micro-structure of this material.

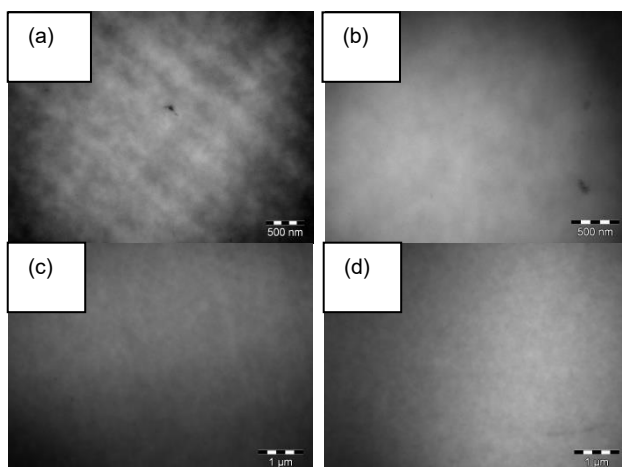


Figure 6.1: Transmission electron micrographs (TEM) of PBT-26_{0kGy} (a), PBT-26_{100kGy} (b) and PBT-30_{0kGy} (c) and PBT-30_{100kGy} (d). The samples were stained using vapor from a 0.2 wt.-% aqueous OsO_4 solution for two hours at room temperature.

The TEM images reveal that phase separation is reduced with increasing dosage of irradiation. The larger amount of the bright phase shows that this can be related to the formation of a cross linked network structure. Phase transitions occur predominantly in hard segments, therefore white phase is related to hard PBT segments. A similar trend holds for PBT-30 (see Figure 6.1). It is reported that at higher soft-phase contents (i.e. 74 wt.-%) a more homogeneous structure compared to the microphase separated structure like PBT-30 (with 70 wt.-% soft

segments) exists [51]. This effect is visible by comparing PBT-26 and PBT-30. In order to investigate the microstructure of the PED polymers in more detail AFM measurements were applied, because TEM only showed the reported effects very unincisive. The AFM images of the two extreme, PBT-30_{0kGy} and PBT-30_{100kGy} reveal the influence of e-beam radiation on the polymers (Figure 6.2).

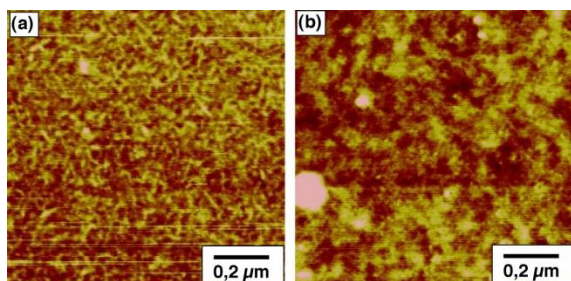


Figure 6.2: Two-dimensional atomic force micrographs (AFM) of PBT-30_{0kGy} (a) and PBT-30_{100kGy} (b). Images with a size of $1 \times 1 \mu\text{m}^2$ were acquired in tapping mode.

Phase separation results in hard phase domains (bright) and soft phase domains (dark). The neat polymer shows a well ordered structure of hard phase domains. In comparison the irradiated polymer has larger bright domains, which look like agglomerations of the bright phase. This effect can be related to the e-beam irradiation, which takes place after the polymerization and introduces crosslinks into the copolymer. In addition, the samples are slightly heated during the irradiation process. Therefore, larger connected domains can undergo room temperature annealing and agglomerate, because of the enhanced micro-mobility of the polymer chains at higher temperatures [75,179] and enhances the phase separation. These results also support the statement that the cross-linking predominantly occurs between the hard phases (see also Chapter 6.1.2). Furthermore, it is concluded that e-beam irradiation randomly breaks and reconnects bonds within the polymer [180]. Hence the micro-structure of the irradiated polymer consists of large interconnected domains while, the neat polymer has a more regular structure.

6.1.2 Thermal properties

6.1.2.1 Differential scanning calorimetry (DSC)

Table 6.1 summarizes the thermal properties of PBT-26 and PBT-30. The glass transition temperature T_{g1} is only moderately influenced by the content of the hard phase. However, the increase in T_C and ΔH_{m2} for PBT-30 is caused by the larger concentration of the crystalline phase. In addition, the calculated degree of crystallinity $w_{c,h}$ is rather low (6.9 - 8.7%).

Table 6.1: Temperature transitions determined with differential scanning calorimetry for PBT-26 and PBT-30 with and without e-beam irradiation.

Sample	Soft segments	Hard segments				
	T_{g1} [°C]	T_{g2} [°C]	T_{m2} [°C]	ΔH_{m2} [J/g]	T_{C2} [°C]	$w_{c,h}$ [%]
PBT-26 (0 kGy)	-43.7 ± 0.3	57.3 ± 0.6	115.1 ± 0.4	8.9 ± 0.2	27.4 ± 0.5	6.9 ± 0.2
PBT-26 (25 kGy)	-43.9 ± 0.2	49.9 ± 0.4	114.1 ± 0.5	9.2 ± 0.1	22.4 ± 0.2	5.8 ± 0.3
PBT-26 (50 kGy)	-43.6 ± 0.3	51.1 ± 0.6	114.1 ± 0.2	9.1 ± 0.2	22.9 ± 0.6	6.2 ± 0.3
PBT-26 (75 kGy)	-43.6 ± 0.4	50.3 ± 0.3	114.5 ± 0.5	6.6 ± 0.3	22.3 ± 0.3	5.8 ± 0.2
PBT-26 (100 kGy)	-43.0 ± 0.1	50.0 ± 0.3	114.2 ± 0.4	8.0 ± 0.3	22.5 ± 0.2	5.8 ± 0.4
PBT-30 (0 kGy)	-42.6 ± 0.1	49.0 ± 0.4	124.1 ± 0.4	8.7 ± 0.4	52.1 ± 0.4	8.4 ± 0.4
PBT-30 (25 kGy)	-41.9 ± 0.4	50.3 ± 0.2	128.3 ± 0.4	9.2 ± 0.4	52.3 ± 0.4	8.2 ± 0.4
PBT-30 (50 kGy)	-42.5 ± 0.3	50.5 ± 0.3	125.2 ± 0.4	9.7 ± 0.4	51.3 ± 0.4	8.3 ± 0.4
PBT-30 (75 kGy)	-42.1 ± 0.3	49.5 ± 0.4	124.2 ± 0.4	10.2 ± 0.4	52.4 ± 0.4	8.7 ± 0.4
PBT-30 (100 kGy)	-41.9 ± 0.2	50.7 ± 0.4	126.2 ± 0.4	9.9 ± 0.4	52.4 ± 0.4	8.2 ± 0.4

The T_{g1} only decreases with increasing dosage of irradiation for PBT-26, but not for PBT-30, but with respect to the standard deviation these changes are negligible. Irradiation influences the T_{g2} values, but significant differences can be seen for PED-26, where T_{g2} decreases from $57.3 \pm 0.6^\circ\text{C}$ for the unirradiated material, to around 50 to 51.1°C , for the irradiated specimens, what can be explained by the effect of the lack of a strong segmental interactions stabilizing the nanostructure at the molecular level. A similar effect is visible for the crystallinity, which only is significantly decreasing for irradiated PBT-26 compared to neat PBT-26. These results indicate that crosslinking predominantly occurs in the hard PBT phase, rather than in the soft DLA segment. With increasing radiation dose, the random polymer structure may favor formation of longer PBT segments to initiate more entanglements and hence requires more thermal agitation to achieve the glass transition. Therefore, the degree of crystallinity is also reduced. For polymers containing 30 wt.-% hard segments, e-beam irradiation slightly increases T_{m2} of PBT. This trend does not apply to all results in Table 6.1, since e-beam irradiation does not only initiate crosslinking, but also cause polymer chain scission and material degradation. In addition, the use of e-beam irradiation does not affect the crystallization behavior of PBT as indicated by the inconsiderable change of T_C in Table 6.1.

6.1.2.2 Dynamic mechanical thermal analysis (DMTA)

In order to establish the presence and quantify the extent of cross-linking, DMTA measurements were carried out. Under loading conditions, the effect of crosslinking is expected to be more pronounced. Figure 6.3 presents the storage modulus (E') and loss modulus (E'') of neat PBT-26 as well as the irradiated PBT multiblock copolymers.

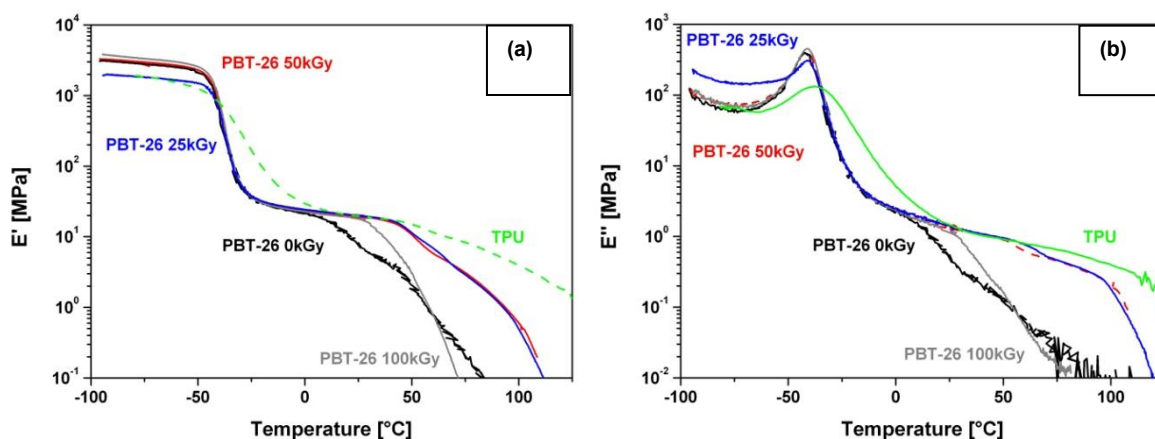


Figure 6.3: E' (a) and E'' (b) of Pellethane®, PBT-26, PBT-26(25kGy), PBT-26(50kGy) and PBT-26(100kGy).

From the trace of the storage modulus (Figure 6.3(a)) and the peaks of the loss modulus (Figure 6.3(b)), one can clearly observe two transition temperatures. For all investigated PBT-26 copolymers the first transition (T_{g1}) is located near to -41°C and is ascribed to the glass transition temperature of soft segments. The second glass transition (T_{g2}) at around 30°C for neat PBT-26 can be associated with the PBT hard phase segment. At the dosages of 25 kGy and 50 kGy, the T_{g2} of irradiated PBT-26 is shifted to 50°C . From these, one can conclude that the e-beam irradiation did, in deed, create cross-linkages in the material, which will have an impact on the mechanical properties of both irradiated PBT-26 and PBT-30 (see Chapter 6.1.3). Furthermore, it is evident that the cross-linkages occurs predominantly within the PBT hard phase, because there is no difference observed in the T_{g1} of the amorphous soft segment containing DLA. From the reduction of the second transition, when the dosage is further increased (100 kGy) one can conclude that degradation due to irradiation take place, which is also seen when comparing the static mechanical properties (see Table 6.2). As to Pellethane®, the irradiated PEDs have the comparable range of E' at around 37°C where both materials are expected to perform in human body.

6.1.3 Mechanical characterization

6.1.3.1 Tensile properties

As seen from the DMTA analysis of the different neat and irradiated PEDs, the possible onset of cross-linking due to e-beam irradiation is also expected to have a positive impact on the mechanical performance. Therefore, a screening of the material mechanical behavior was performed in order to study how e-beam irradiation and the formation of the network structure affects the tensile properties. Table 6.2 presents the results for E_{mod} , σ_{max} and ϵ_{max} . Comparing the neat materials, an overall improvement in the mechanical behavior (σ_{max} and ϵ_{max}) can be observed with increasing fraction of the hard phase. The increase of ϵ_{max} can be related to the microstructure of the polymer, since the higher soft-phase content of PBT-26 yields a more

homogeneous structure than the microphase separated structure of PBT-30 [51]. In addition, PBT-30 is stiffer than PBT-26, since the Young's modulus increases from 7.7 MPa to 13.5 MPa (Table 6.2). These results reveal the favorable contribution of a higher concentration of the hard phase (PBT) to enhance the mechanical response of the material as it is generally accepted for thermoplastic elastomers (the stiffness increases with content of hard segments [75]).

Table 6.2: Static tensile properties of PEDs, TPU and silicone. The geometry of the samples was chosen according to ASTM D 1708-06a. The cross-head speed was 100 mm/min. The ultimate tensile strength is denoted by σ_{\max} , the elongation at break by ϵ_{\max} and the Young's modulus by E.

Sample	E [MPa]	σ_{\max} [MPa]	ϵ_{\max} [%]
PBT-26			
0 kGy	7.7 ± 0.2	3.8 ± 0.1	512 ± 17
25 kGy	8.4 ± 0.8	4.0 ± 0.2	563 ± 101
50 kGy	8.3 ± 0.1	3.9 ± 0.1	580 ± 50
75 kGy	8.0 ± 1.1	4.3 ± 0.2	534 ± 87
100 kGy	7.7 ± 0.5	4.7 ± 0.3	832 ± 92
PBT-30			
0 kGy	13.5 ± 0.7	6.1 ± 0.2	790 ± 30
25 kGy	13.6 ± 0.1	6.6 ± 0.3	838 ± 76
50 kGy	13.9 ± 0.4	7.4 ± 0.2	901 ± 10
75 kGy	14.1 ± 0.3	7.2 ± 0.2	790 ± 80
100 kGy	13.1 ± 0.3	7.3 ± 0.3	895 ± 50
PBT-26 α^*			
0 kGy	7.2 ± 0.3	4.0 ± 0.2	607 ± 28
25 kGy	7.0 ± 0.3	3.6 ± 0.1	447 ± 68
50 kGy	7.8 ± 0.4	4.1 ± 0.2	657 ± 81
75 kGy	8.0 ± 0.2	4.0 ± 0.1	659 ± 53
100 kGy	7.5 ± 0.3	4.0 ± 0.1	620 ± 47
PBT-30 α^*			
0 kGy	12.5 ± 0.8	5.6 ± 0.1	664 ± 25
25 kGy	13.1 ± 0.8	5.8 ± 0.2	722 ± 76
50 kGy	13.5 ± 0.7	6.5 ± 0.4	790 ± 102
75 kGy	12.3 ± 0.7	5.8 ± 0.3	690 ± 51
100 kGy	12.4 ± 0.3	5.6 ± 0.2	597 ± 69
TPU			
0 kGy	26.4 ± 0.3	52.9 ± 4.8	910 ± 21
25 kGy	26.9 ± 0.5	42.4 ± 1.2	891 ± 86

50 kGy	_**	_**	_**
75 kGy	25.3 ± 1.3	32.6 ± 5.2	786 ± 129
100 kGy	_**	_**	_**
Silicone			
	2.3 ± 0.2	10.2 ± 0.8	1034 ± 91

* α = α -tocopherol (stabilizer)

** No useable results were obtained, due to slippage of the tensile bars during testing.

Figure 6.4 shows the stress-strain curves of the polymers used within this study. Both, PBT-26 and PBT-30 have a relatively high elongation at break, which can be related to the long chain aliphatic DLA segments, used as the soft phase within the TPEs. In addition, the PEDs do not depict a typical rubber-like behavior similar to the benchmark materials silicone and TPU, which are characterized by a chemical (silicone) or a physical network structure reinforced with hydrogen bonding (TPU). The presence of additional hydrogen bonds in the TPU is responsible for the high tensile strength, whereas different hardening additives are responsible for the tensile strength of silicone. We emphasize that synthesized PED copolymers do not contain any additives or even thermal stabilizers, and still display very good mechanical properties [48,50,51].

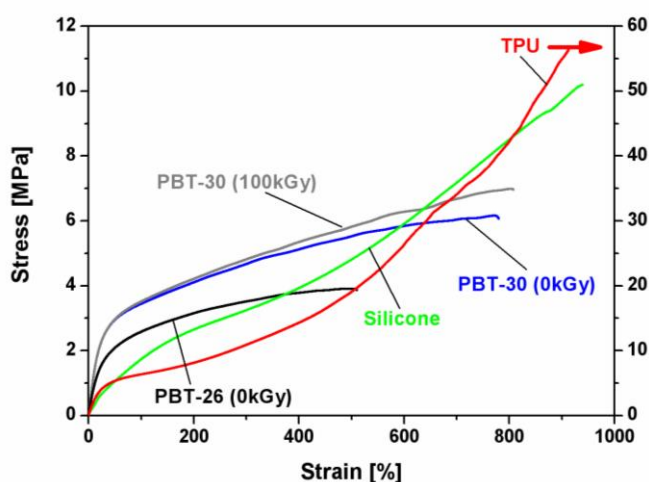


Figure 6.4: Stress-strain tensile curve of PBT-26, PBT-30 with 0 kGy and 100 kGy of e-beam irradiation, Silicone and TPU. The measurements were performed on 1 mm thin films with a cross-head speed of 100 mm/min.

Table 6.2 and Figure 6.4 show that the use of e-beam irradiation and the amount of irradiation dosage increases σ_{\max} and ϵ_{\max} of the materials via the formation of the cross linked network structure. E-beam irradiation has only a minor effect on E_{mod} of PBT-26 (see Table 6.2) and PBT-30 (see also Figure 6.4).

E-beam irradiation essentially creates free radicals along the polymer chains. These free radicals can be re-combined to form crosslink's. However, the resulting free radicals can also react with the oxygen bi-radicals, which lead to oxidation and other related free radical reactions. This effect can cause polymer chain scission and material degradation [115]. The onset of material degradation explains the drastic drop in σ_{\max} and ϵ_{\max} of TPU (see Table 6.2) and the color change (yellowing) of the material with various dosages of e-beam irradiation.

Because of possible e-beam induced degradation, α -tocopherol was added for stabilization of the PED copolymers [181, 182,183]. The tensile curves as well as the summary of the mechanical tensile performance of original and modified PBT-26 in Figure 6.5 and Table 6.2

show that the use of α -tocopherol as a stabilizer does not affect the mechanical tensile performance. Even e-beam irradiation does not change the tensile properties of PBT-26 modified with α -tocopherol [180].

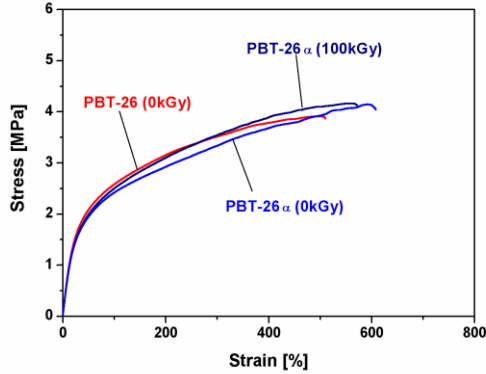


Figure 6.5: Stress-strain tensile curve of PBT-26, PBT-26 $_{\alpha}$ 0kGy and PBT-26 $_{\alpha}$ 100kGy. The measurements were performed on 1 mm thin films with cross-head speed of 100 mm/min.

6.1.3.2 Dynamic fatigue performance (SILT and SLT)

The tensile strength σ_{\max} is a necessary parameter for calculating the different loading steps in the fatigue measurements. Figure 6.6 presents the σ_{\max} values for PBT-26 and PBT-30. PBT-26 as well as PBT-30 have an increased tensile strength, resulting from the e-beam irradiation dosage of 50 kGy and therefore are taken for further investigations.

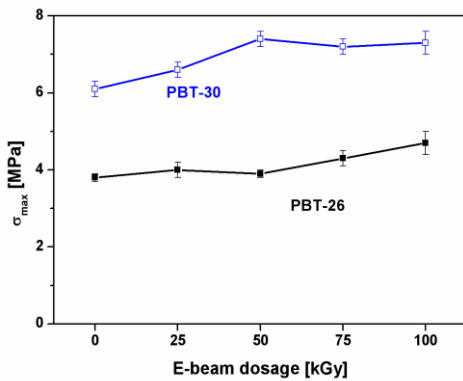


Figure 6.6: Ultimate tensile strength (σ_{\max}) of the neat and irradiated PBT-26 and PBT-30.

Based on the measured tensile strength σ_{\max} the different loading steps have been defined to start at 5 % of the ultimate tensile strength and will be raised in steps of 5 %.

Figure 6.7 provides the dynamic modulus E_{dyn} results during the SILT of TPU, neat PBT-26 and PBT-30 and both irradiated with a dosage of 50 kGy. For PBT-26 and PBT-30 systems, the dynamic E_{dyn} is higher than the static values ($E_{\text{mod}}^{\text{PBT-26}} = 7.7$ MPa, $E_{\text{mod}}^{\text{PBT-26}_{50\text{kGy}}} = 8.3$ MPa, $E_{\text{mod}}^{\text{PBT-30}} = 13.5$ MPa, $E_{\text{mod}}^{\text{PBT-30}_{50\text{kGy}}} = 13.9$ MPa), which can be related to the viscoelastic response of the material to the higher loading velocity during dynamic loading than during quasi-static testing.

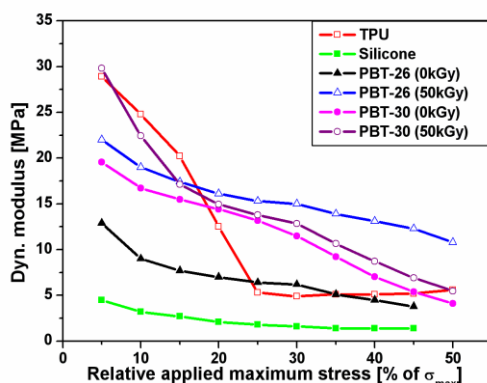


Figure 6.7: Dynamic modulus E_{dyn} as a function of relative applied maximum stress for silicone, TPU, neat PBT-26, PBT-26_{50kGy}, neat PBT-30 and PBT-30_{50kGy} (SILT).

Figure 6.7 reveals that the neat PBT-26 has a lower E_{dyn} than the commercial TPU. However after the 5th load level (5,000 cycles), the neat PBT-26 even exhibits a higher dynamic modulus and does not depict from such a drastic drop like TPU. Polyurethane samples generally show higher initial E_{dyn} values, which drop faster with increasing load levels [50,184]. Takahara et al. suggested that under cyclic loading the destruction of the hard segment domain or a mixing of the hard and soft segment occurs [185, 186]. Based on the afore mentioned, PBT-26 is more resistant to fatigue than TPU. Comparison of irradiated PBT-26 reflects that at low stress levels, the irradiated PBT-26 has an improved dynamical performance, which is comparable to commercial TPU. Similar to the neat PBT-26, the irradiated material shows no drastic drop of E_{dyn} and outperforms TPU after 3,000 cycles. This positive effect is related to the crosslinking due to e-beam irradiation, which introduces additional chemical bonds between the backbone chains to stiffen the material. As expected for PBT-30 the dynamic modulus E_{dyn} is increased compared to PBT-26 because of the higher amount of the PBT hard phase. Irradiation of PBT-30 causes an increase of E_{dyn} , similar to commercial TPU. During the first two loading levels, E_{dyn} strongly drops. Similar to TPU this drop can be related to the destruction of the hard segment domains. As this drop does not occur within the neat PBT-30 this effect can be explained by the formation of crosslinks. DSC measurements – discussed in Section 5.1.2.2 – already indicated that these crosslinks are predominantly in the PBT hard phase. Furthermore, it is obvious that irradiated PBT-26 has a much lower deformation at the same loading level than the neat material and commercial TPU (see Figure 6.8). A similar effect can be observed for the neat and irradiated PBT-30. The lower the soft phase content, the lower is the susceptibility to dynamic creep [51]. Therefore, the reduction of the deformation during the dynamic loading of the SILT methodology, due to e-beam irradiation is not as pronounced as for PBT-26.

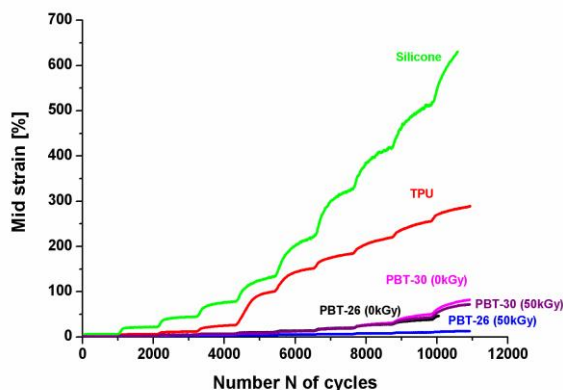


Figure 6.8: Mid strain as a function of number N of cycles for silicone, TPU, neat PBT-26, PBT-26_{50kGy}, neat PBT-30 and PBT-30_{50kGy} (SILT).

When the micro domains are destroyed, TPU creeps more severely within each loading level. Hence, the neat PBT-26 is also more susceptible to creep than PBT-26_{50kGy}, because PBT-26 breaks before PBT-26_{50kGy}. This also holds for PBT-30. The chains of the irradiated PED have lesser possibilities to slide against one another, due to the formation of crosslinks and lower amount of energy is dissipated by hysteretic heating, which is caused by the friction of polymer chains against each other [145].

A review of the damping characteristics of the materials during SILT also underlines that e-beam irradiation enhances the dynamic performance of the PED (see Figure 6.9). The damping is defined as the area, which is covered by a hysteresis loop [49]. A higher damping is related to higher loss of energy. The energy can be dissipated due to hysteretic heating and the formation of micro cracks, which creates new surfaces [179]. PBT-26 shows the highest damping value followed by neat PBT-30. This behavior indicates, that at such compositions (only 26 wt.-% of hard segments), the material creeps due to the missing of strong segmental interactions, to stabilize the nanostructure at the molecular level. Therefore, a highly homogeneous rather than a microphase separated structure is expected for these polymers. The difference between PBT-26 and PBT-30 indicates that the structure of PBT-26 is even more homogeneous than the structure of PBT-30. Both irradiated polymers show a decreased value of damping, which can be explained by the formation of a higher degree of microphase separation due to e-beam irradiation. Hence, e-beam irradiation improves the fatigue resistance of the multiblock polyester copolymers especially for lower loading cycles by reducing the damping. Because of the additional crosslinks, more bonds have to be broken to create cracks for energy dissipation. For all loading levels, PBT-26_{50kGy} exhibits nearly the same damping behavior, whereas the TPU has a notable increasing damping value after each load level. Both neat and irradiated PEDs show a mild increasing trend in damping.

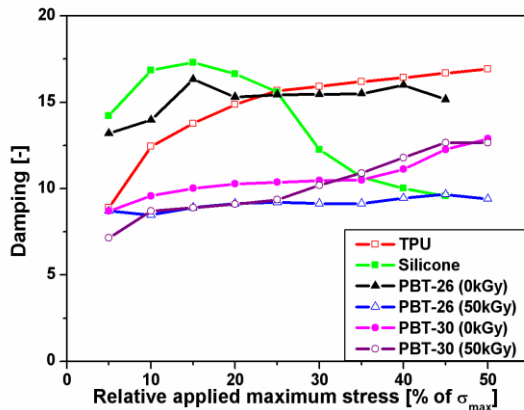


Figure 6.9: Damping versus number N of cycles for silicone, TPU, neat PBT-26, PBT-26_{50kGy}, neat PBT-30 and PBT-30_{50kGy} (SILT).

Analyzing the data of Figure 6.7 the critical load level is set at the 4th load level. In this interval, E_{dyn} drops more than 5 % within one loading level. For the following SLT measurements the appropriate load is applied and Figure 6.10 shows the results for different material systems.

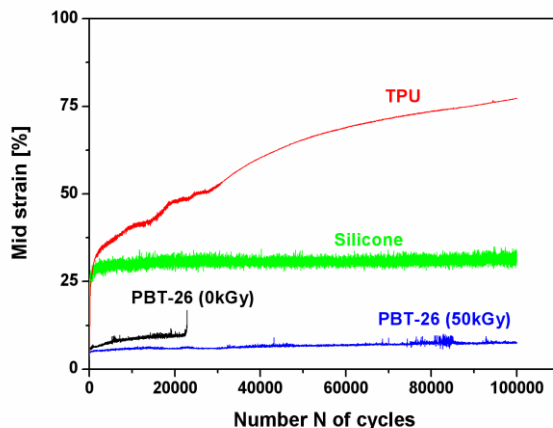


Figure 6.10: Dynamic creep for silicone, TPU, neat PBT-26 and PBT-26_{50kGy} measured by the single load test (SLT) methodology. The test frequency was 1 Hz, the number of cycles N was 100.000 and $T = 24^{\circ}\text{C}$.

Non-irradiated PBT-26 already breaks after around 22 000 cycles, while irradiated PBT-26 sustains the loading conditions up to 100,000 cycles. This is consistent with the SILT results, where the non irradiated PBT-26 also does not sustain all load levels. A pronounced creep of the segmented TPU system is visible over 100,000 cycles. The different steps can be explained by the destruction of the micro domains [187]. In the PBT materials these domains are not destroyed. Consequently, the PBT material is less sensitive to dynamic creep than the TPU system and the silicone, see Figure 6.11.

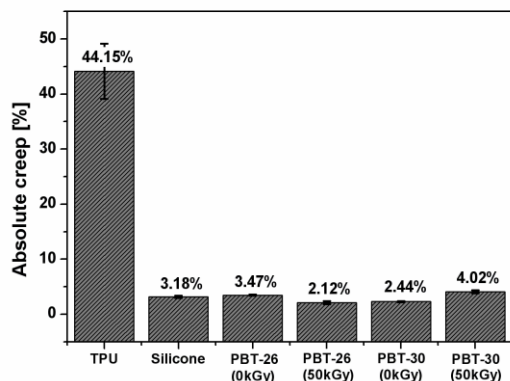


Figure 6.11: Absolute creep $\Delta\varepsilon$ of PED copolymers, silicone and TPU. The test parameters were: frequency = 1 Hz, number of cycles $N = 100,000$ and $T = 24$ C.

The irradiated PBT-26 shows a lower susceptibility to dynamic creep than the neat polymer and even lower than all other materials. This decrease of the absolute creep is related to the formation of crosslinks due to e-beam irradiation. By introducing an additional network, a stable polymer structure is formed. During the dynamic loading the number of entanglements decreases and the chemical bonds are responsible for carrying the load. Since more chemical bonds have to break before the sample ruptures and is destroyed the irradiated PBT-26 sustains the whole loading pattern while PBT-26 breaks at a smaller number of cycles (see Figure 6.10). Due to the double physical and chemical network structure the final elongation of the sample is also decreased and the dynamic creep behavior is improved. In comparison, the neat PBT-30 sustains all loading cycles without breakage as well as irradiated PBT-30. The absolute creep of neat PBT-30 is smaller than the absolute creep for the neat and irradiated PBT-26, which indicates that with lower soft phase content the susceptibility to creep is also smaller [51]. In addition, the absolute creep of neat PBT-30 is smaller than for irradiated PBT-30. This result underlines the conclusion that crosslinking mainly occurs in the PBT hard phase. In comparison to PBT-26 a dosage of 50 kGy is not sufficient to improve the dynamic creep behavior of PBT-30. It is worthwhile to mention, that the applied loading level during the SLT of irradiated PBT-30 is slightly higher than for the non-irradiated PBT-30, while the applied loads were nearly equal for PBT-26. Therefore, it is reasonable, that irradiated PBT-30 has a slightly higher absolute creep value than the non-irradiated one. In addition, no destruction of the microstructure is visible because no steps or a rapid growth during the strain measurements can be detected, similar to the SLT of PBT-26.

6.1.4 Summary

The dynamic creep and fatigue performance of novel nano-structured poly(aliphatic/aromatic-ester) multiblock copolymers (PEDs) with various dosages of e-beam irradiation was investigated. DSC measurements indicated that crosslinking mainly occurs within the PBT hard phase, shown by the slight increase of T_{m2} and the decrease of the crystallinity. It was found that the introduction of the additional network influences the microstructure. For PED, the increase of irradiation dosage leads to the formation of PBT hard phase aggregates, which has a reinforcement effect on the material. This formation of an additional cross linked network in the polymer is responsible for improving the quasi-static mechanical properties of these PED multiblock copolymers.

As expected, the improvement in the mechanical performance was also observed in the fatigue and creep behavior of irradiated PEDs compared to the neat PEDs, TPU and silicone.

Particularly, the irradiated materials, show a less drastic drop of E_{dyn} as compared to TPU and were more resistant to creep. In addition, the irradiated PEDs were more resilient against micro-scale damage to lower damping. Therefore, thermoplastic elastomers, especially PED multiblock copolymers can be considered as good candidates for medical applications, where materials are subjected to oscillatory deformations.

6.2 Influence of a chemical network structure on the material performance of (soft) polyisobutylene-based thermoplastic elastomers (based on [188])

For this study, three different D_IBS polymers were investigated. L_SIBS (SIBSTAR 073T) was provided by the Kaneka Corporation. Table 6.3 lists the materials. L_SIBS31 refers to the L_SIBS sample with 31 wt% PS, while D_IBS27 stands for the branched polymer that contains 27 wt% PS. The average number of end blocks or “arms” (N) in the branched samples is calculated as B+2 where B is the average number of branches per chain obtained from polymerization kinetics as reported [121]. A medical-grade silica-reinforced crosslinked silicone rubber (MED 4050 - Nusil Technology) was used as a control, because this is the only material approved for breast implant shells by the US Food and Drug Administration and the research is focusing on this topic.

Table 6.3: Materials used in the current study.

Material Designation	Hard (PS) phase [wt%]	M_n [g/mol]	\bar{D} (M_w/M_n)	N*
L_SIBS31	31	67,000	1.2	2
D_IBS33**	33	70,000	4.5	4
D_IBS27	27	178,000	2.7	4
D_IBS16 **	16	119,000	2.4	3

* Number of arms; rounded numbers; ** Puskas, 2009a

It was difficult to design the PIB-based block copolymers for comparative studies. If the total block copolymer molecular weight (M_n) is kept constant, increasing PS content would reduce the molecular weight of the PIB core (M_n^{PIB}). If the M_n^{PIB} is kept constant, the M_n will increase with increasing PS content. However, it was shown that the ultimate tensile strength of L_SIBS with two PS “arms” scaled with the molecular weight of the PS arms [$M_n^{\text{PIB}(\text{arm})}$] and reached the maximum strength at about 12,000 – 16,000 g/mol [189]. When branching introduces more than two end blocks (arms) at the same PS content, the $M_n^{\text{PS}(\text{arm})}$ of each PS block would be reduced. In the material matrix shown in Table 6.3, three block copolymers with ~30 wt% total PS content have been used: one linear polymer with two end blocks (arms), and two branched polymers with an average of four end blocks (arms). L_SIBS31 and D_IBS33 have similar M_n , but the latter is branched leading to a broader molecular weight distribution (MWD) and hence increased dispersity index. D_IBS27 has much higher M_n than the other materials. Table 6.4 summarizes $M_n^{\text{PS}(\text{arm})}$, M_n^{PIB} , and $M_n^{\text{PIB}(\text{arm})}$ for each material. The molecular weight of the PIB [$M_n^{\text{PIB}(\text{arm})}$] or PS [$M_n^{\text{PS}(\text{arm})}$] arm was calculated by dividing M_n^{PIB} or M_n^{PS} by the number of arms/end blocks (N). As shown in Table 6.4, the $M_n^{\text{PS}(\text{arm})}$ of the polymers increases in the order of D_IBS33 (6,000 g/mol), L_SIBS31 (10,000 g/mol) and D_IBS27 (12,000 g/mol). With an average of three end blocks, D_IBS16 has a $M_n^{\text{PS}(\text{arm})}$ of 6,000 g/mol and the same $M_n^{\text{PS}(\text{arm})}$ as D_IBS27. These material matrix and information (Table 6.3 and Table 6.4) will be used to gain insight into the structure-property relationships of PIB-based block polymers as important emerging biomaterials [104, 73, 190, 160]. Medical grade silicone rubber was used as a control for the comparison of static and dynamic mechanical properties.

Table 6.4: PIB-based block copolymer matrix.

Material	$M_n^{\text{PS(arm)}}$ [g/mol]	Soft block		Domain Size [nm]
		M_n^{PIB} [g/mol]	$M_n^{\text{PIB(arm)}}$ [g/mol]	
L_SIBS31	10,000	46,000	23,000	27 ± 4
D_IBS33	6,000	47,000	12,000	39 ± 10
D_IBS27	12,000	130,000	33,000	66 ± 13
D_IBS16	6,000	100,000	33,000	36 ± 8

M_n data: numbers rounded up to the nearest thousands; domain size measured using TEM: $n = 40$

6.2.1 Polymer morphology

Figure 6.12 shows TEM images of samples microtomed from compression molded sheets, stained with RuO_4 . The darker regions correspond to the hard PS phases and the lighter regions correspond to the continuous PIB phase [121]. From Figure 6.12, all four polymers show distinct microphase separated morphology; Table 6.4 lists the average size of the PS domains. Storey and Baugh reported that solution cast films of L_SIBS with 19.2 – 33.7 wt% PS have hexagonally packed cylinders of PS dispersed in the PIB matrix [191]. Figure 6.12 (a) shows a similar ordered packing of the PS domains but with lesser long-range order on account of the sample processing (compression molding).

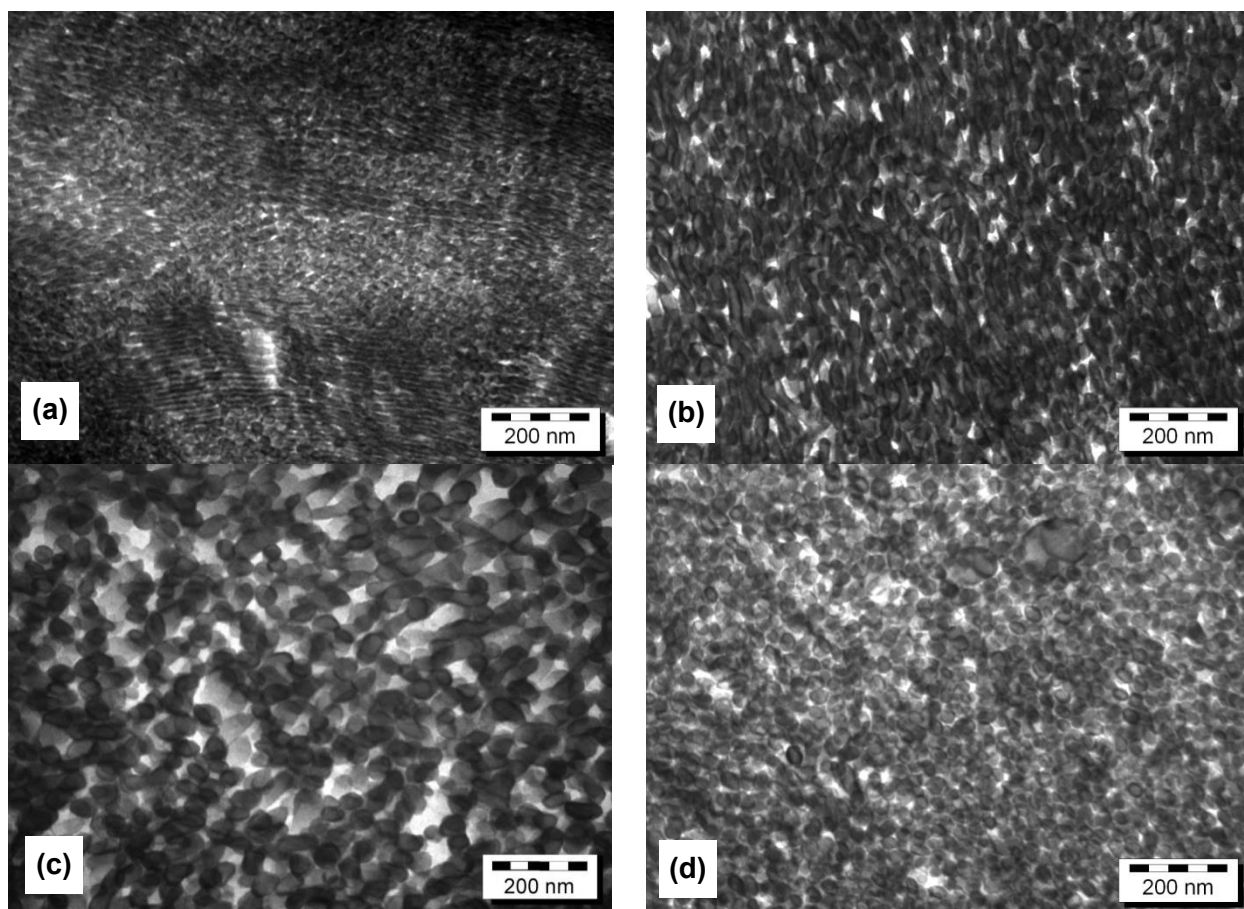


Figure 6.12: TEM images of microtomed and stained (a) L_SIBS31, (b) D_IBS33 (TPE_4), (c) D_IBS27 and (d) D_IBS16 (TPE_2).

The TEM images of the branched polymers appear to indicate a more 3D-like structure of the PS phases, which is most apparent in D_IBS27. At ~30 wt% PS content, L_SIBS31 has the smallest PS domain size, in spite of its higher $M_n^{PS(\text{arm})}$ than that of D_IBS33. The PS domain size of D_IBS27 is more than twice as large as that of L_SIBS31, in spite of the lower PS content and similar $M_n^{PS(\text{arm})}$. Comparison of the three branched samples shows that the domain size scales with the $M_n^{PS(\text{arm})}$ (see also Table 6.4).

6.2.2 Thermal properties

The thermal transition behavior of IBS block polymers was investigated by both DSC and DMTA. In these IBS block polymers, the glass transition of the hard PS and soft PIB phase are expected to be at -65°C and 100°C, respectively [192]. However, the DSC technique was unable to well define the glass transition of the PS phase, even when performed at much higher heating rates of 100K/min or under high pressure from independent study. With the DMTA technique, polymer chains are perturbed not only thermally through the temperature sweep, but also mechanically through the oscillatory deformation. In this way, the long-range coordinated molecular or segmental motion of a polymer chain associated with the glass transition [193] can be detected more readily by DMTA. Figure 6.13(a) – (c) present E' , E'' and $\tan \delta$ plots over the range of the applied temperature sweep. Table 6.5 lists the two major thermal transition temperatures represented by the peaks in the E' plots in Figure 6.13(b). In Figure 6.13(c), two additional secondary relaxation peaks can be observed for the PIB phase. Hill and Dissado attributed these secondary peaks of PIB to the relaxation of chain clusters with different rigidities and structural orders [194]. Figure 6.13(c) shows a high temperature transition of L_SIBS31 at 103.1°C, corresponding to the T_g of the PS phase. There is an additional relaxation process at a higher temperature that has not been observed earlier in L_SIBS samples. Up to know, no explanation for the origin of this secondary transition could be established. Interestingly, the single high thermal transitions in D_IBS27 and D_IBS33 shifted to ~120°C (the high thermal transition in D_IBS16 is very weak, due to the low PS content). This can be related to the greater segmental restriction of the polymer chains due to the branched PIB core as illustrated in Figure 6.14.

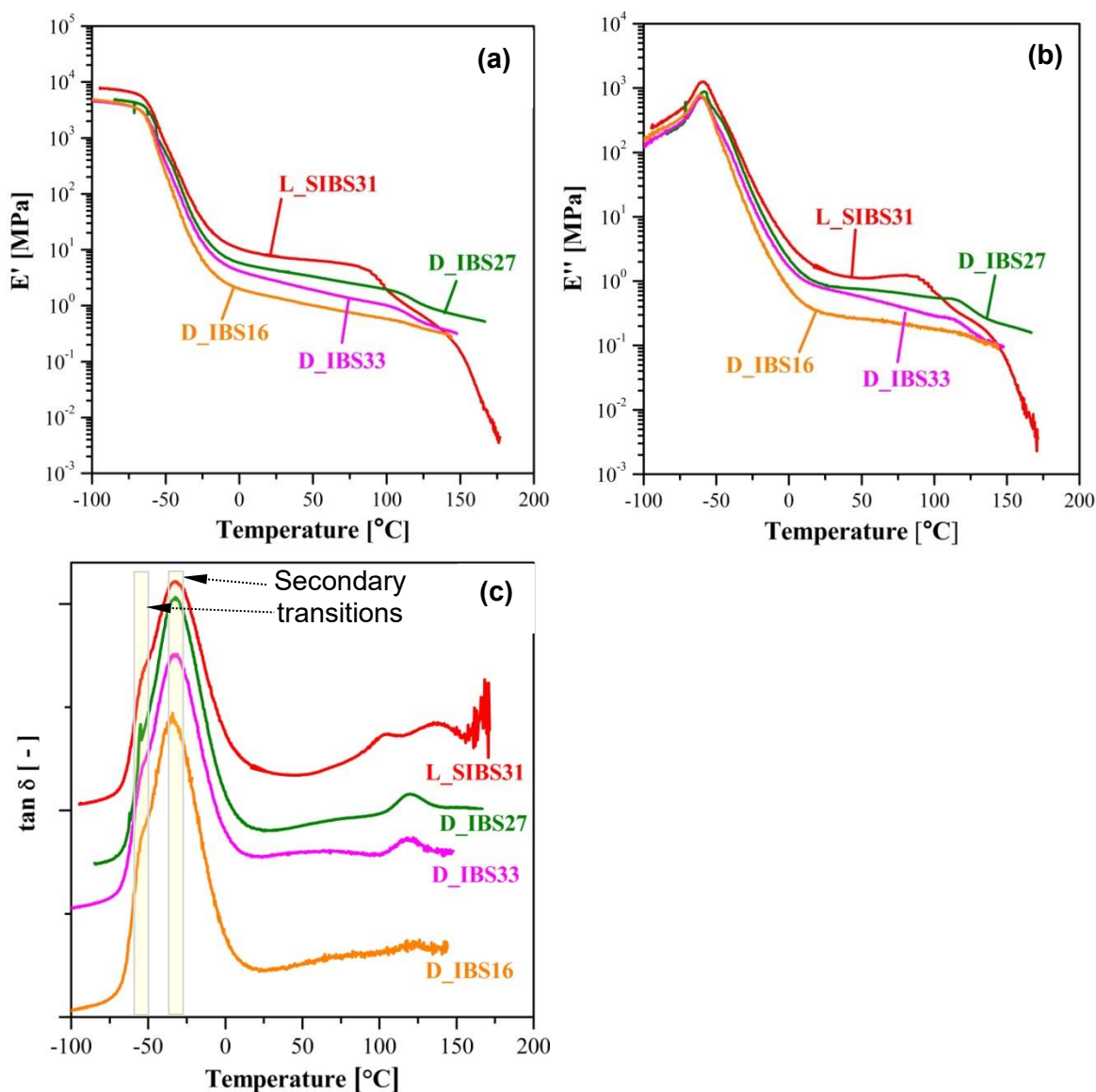


Figure 6.13: The effect of hard phase content and material topology on the dynamic mechanical properties of IBS block copolymers: (a) storage modulus, E' , (b) loss modulus, E'' , and (c) $\tan \delta$

Table 6.5: T_g of IBS block copolymers by DMTA.

Material	T_g^{PIB} (°C)	T_g^{PS} (°C)
L_SIBS31	-59.0	103.1
D_IBS33	-60.1	119.4
D_IBS27	-58.5	119.0
D_IBS16	-61.0	121.9

* T_g of PIB and PS standards are -65.0°C and 100°C, respectively [191].

This likely is a contributing factor to the lower ultimate tensile strength of the branched TPEs (see also Chapter 6.2.2). The higher transition, on the other hand, provides the possibility of

higher service temperatures and sterilization by dry heating or steam used by the medical device manufacturers.

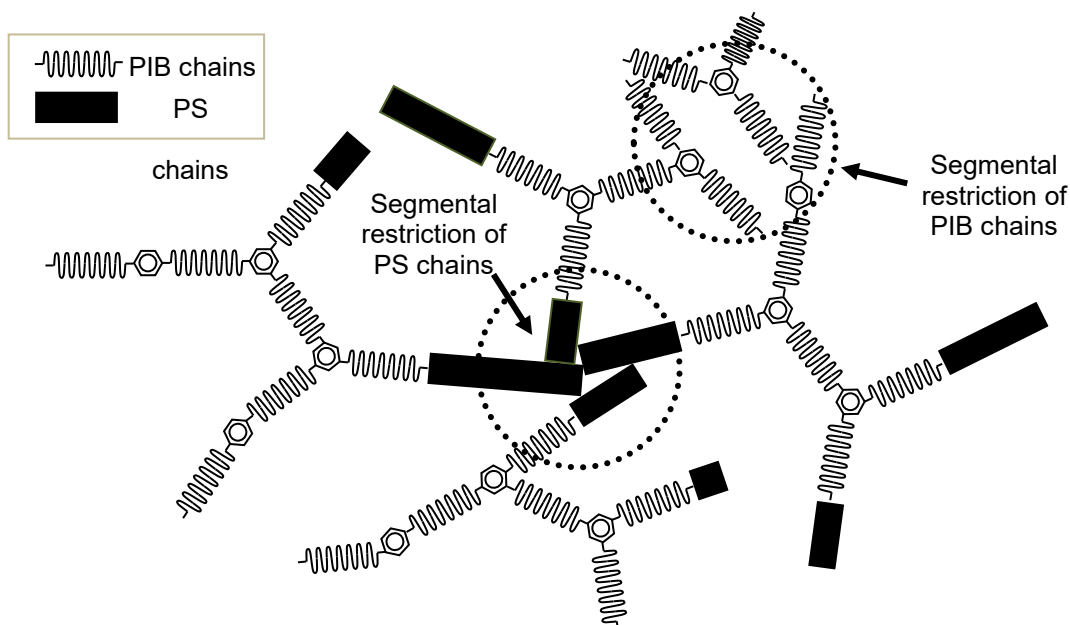


Figure 6.14: Segmental restriction of both PS and PIB chains in the D_IBS polymers.

6.2.3 Mechanical characterization

6.2.3.1 Tensile properties

The phase-separated microstructure of thermoplastic elastomers is responsible for their rubber-like behavior with large elongation when stretched [75, 195].

Table 6.6 shows the quasi-static tensile data and Figure 6.15 the representative stress-strain plots of the investigated samples.

Table 6.6: Quasi-static tensile data.

Material	σ_{ult} [MPa]	ε_{max} [%]
L_SIBS31	13.1 ± 0.4	440 ± 41
D_IBS33 *	5.8 ± 0.1	490 ± 11
D_IBS27	8.8 ± 1.1	620 ± 31
D_IBS16 *	6.3 ± 0.3	900 ± 26
Silicone rubber	10.2 ± 0.2	845 ± 23

* see also Puskas et al., 2009a; n = 3

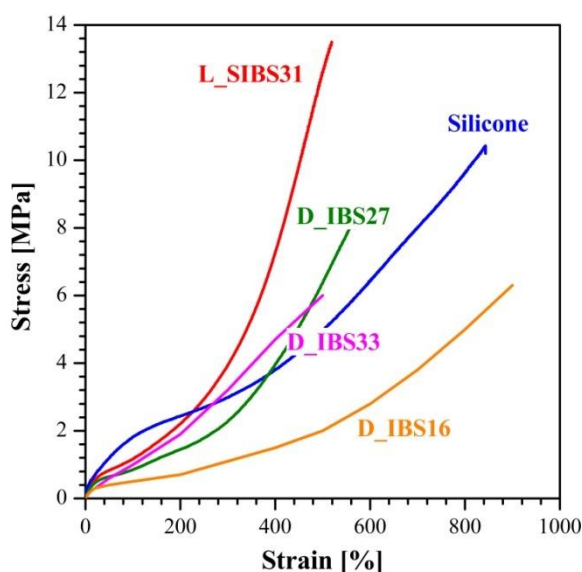


Figure 6.15: Representative tensile stress-strain plots.

L_SIBS31 had the highest ultimate tensile strength (σ_{ult}) but the lowest elongation at break (ϵ_{max}). At $M_n^{PIB(arm)}$ of 33,000 g/mol and short PS arms, D_IBS16 was the most ductile of all the materials. When compared to D_IBS16, the lower $M_n^{PIB(arm)}$ of D_IBS33 gave rise to a reduced ductility, while the same $M_n^{PS(arm)}$ provided a comparable level of tensile strength. Compared to D_IBS16, D_IBS27 had the same $M_n^{PIB(arm)}$ but twice as high $M_n^{PS(arm)}$. This resulted in higher σ_{ult} and lower ϵ_{max} in D_IBS27. From the discussions in this section and Chapter 6.2.1 on Polymer Morphology, it is clear that $M_n^{PIB(arm)}$ and $M_n^{PS(arm)}$ of D_IBS polymers are important parameters to influence their final tensile properties. They had lower tensile strength than L_SIBS31, on account of their higher Disparity index (see Table 5.3) indicating a broader molecular weight distribution which led to less ordered structures. It is important to highlight that the tensile strength of all tested materials are well above those of soft tissues [196], and thus can be good biomaterial candidates for soft tissue replacement. The PIB-based block copolymers were softer than the silicon rubber, as demonstrated by their lower moduli (see Figure 6.15).

6.2.3.2 Dynamic fatigue performance (SILT and SLT)

To compare the dynamic fatigue performance of these PIB-based block copolymers and silicone rubber, the methodology introduced in Chapter 5.4.2 was applied where SILT was first used to identify the critical stress of each material, followed by SLT to evaluate the dynamic creep of these materials. As discussed in Chapter 5.4.2, the SILT was performed at 1 % of σ_{ult} step for every 1000 cycles on each material. This SILT methodology was similar to those employed by El Fray and coworkers on 3 mm thick S2 dumbbells, except they had used different testing frequencies at various loading levels [48] and a step size of 5 % [197]. However, 5% step size in the used 1 mm thick dumbbells caused “pinching” of the hysteresis loops, changing the dynamic moduli values. “Pinching” describes the change in the shape of a hysteresis loop where one and/or both ends of the loop collapse as if they were “pinched by fingers”, and can be related to the change in material property due to cyclical loading (see Figure 6.16).

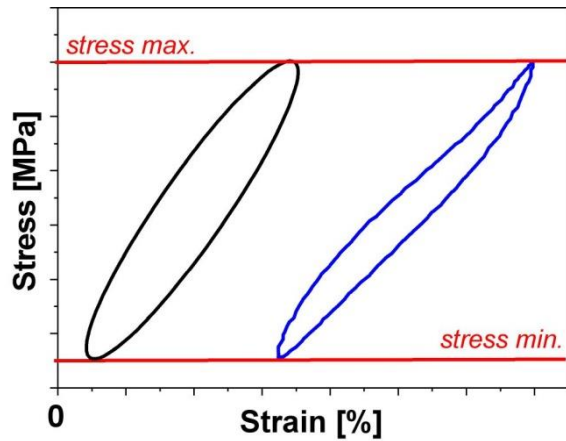


Figure 6.16: Ellipsoid shaped (left) and “pinched” (right) hysteresis loop.

Figure 6.17(a) and (b) show the evolution of E_{dyn} and mid-strain (ϵ_d) values measured for each material over more than 12,000 cycles, respectively. Table 6.7 lists the magnitude of the stress (1% of σ_{ult}) applied to the materials at each step and the critical stress (σ_c) when E_{dyn} dropped more than 5 % in a single step. No pinching of the hysteresis loops was observed prior to reaching the critical stress σ_c . Several interesting observations can be drawn from Figure 6.17 to highlight the difference in dynamic response of the polymers. Silicone rubber had the highest E_{dyn} and lowest ϵ_d among all materials throughout all SILT cycles, which can be attributed to the presence of the chemically crosslinked network and the silica particles to reinforce this thermoset elastomer.

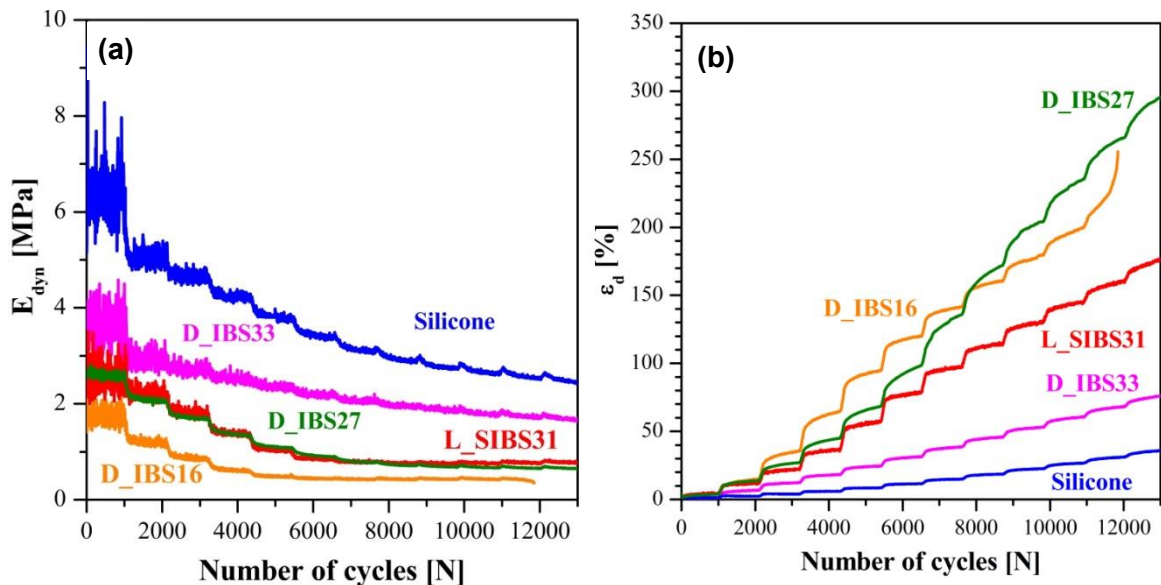


Figure 6.17: (a) E_{dyn} and (b) ϵ_d profiles of various materials from SILT ($R = 0.1$; $f = 1$ Hz; Step size = 1% of σ_{ult}).

D_IBS27 and L_SIBS31 showed comparable E_{dyn} , but D_IBS27 had higher ϵ_d than L_SIBS31. These materials have similar $M_n^{\text{PS}(\text{arm})}$ but D_IBS27 has a much higher $M_n^{\text{PIB}(\text{arm})}$ than L_SIBS31. The effect of the branched architecture can be observed in the E_{dyn} and ϵ_d plots of D_IBS33, which showed the highest overall E_{dyn} and lowest ϵ_d among the PIB-based block copolymers. Most likely the shorter PIB arms of D_IBS33 helped to reduce the overall creep

ε_d at each loading step, in spite of the short PS blocks. D_IBS16 had the lowest E_{dyn} of all and broke prematurely.

Table 6.7: Critical loading levels and critical stresses σ_c from SILT.

Material	Stress Step [MPa] (1% of σ_{ult})	Critical step	Critical stress σ_c [MPa]
L_SIBS31	0.131	5	0.655
D_IBS33	0.058	6	0.348
D_IBS27	0.088	2	0.176
D_IBS16	0.063	3	0.189
Silicone rubber	0.102	5	0.510

Using the σ_c of each material listed in Table 6.7, SLT was performed to evaluate their dynamic creep behavior. The change of ε_d values and calculated dynamic creep ($\Delta\varepsilon$) of the five materials are presented in Figure 6.18(a) and (b), respectively. Based on these SLT tests with the σ_c of each material, silicone rubber had the lowest $\Delta\varepsilon$ at 3.0 ± 0.5 % among all the materials that can be attributed to the chemical crosslinking and silica reinforcement. The $\Delta\varepsilon$ of D_IBS33 was much lower than the other polymers, again due to its shortest PIB arms and branched architecture. For this series of SLTs, Figure 6.19(a) - (c) provide the measured storage energy, loss energy and damping of these five materials. Two key observations can be made to relate these parameters to the possible damage in the material. Up till about 20,000 cycles, the stored and loss energies of the five materials experienced appreciable increases, which in general stabilized to a constant increase. This trend can also be noted in the damping profiles in Figure 6.19(c). This suggests that there may be an initial period of fatigue damage followed by a period of stabilization before a catastrophic failure at the end of SLT, similarly to the process of fatigue crack growth [198].

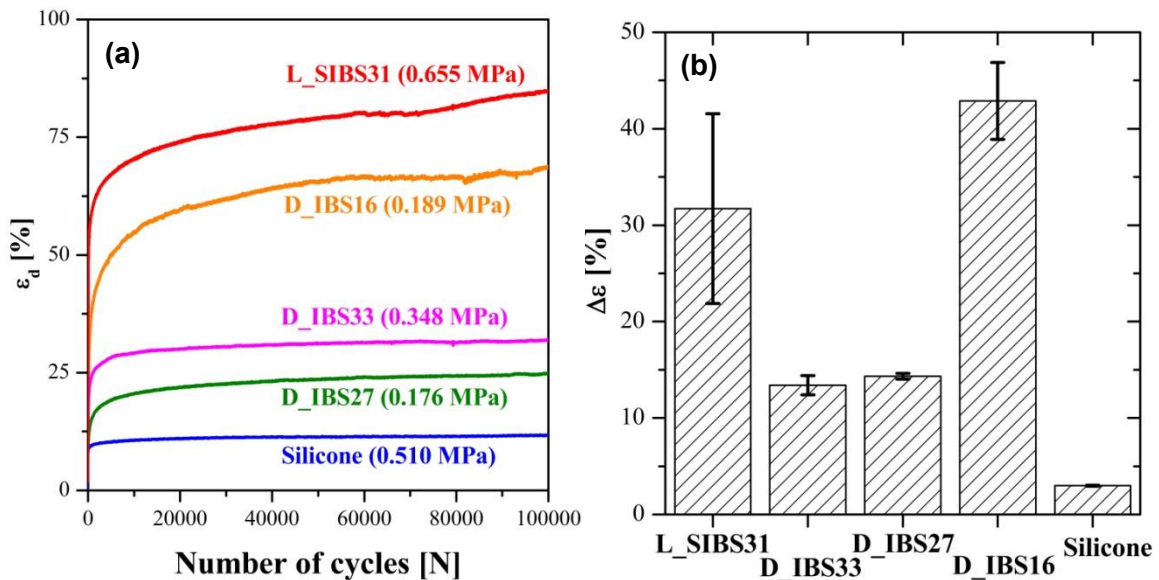


Figure 6.18: (a) ε_d profile, and (b) $\Delta\varepsilon$ values of various materials using SLT ($f = 1$ Hz, $R = 0.1$ and the σ_c of each material).

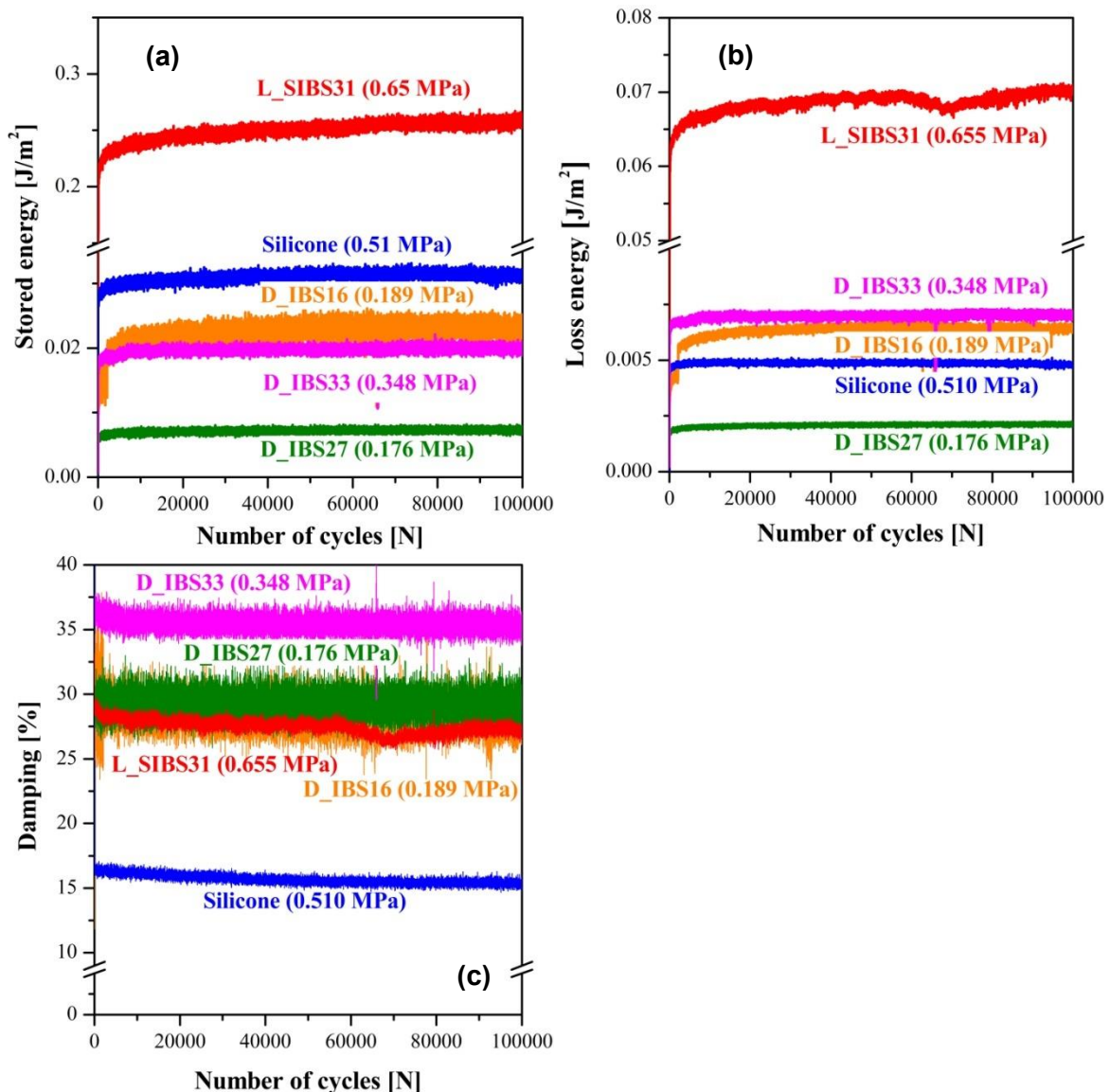


Figure 6.19: (a) Stored energy, (b) loss energy and (c) damping plots of various materials using SLT ($f = 1$ Hz, $R = 0.1$ and the individual σ_C of each material).

D_IBS33 had the highest damping which highlights its ability to dissipate energy much better than other materials, and silicone rubber had the poorest damping characteristics among the five materials.

For a consistent comparison of the dynamic creep performance, the materials were tested at 0.510 MPa, the σ_C of silicone rubber. Figure 6.20(a) and (b) present the ε_d plots during SLT and the calculated $\Delta\varepsilon$ at the end of 100,000 cycles. At the lowest hard phase content among the PIB-based block copolymers, D_IBS16 broke prematurely after 20,000 cycles before the end of the test. L_SIBS31 and D_IBS27 had very similar ε_d profiles and the $\Delta\varepsilon$ of the latter was only slightly higher than that of the former, because of the longer PIB arms and shorter PS arms in D_IBS27. D_IBS33 had much lower ε_d values throughout the test and its $\Delta\varepsilon$ was lower than those of L_SIBS31 and D_IBS27. Silicone rubber had the lowest ε_d and $\Delta\varepsilon$ of all materials, due to chemical crosslinking and silica reinforcement. Figure 6.21(a) – (c) present the stored energy, loss energy and damping of the five materials during SLT. Similarly to Figure 6.19 with the exception of D_IBS16 that broke prematurely, silicone rubber, L_SIBS31, D_IBS27 and D_IBS33 only showed minor change in the damping characteristic beyond

20,000 cycles of dynamic loading, as given by the marginal changes in the stored and loss energy as well as the damping ratio. D_IBS33 remains the best material for energy dissipation and shock absorption with the highest damping ratio among the five materials.

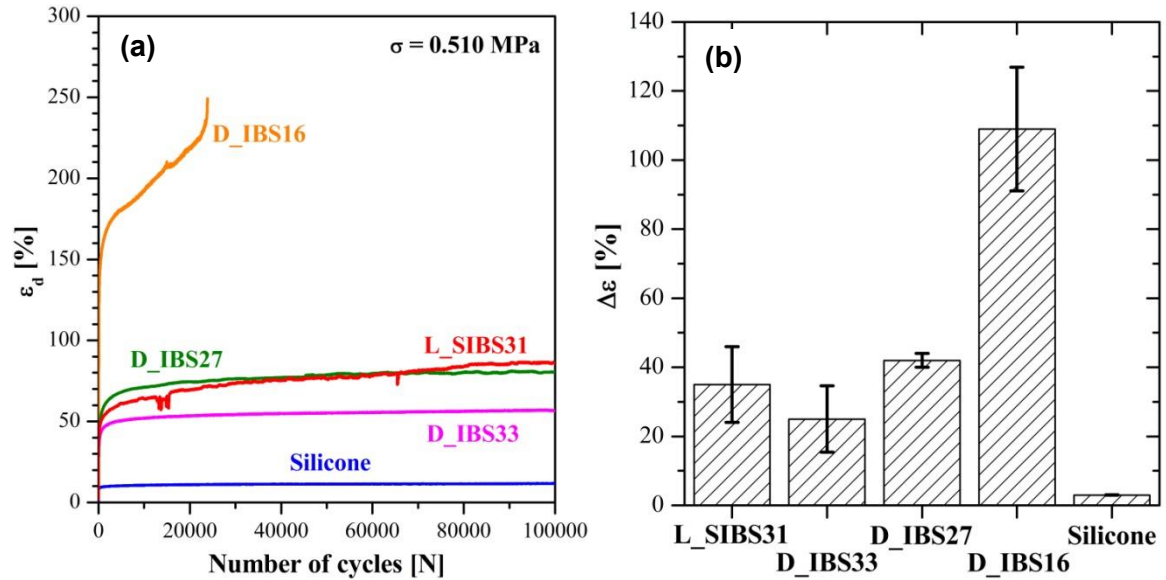


Figure 6.20: (a) ε_d , (b) $\Delta\varepsilon$ values from SLT ($f = 1$ Hz, $R = 0.1$ and $\sigma = 0.51$ MPa).

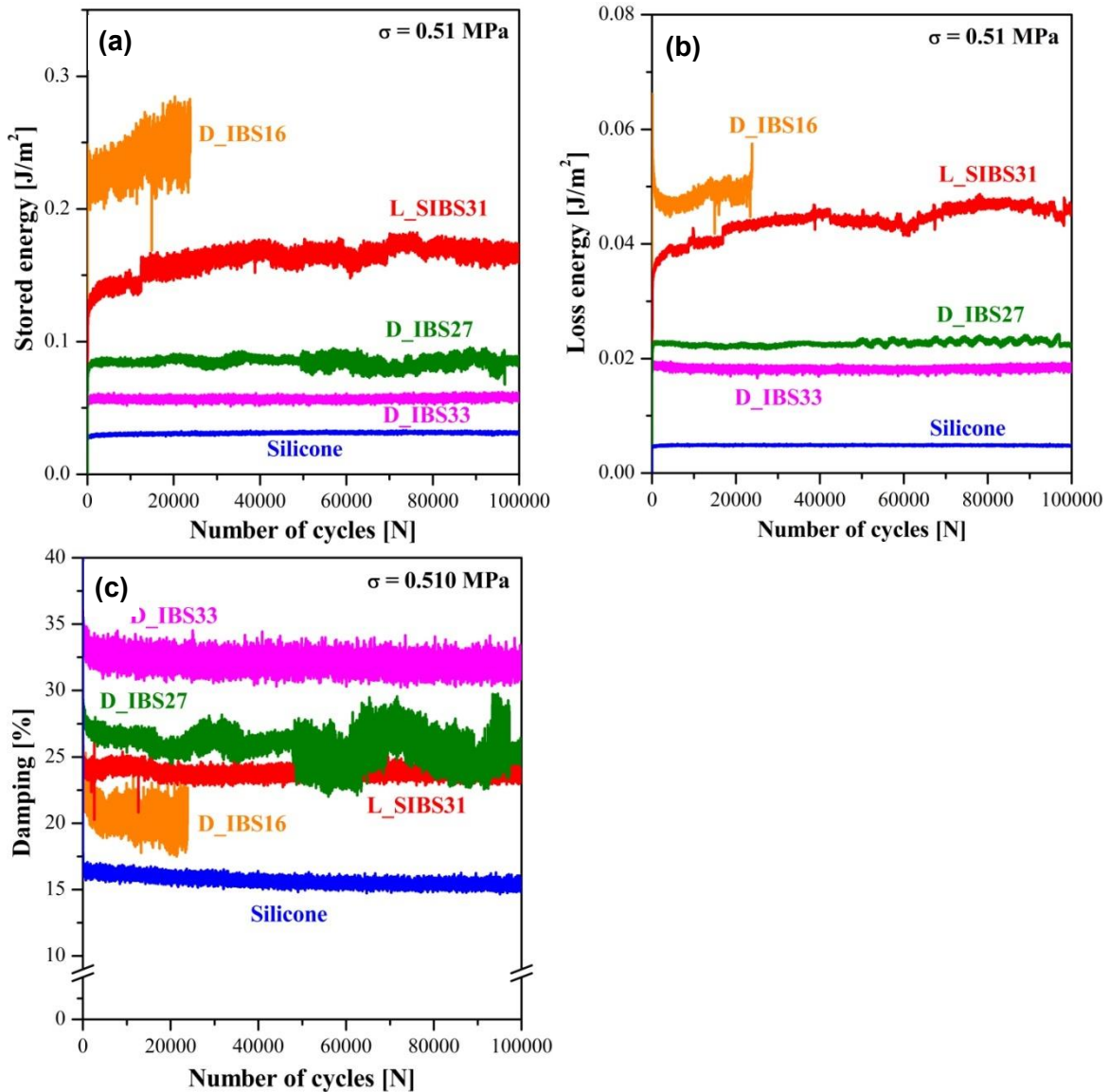


Figure 6.21: (a) Stored energy, (b) loss energy and (c) damping plots from SLT ($f = 1$ Hz, $R = 0.1$ and $\sigma = 0.51$ MPa).

6.2.4 Summary

This study investigated the morphology, thermal, quasi-static tensile and long-term dynamic fatigue properties of PIB-based block copolymers made by living carbocationic polymerization. The effects of chain architecture, hard phase (PS) content and molecular weight of the PIB and PS arms ($M_n^{\text{PIB}(\text{arm})}$ and $M_n^{\text{PS}(\text{arm})}$) were studied using L_SIBS31 with a linear triblock architecture, and D_IBS16, D_IBS27 and D_IBS33 with branched PIB cores capped with PS end-blocks and hence representing the additional crosslinking. Silicone rubber was also used in this study as a benchmark biomaterial. From TEM imaging of stained thin sectioned samples, dispersed PS domains with 3D-like structures were observed in the polymers with branched PIB cores. From the quasi-static testing, it was found that $M_n^{\text{PS}(\text{arm})}$ and $M_n^{\text{PIB}(\text{arm})}$ are two important material parameters that influence the σ_{ult} and ϵ_{max} of the PIB-based block copolymers. The T_g of the PS phases shifted to $\sim 120^\circ\text{C}$ in the branched block copolymers. $M_n^{\text{PS}(\text{arm})}$ and $M_n^{\text{PIB}(\text{arm})}$ also had a direct influence on the magnitude of E_{dyn} and ϵ_d , of the tested PIB-based materials and the beneficial effect of additional branches in the PIB core was

demonstrated by investigating the dynamic creep and fatigue properties of L_SIBS31 and D_IBS33, which are chemical similar, concerning the hard phase content (app. 30 wt.%) and the molecular weight M_n (app. 70,000 g/mol), but different in terms of their structure (linear vs. dendritic). In summary, the static and dynamic mechanical properties of SIBS-type polymers can be fine-tuned by the composition, architecture and molecular weight of the materials. Nevertheless, the biggest shortcoming is the relatively high creep of these materials, typical of all thermoplastic elastomers. The approach to improve this drawback with carbon reinforcement of the D_IBS materials will further be discussed in Chapter 6.3.

6.3 Influence of a secondary network structure on the material performance of dendritic polyisobutylene-based thermoplastic elastomers using nano-scaled additives (based on [199] and [200])

In order to study the effect of secondary network structure, two different dendritic samples were used with poly(*p*-methylstyrene) (PMS) (D_IB_MS10 and D_IB_MS17) hard blocks and modified using both, a reinforcing carbon black grade as well as a nano-clay filler. For the evaluation of the nano-clay composites [200], the the structure-property relationship has been established by providing the mechanical properties and morphological evaluation.

6.3.1 Composites – carbon black

D_IBS block copolymers with PIB dendritic core and poly(isobutylene-*b*-*para*-methylstyrene) end blocks were synthesized by Puskas et al. as reported in [121, 160]. The material designation, type of hard phase, hard phase content, number-averaged molecular weight (M_n) and disparity index of these polymers are provided in Table 6.8. D_IB_MS10_300 refers to a block copolymer with 10 wt% MS content and $M_n \sim 300$ kg/mol. The average number of end blocks or “arms” (N) in the branched samples is calculated as $B+2$ as reported, where B is the average number of branches per chain obtained from polymerization kinetics [121, 160]; N are also included in Table 6.8. The hard phase content, molecular weight and disparity index of these materials were measured using nuclear magnetic resonance (NMR) spectroscopy and size exclusion chromatography (SEC); the experimental approaches for these material characterizations were described elsewhere [160, 162]. The description of these materials is provided in Table 6.8.

Table 6.8: Material types used in the current study.

Material Designation	Total MS (wt%)	M_n (g/mol)	M_w/M_n	N^*	MS in end-block (wt%)
D_IB_MS10_300 (06DNX030)	9.5	291,600	1.94	4	21
D_IB_MS17_150 (06DNX120)	16.7	146,600	1.46	5	42

*Rounded numbers.

The carbon composites were prepared as reported using 60 phr (37.5 wt%) N234 carbon black (Cabot Corporation) [121, 160]. A medical-grade crosslinked silicone rubber reinforced by silica (MED 4050) supplied by Nusil Technology was used for comparison.

6.3.1.1 Morphology

Driven by thermodynamic forces, the thermoplastic and elastomeric phases in TPEs phase separate to develop distinctive ordered morphologies, depending on the relative composition of the two phases [195]. Figure 6.22(a) – (d) are the TEM images of thin sections of RuO₄-stained D_IB_MS10_300, D_IB_MS17_150, and their CB composites. Table 6.9 lists the calculated average molecular weight of the PMS chain in the end block [$M_n^{PMS(EB)}$], PIB core (M_n^{PIB}), and PIB branches [$M_n^{PIB(arm)} = M_n^{PIB}/N$] in D_IB_MS10_300 and D_IB_MS17_150 [121, 160]. From Figure 6.22 (a) and (b), the hard PMS domains in neat D_IB_MS10_300 and D_IB_MS17_150 generally assumed a circular shape for spheres or cylinders. Table 6.10,

Figure 6.22 (a) and (b) show that the hard phase domains in D_IB_MS17_150 were smaller and closer to one another than those in D_IB_MS10_300, which can be related to the lower $M_n^{PMS(EB)}$ in the end blocks and much longer PIB arms in D_IB_MS17_150 (see Table 6.9).

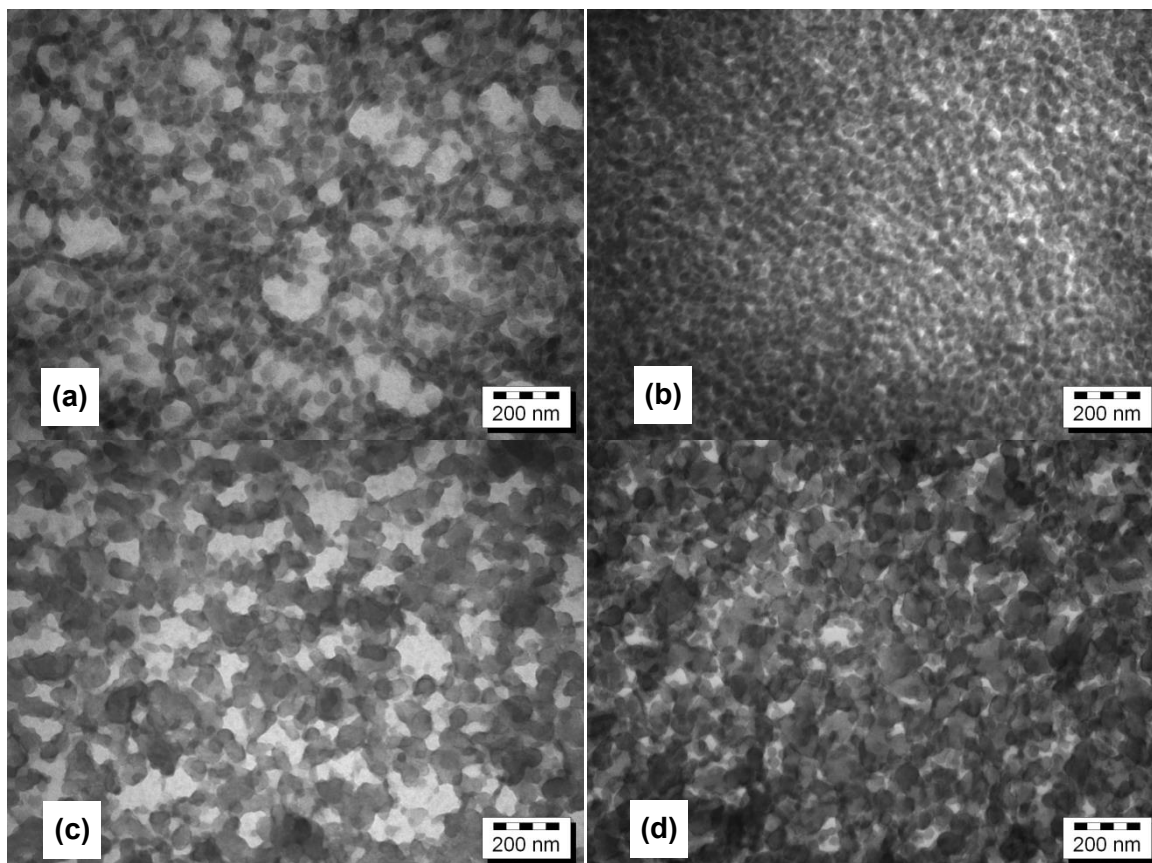


Figure 6.22: TEM images of stained thin sections of (a) D_IB_MS10_300, (b) D_IB_MS17_150, (c) D_IB_MS10_300_CB, and (d) D_IB_MS17_150_CB.

Table 6.9: Material composition.

Material	End-Block		MS in arm wt%	Soft Core	
	M_n^{EB} [g/mol]	$M_n^{EB(arm)}$ [g/mol]		M_n^{PIB} [g/mol]	$M_n^{PIB(arm)}$ [g/mol]
D_IB_MS10_300	68,000	17,000	42	224,000	56,000
D_IB_MS17_150	32,000	6,400	21	116,000	23,000

(Numbers rounded up to the nearest thousands.)

Table 6.10: Hard phase domain sizes from TEM.

Material	Domain Size [nm]
D_IB_MS10_300	39 ± 8
D_IB_MS17_150	31 ± 6
D_IB_MS10_300_CB	79 ± 32
D_IB_MS17_150_CB	67 ± 22

The TEM images in Figure 6.22(c), (d) and Table 6.10 revealed that the addition of CB led to an overall increase in the size of the discrete domains. Since samples were not stained, the darker phase can be attributed to CB. From the TEM images of unstained thin section of D_IB_MS10_300_CB and D_IB_MS17_150_CB in Figure 6.23, one can observe that the CB is well dispersed and distributed in the polymer matrix and is preferentially attracted to the hard PMS-rich phases.

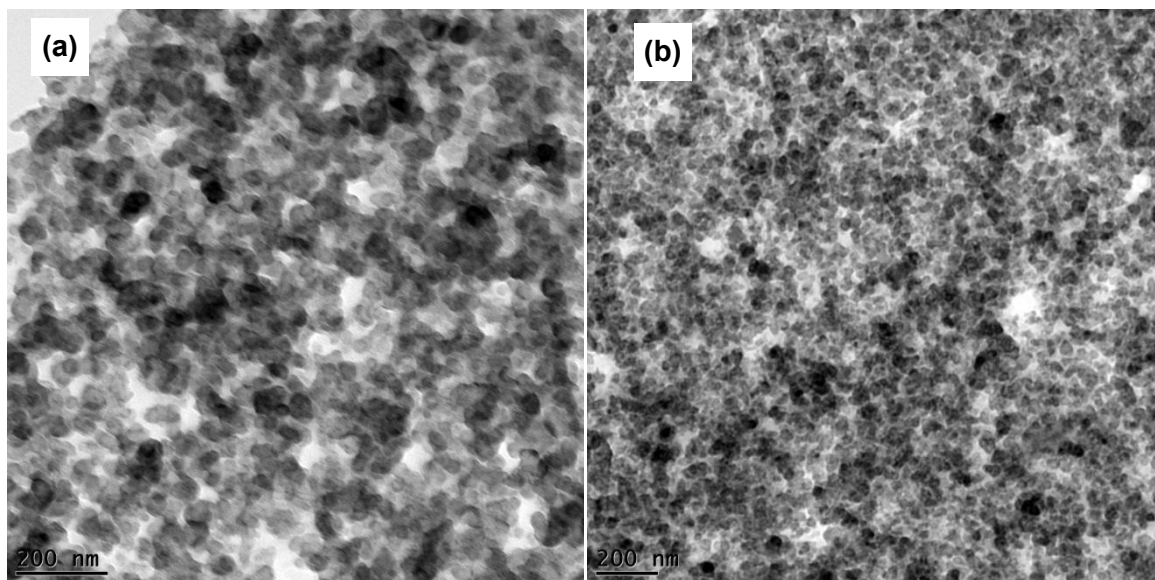


Figure 6.23: TEM images of unstained thin sections of (a) D_IB_MS10_300_CB and (b) D_IB_MS17_150_CB.

In Figure 6.23, the dispersed CB particles in D_IB_MS17_150_CB were seen to be notably smaller than those in D_IB_MS10_300_CB to indicate a better degree of filler dispersion in the polymer matrix. Based on these microscopy observations and domain measurement, the well dispersed CB filler can provide reinforcement to the polymer matrix, not only via its surface interaction with the polymer matrix, but also through its unique “nucleating” effect to link and form larger PMS domains and connect together into a secondary network.

To further support the conclusion, of the formation of a secondary network structure Figure 6.24 compares the 1-D WAXS diffraction patterns of D_IB_MS17_150 and its composite. The composite shows an additional broad peak at 25° in addition to the 15° peak in the neat amorphouse material. The broad peak can be related to the amorphouse nature of the N234 CB filler and suggests a certain level of order in the filler dispersion [160].

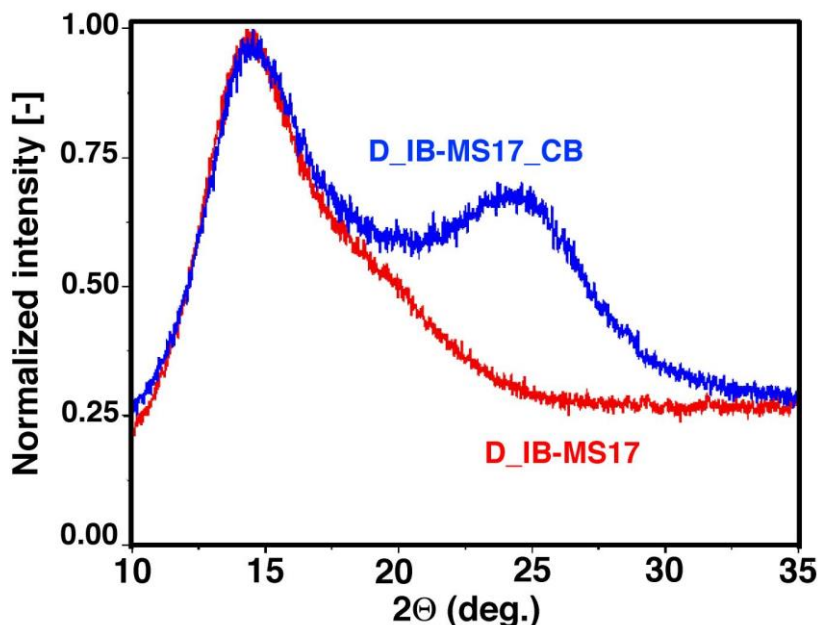


Figure 6.24: 1-D WAXS spectrum of D_IB_MS17_150 and D_IB_MS17_150_CB.

The good dispersion of CB in the D_IB-MS copolymers as well as the formation of the secondary network structure shown by the WAXS results leads to the conclusion that CB preferentially goes into the PIB and PMS-containing domains and the interfaces. This results in further phase separation and thereby leading to reinforcement as the hard phase domains are growing compared to the neat materials [121]. The dispersion of the carbon black as well as its effect on the phase separation is responsible for the drastic enhancement of the mechanical properties and will in detail be discussed in the Chapter 6.3.1.4.

6.3.1.2 Thermal properties

Figure 6.25(a) – (c) present the, E' , E'' and $\tan \delta$ of the considered materials tested over the range of the temperature sweep. Table 6.11 lists the two major thermal transition temperatures represented by the peaks in the E'' plots in Figure 6.25(b).

Table 6.11: Glass transition temperatures determined by DMTA for various materials.

Material	T_g^{PIB} (°C)	T_g^{PMS} (°C)
D_IB_MS10_300	-61.6	93.4
D_IB_MS10_300_C B	-60.7	88.4
D_IB_MS17_150	-59.8	97.8
D_IB_MS17_150_C B	-59.4	85.6

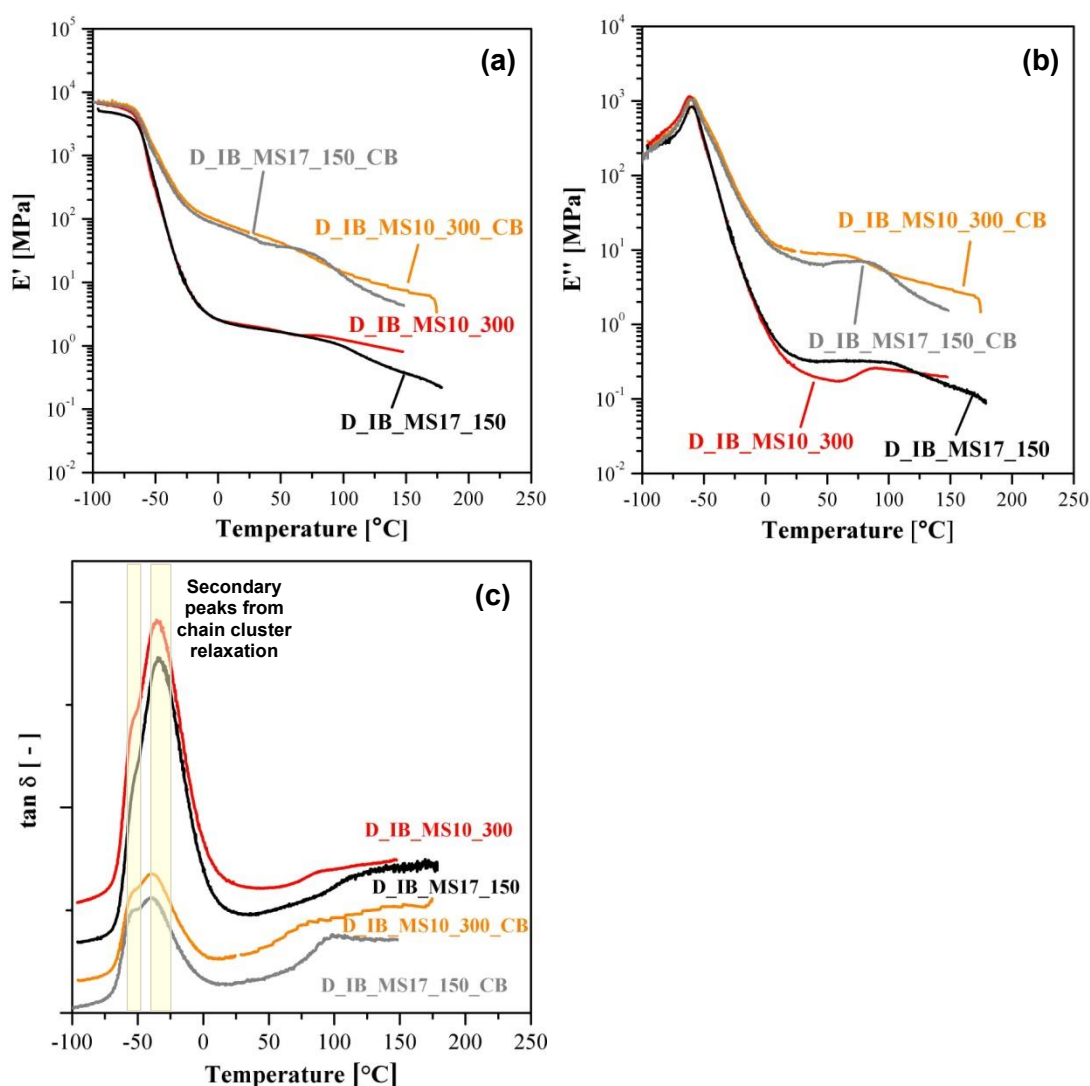


Figure 6.25: The effect of CB on the dynamic mechanical properties of D_IB-MS block copolymers: (a) storage modulus E' , (b) loss modulus E'' and (c) $\tan \delta$.

The typical phase-separated morphology of the D_IB-MS copolymers and their nanocomposites is responsible for their physical properties. From Figure 6.25, it is visible that the storage modulus (E') drops quickly around the glass transition of the soft PIB phase, followed by a wide rubbery plateau where the soft segments are in a viscoelastic state. For the neat materials and its corresponding nanocomposites this drop even begins at nearly the same temperature (see Table 6.11), which shows that the secondary network has no effect on the mechanical properties at temperatures below the glass transition of PIB. Considering the second glass transition for the styrenic phase, a drop in E' and a corresponding peak in E'' or $\tan \delta$. can be detected for D_IB-MS materials, even for those with a low content of PMS. These two-stage changes in the storage and loss moduli provide some indication on the phase-separated nature of the block copolymers. From Figure 6.25(a), depicting the storage modulus of the D_IB-MS polymers and nanocomposites it is clearly visible that the nanocomposites have a much higher modulus in the rubbery plateau than their neat counterparts. In addition, the composites do behave more stable at high temperatures. The storage modulus of the neat materials already drops, while the nanocomposites still show a stable behavior. This can be related to the strong interaction between the CB and the D_IB-MS copolymers and will further be highlighted in the next section (see Chapter 6.3.1.3). From Figure 6.25(a) one can also see

that D_IB_MS17_150_CB has a higher storage modulus in the temperature range of 60 – 126°C, which can be related to stronger interaction between the carbon black and the polymer chains. In literature it is discussed, that significant changes of the glass transition due to the addition of nanoparticles can be correlated to changes in diverse transport phenomena as well as chain relaxation behavior. Specifically, both experimental and theoretical studies have indicated a tendency for highly attractive or repulsive nanoparticle interactions to increase or decrease T_g , respectively [201; 202; 203; 204]. This phenomenon has been rationalized in terms of the influence of the nanoparticle boundary interactions on the dynamics of polymers within an interfacial “layer” near the nanoparticle surfaces. In particular, polymer chains in direct contact with the nanoparticle show a slowing down (increased T_g) or acceleration of dynamics (decreased T_g) when the polymer-nanoparticle interactions are attractive or repulsive, respectively [203; 204]. One has to bear in mind the relative size of a polymer chain compared to micrometer and nanometer-sized particle. The dramatically larger chain-particle interface area in the case of nanocomposites compared to microcomposites makes effects appearing negligible in microcomposites very prominent in nanocomposites [204].

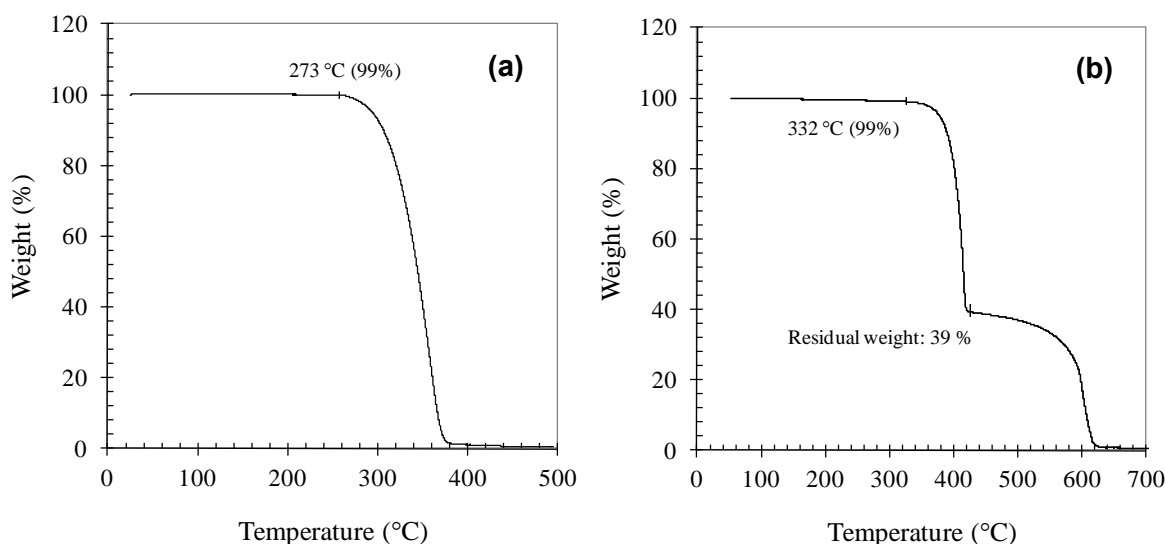
In Figure 6.25(c), two additional secondary relaxation peaks can be observed for the PIB phase, which are unique for this class of materials as firstly discussed by Götz and coworkers [188]. According to Hill and Dissado, these secondary peaks of PIB can be related to the relaxation of chain clusters with different rigidities and structural orders [194]. Interesting, as can be seen from Table 6.11, that with the introduction of CB, the T_g^{PMS} of CB composites decreased compared to the neat polymers. It can be postulated that the affinity of CB to the PMS phase in the end-blocks of the D_IB-MS polymers could have “lubricated” the PMS chains to enhance their mobility to slide over one another during the glass transition process. It is also likely that different structural orders of PMS-CB clusters existed in the CB composites. Given the dimensional disparity between polymer chains and CB particles, the DMTA would unlikely have the sensitivity to detect additional chain relaxation modes created by these PMS-CB clusters, unlike for the PIB phase as reported above and shown in Figure 6.25(c).

6.3.1.3 Thermal degradation behavior

Table 6.12 lists the temperatures at which the materials and the N234 CB fillers considered in this study underwent 1 % weight loss from thermal degradation in air and in nitrogen. From Table 6.12, there was only a marginal difference (within experimental errors) in the temperatures (~ 270°C) at which D_IB_MS10_300 and D_IB_MS17_150 lost 1 % of their weights in air. With CB fillers, the thermal stability of D_IB_MS10_300_CB and D_IB_MS17_150_CB was notably improved by more than 60°C in air. In nitrogen, the neat polymers and CB filled composites all degraded at around 318 – 334 °C. This shows that the introduction of CB filler can retard thermally induced material degradation in a similar way as in the oxygen-free (nitrogen) environment. Jakab and Omastová also reported the free radical scavenging capability of CB fillers to help suppress the chain scission of PIB at elevated temperatures [120]. Table 6.12 indicated that the environment had negligible impact on how the N234 CB fillers degraded thermally. Figure 6.26 (a) and (b) present the weight loss profiles of D_IB_MS10_300 and D_IB_MS10_300_CB when heated in air, respectively. Figure 6.26 (a) showed a typical polymer degradation behavior at elevated temperatures, whereas Figure 6.26 (b) presented a two-stage degradation process for D_IB_MS10_300_CB to show that the polymer first degraded followed by the CB fillers. At the second stage, the starting residual weight of 39 % was in good agreement to the amount (37.5 wt%) of CB fillers added. The increase in degradation temperature strongly suggests a beneficial interaction between the neat polymers and CB fillers to retard the thermal degradation process of the neat polymers, while not affecting the heat stability of the CB fillers.

Table 6.12: TGA data of the materials studied.

Material	Atmosphere	Temperature at 1% Mass Loss [°C]
D_IB_MS10_300		273 ± 1
D_IB_MS17_150*		261 ± 5
D_IB_MS10_300_CB	Air	332 ± 7
D_IB_MS17_150_CB*		329 ± 1
N234 CB		374 ± 11
D_IB_MS10_300		318 ± 7
D_IB_MS17_150		334 ± 9
D_IB_MS10_300_CB	Nitrogen	326 ± 11
D_IB_MS17_150_CB		334 ± 3
N234 CB		369 ± 17

**Figure 6.26:** Thermogravimetric plots of (a) D_IB_MS10_300 and (b) D_IB_MS10_300_CB tested in air.

6.3.1.4 Mechanical characterization

6.3.1.4.1 Tensile properties

Figure 6.27 and Table 6.13 present the quasi-static tensile properties of D_IB_MS10_300, D_IB_MS17_150, D_IB_MS10_300_CB, D_IB_MS17_150_CB, and silicone rubber (Silicone). In Chapter 6.2, it was discussed that the ultimate tensile strength (σ_{ult}) and elongation at break (ϵ_{max}) in dendritic PIB-based block copolymers are directly related to the length of arms of the soft and hard phase. In contrast, as shown in Figure 6.27 and Table 6.13, D_IB_MS10_300 and D_IB_MS17_150 show nearly identical tensile plots; such tensile behavior needs to be understood from an overall perspective of their unique IB-PMS end blocks, hard phase morphology and chain length of the soft and hard phase. From Table 6.9, both D_IB_MS10_300 and D_IB_MS17_150 had similar $M_n^{PMS(EB)}$ to give rise to a comparable σ_{ult} . While the $M_n^{PIB(arm)}$ of D_IB_MS10_300 was more than twice than that of D_IB_MS17_150, the ductility of D_IB_MS10_300 (by the measure of ϵ_{max}) stayed at the same level as

D_IB_MS17_150. The phase separation behavior discussed in Chapter 6.3.1.1 indicated that the hard domain size in D_IB_MS10_300 was relatively larger to restrict the mobility of the soft PIB chains. As a result, the soft phase (especially with higher M_n^{PIB} and $M_n^{\text{PIB}(\text{arm})}$) of D_IB_MS10_300 could undergo a greater degree of chain entanglement to limit the overall ductility of the material.

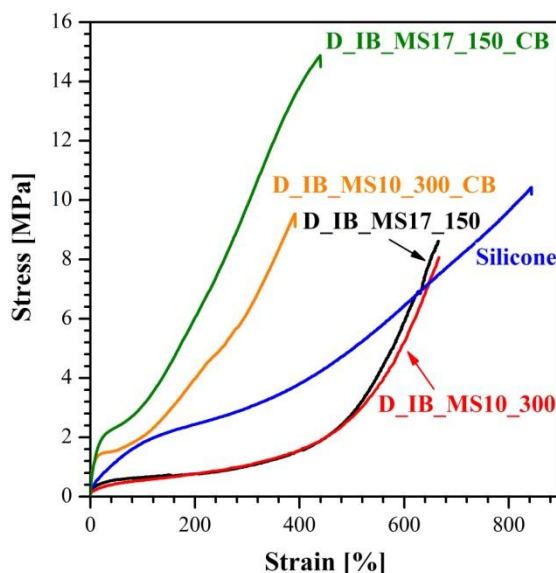


Figure 6.27: Tensile stress-strain curves of various materials (Testing rate = 500 mm/min).

Table 6.13: Quasi-static tensile properties of different materials (Testing rate of 500 mm/min).

Material	σ at 100 % [MPa]	σ at 200 % [MPa]	σ at 300 % [MPa]	σ_{ult} [MPa]	ϵ_{max} [%]
D_IB_MS10_300	0.5 ± 0.1	0.7 ± 0.1	1.1 ± 0.2	8.2 ± 0.4	647 ± 21
D_IB_MS17_150	0.6 ± 0.0	0.7 ± 0.0	1.0 ± 0.1	8.5 ± 0.7	655 ± 25
D_IB_MS10_300_CB	2.4 ± 0.4	4.6 ± 0.6	7.5 ± 1.1	10.1 ± 1.4	370 ± 31
D_IB_MS17_150_CB	2.7 ± 0.6	6.0 ± 0.0	10.5 ± 1.0	14.7 ± 1.3	455 ± 63
Silicone	1.8 ± 0.1	2.4 ± 0.0	3.0 ± 0.1	10.2 ± 0.2	845 ± 36

From Table 6.13, the reinforcing effect of CB fillers in D_IB_MS10_300_CB and D_IB_MS17_150_CB was evident with marked increases in stresses at various elongations and σ_{ult} . For the better dispersion of CB nanoparticles shown in Figure 6.23, D_IB_MS17_150_CB exhibited a greater improvement in σ_{ult} than D_IB_MS10_300_CB. With the CB fillers, D_IB_MS10_300_CB and D_IB_MS17_150_CB had comparable or higher tensile performance as the medical-grade Silicone, which was itself a crosslinked thermoset rubber with silica reinforcement. The measured σ_{ult} and ϵ_{max} of the current matrix of materials in Table 6.13 far exceed the reported strength of soft tissues [196], and satisfied the FDA requirement of 350 % on the ductility of breast implant materials [206]. Thus for such a mechanical performance, these dendritic PIB-based block copolymers and their CB composites are suitable to be used as novel biomaterials for certain implant applications. Fracture surfaces of D_IB_MS10_300 and D_IB_MS17_150 after tensile testing are shown in the SEM images of Figure 6.28 (a) and (b). It is important to note that the samples were stored at least 24 hours at room temperature before surface characterization. At microscopic scale,

the ductility of the PIB phase in these polymers can nevertheless be at work to enable material stretching and drawing and create unique fracture surface morphology upon rupture. Comparing Figure 6.28 (a) to (b), the higher $M_n^{\text{PIB}(\text{arm})}$ led to more pronounced features in the fracture surfaces of D_IB_MS10_300 as an indication of lesser material stretching and deformation. With the CB filler forming a secondary network structure, the fracture surfaces of D_IB_MS10_300_CB and D_IB_MS17_150_CB as seen in Figure 6.28(c) and (d) were much smoother and contained sharper edges to suggest a change in material failure mechanism to a rather brittle mode from the ductile fracture in the neat polymers. It is well established from the literature that the use of fillers, such as CB, carbon fibers or nanoclay, in polymer composites can lead to an embrittlement of materials [207]. This material embrittlement was also shown by the reduction of ϵ_{max} in D_IB_MS10_300_CB and D_IB_MS17_150_CB compared to the neat polymers (see Table 6.13), which was also in agreement with the findings reported by Leyva and coworkers on CB-filled SBS composites with increased σ_{ult} but reduced ϵ_{max} [208]. In detail, Leyva and her coworker noticed an increase of the tensile strength (from approximately 19 MPa to 23 MPa) up to a CB concentration of 2.6 vol%. Further increase of the CB content lead to reduction of the ultimate tensile strength. In addition, Leyva and her coworker reported that the elongation at break slowly decreases with the increase in the CB concentration (from approximately 5500 % to 1600 %). The decrease in the elongation at break with the increase in the filler loading is mainly related to the reduction in chain flexibility through the filler addition [208].

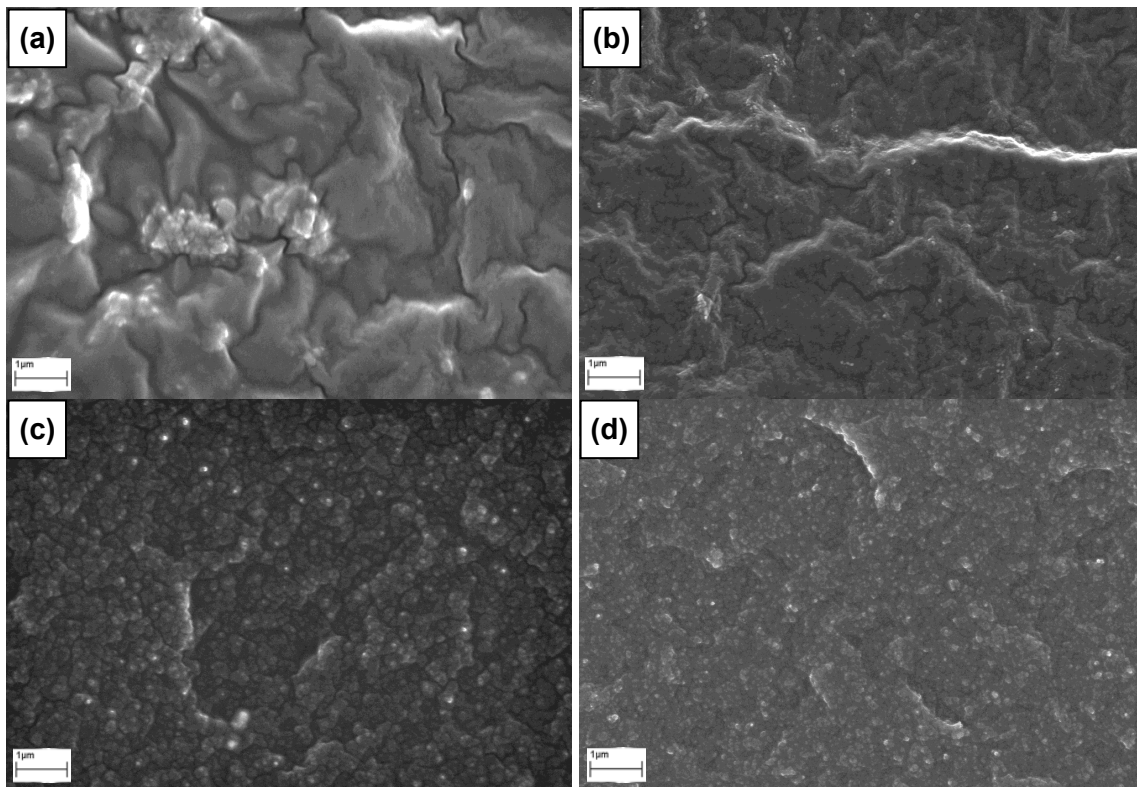


Figure 6.28: SEM images of the fracture surface of (a) D_IB_MS10_300, (b) D_IB_MS17_150, (c) D_IB_MS10_300_CB, and (d) D_IB_MS17_150_CB, after tensile testing.

6.3.1.4.2 Dynamic fatigue performance (SILT and SLT)

For SILT on a material, a starting load of 1 % of σ_{ult} was applied and kept constant for 1000 cycles. The load was thereafter raised step-wisely by another 1 % of σ_{ult} for every 1000 cycles,

with 100 transitional cycles taken between steps for the load adjustment. The testing frequency of 1 Hz was specially selected to mimic the physiological frequency experienced in the human body. Compared to the larger step size of 5 % of σ_{ult} taken by El Fray and coworkers [104], a smaller step size of 1 % was necessary for this study to reduce the “pinching” effect on the hysteresis loops of the softer materials at high strains, as reported by Puskas et al. [162]. Figure 6.29(a) and (b) show the measured mid-strain (ϵ_d) and dynamic modulus (E_{dyn}) of our considered materials from the SILT. In a consistent trend with the quasi-static tensile data (see Figure 6.27 and Table 6.13), the SILT showed that both neat polymers (D_IB_MS10_300 and D_IB_MS17_150) had similar behaviors in ϵ_d and E_{dyn} that are to be expected for their comparable tensile properties. Nevertheless, the neat polymers showed higher ϵ_d and lower E_{dyn} than Silicone, even at lower applied loads for every step. With the introduction of CB fillers, D_IB_MS10_300_CB and D_IB_MS17_150_CB had comparable ϵ_d and higher E_{dyn} than Silicone. Table 6.14 lists the critical loading level and calculated critical stress (σ_c) of each material. The lower σ_c of the neat polymers indicated a greater susceptibility to suffer material damage, lose load-carrying capability and creep more under cyclical loadings than Silicone and the CB-filled composites.

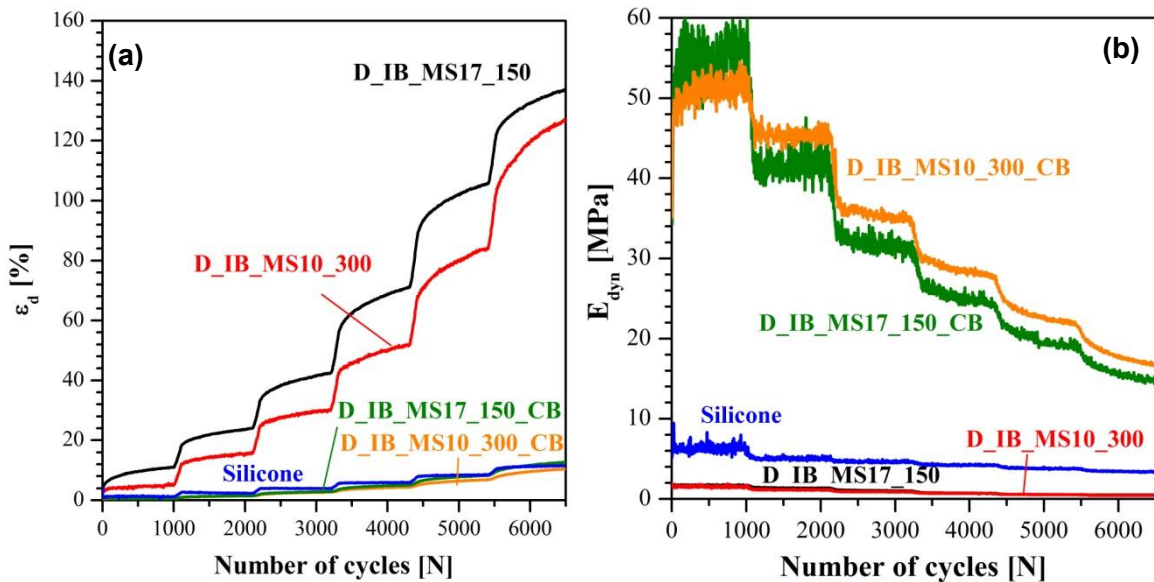


Figure 6.29: Variation of (a) mid-strain and (b) dynamic modulus over the number of cycles using SILT.

Table 6.14: Critical loading level and σ_c for various materials using SILT.

Material	Critical loading level	Critical stress σ_c [MPa]
D_IB_MS10_300	2	0.16
D_IB_MS17_150	2	0.17
D_IB_MS10_300_CB	4	0.41
D_IB_MS17_150_CB	4	0.59
Silicone	5	0.51

Dynamic Fatigue Study: Single Load Test (SLT)

To have an equitable comparison on the dynamic creep performance of different materials, the σ_c of Silicone (0.51 MPa) was employed to conduct the SLT. From this, the dynamic creep behavior of each material is shown in Figure 6.30(a) and (b) for the change of ε_d and the calculated dynamic creep ($\Delta\varepsilon$), respectively. One can observe in both figures that D_IB_MS17_150 underwent much higher ε_d and $\Delta\varepsilon$ than D_IB_MS10_300 in SLT, which can be related to its smaller molecular chain configurations [i.e. $M_n^{\text{PMS}(\text{arm})}$, M_n^{PIB} , and $M_n^{\text{PIB}(\text{arm})}$]. A higher $M_n^{\text{PMS}(\text{arm})}$ in the thermoplastic end-block would provide a greater resistance to creep deformation. As discussed in previous chapters, the higher M_n^{PIB} and $M_n^{\text{PIB}(\text{arm})}$ in D_IB_MS10_300 could also contribute to the lower creep with a greater chain entanglement within the soft phase. These structure-property relationships can provide valuable insights on how the cationic polymerization process of this class of thermoplastic elastomers can be controlled on the chain architecture and hard/soft phase content to deliver desired mechanical performance.

From the Figure 6.30, D_IB_MS10_300_CB and D_IB_MS17_150_CB had about 5 – 7 times lower $\Delta\varepsilon$ than their neat polymer counterparts. Both CB-reinforced polymers had comparable or lower ε_d than Silicone. As discussed in Chapter 6.3.1.1 and 6.3.1.4.1, the better dispersion of CB particles in D_IB_MS17_150_CB enabled a greater reinforcement of the material (shown by its higher σ_{ult}) and hence yielded a lower $\Delta\varepsilon$ than D_IB_MS10_300_CB. Also the $\Delta\varepsilon$ of D_IB_MS17_150_CB was the same as Silicone at 3 % to further demonstrate the effectiveness of CB fillers on material reinforcement.

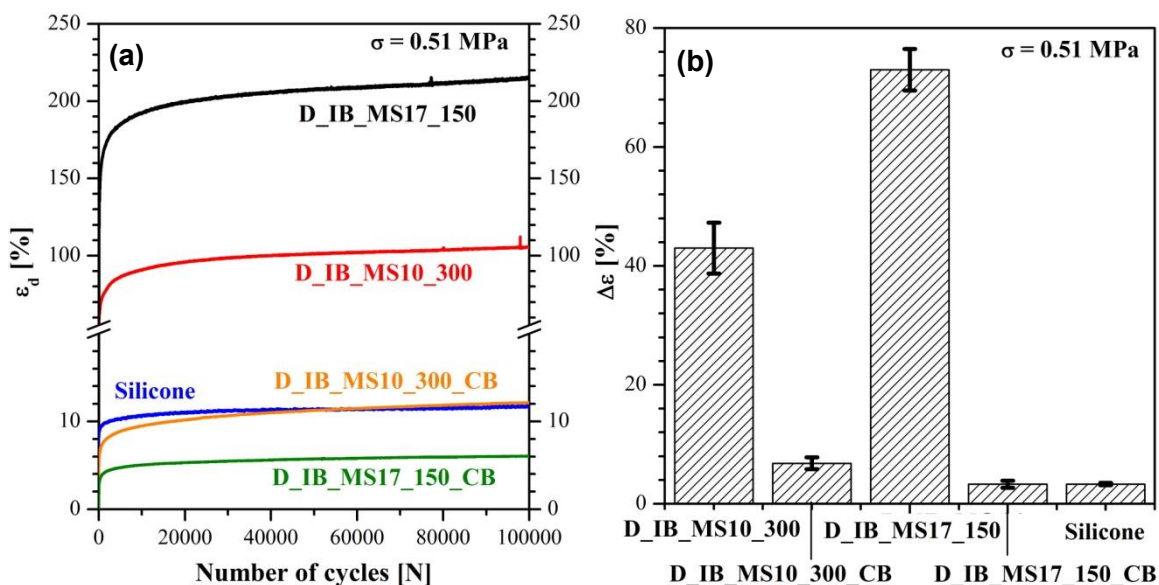


Figure 6.30: (a) ε_d , (b) $\Delta\varepsilon$ values of various materials using SLT ($f = 1$ Hz, $R = 0.1$ and $\sigma = 0.51$ MPa).

Figure 6.31(a) – (c) present the stored energy, loss energy and damping ratio of the five materials considered for SLT. In particular, Figure 6.31 (b) showed higher loss energies by both neat polymers to possibly indicate more material damage to the materials during SLT. The loss energies of CB-filled composite materials were at the similar level but still higher than Silicone that was itself chemically crosslinked and also reinforced with silica. Among the five materials, D_IB_MS10_300_CB and D_IB_MS17_150_CB had higher damping ratios as shown in Figure 6.31(c) to demonstrate their superior damping capability for relevant engineering applications. Figure 6.32(a) and (b) give the hysteresis loops of the considered

materials during the early (Cycle 1000) and ending (Cycle 99,960) stages of SLT, respectively. Comparing both figures, the hysteresis loop of each material can be seen to shift horizontally to mark the onset of dynamic creep. For the applied load of 0.51 MPa, “pinched” hysteresis loops can be observed for the softer neat polymers and Silicone from the early stage of SLT. For D_IB_MS10_300_CB and D_IB_MS17_150_CB whose quasi-static and dynamic moduli were highest among all, their hysteresis loop maintained a regular shape throughout the SLT without signs of pinching.

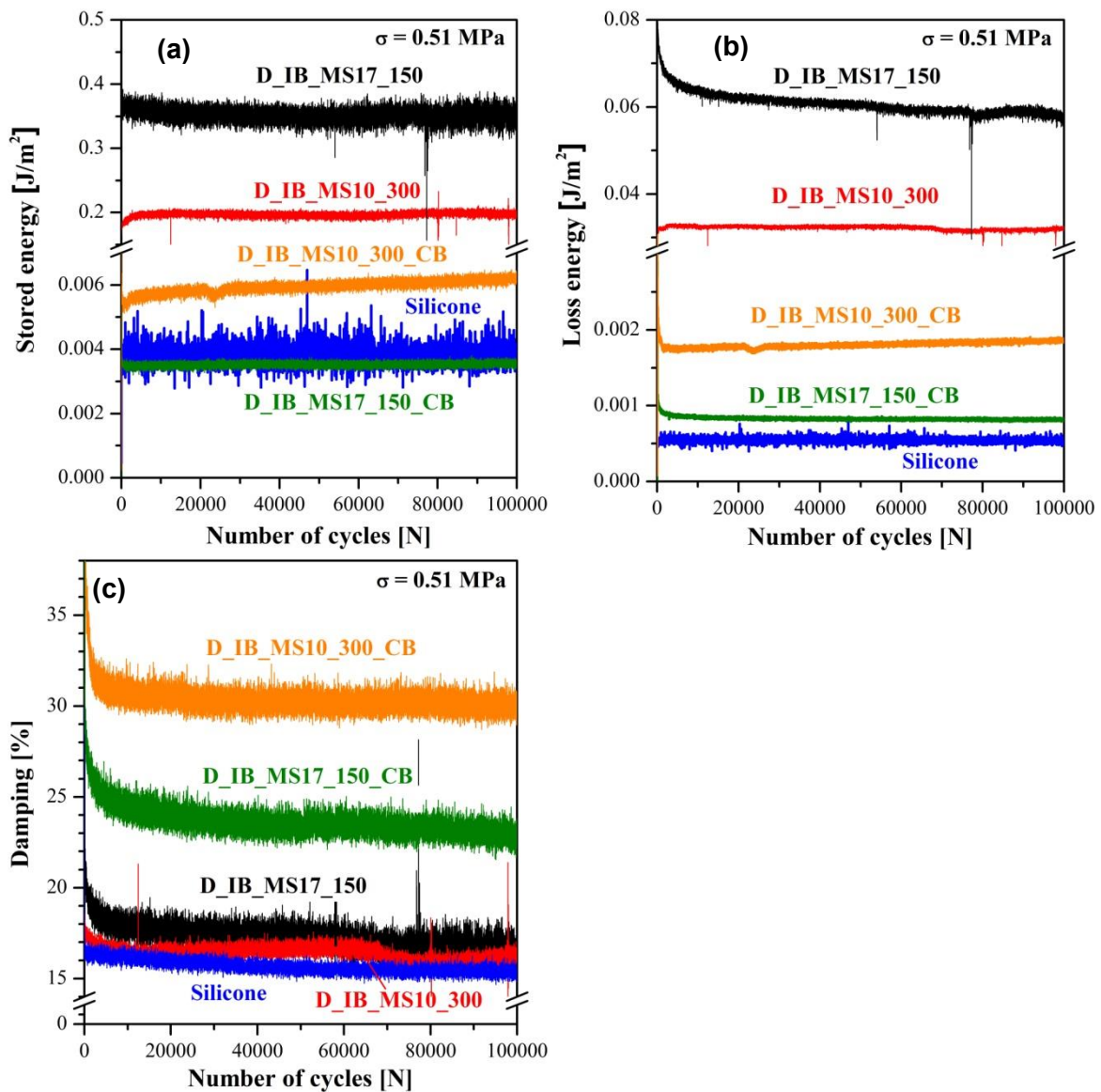


Figure 6.31: (a) Stored energy, (b) loss energy and (c) damping plots of various materials using SLT ($f = 1$ Hz, $R = 0.1$ and $\sigma = 0.51$ MPa).

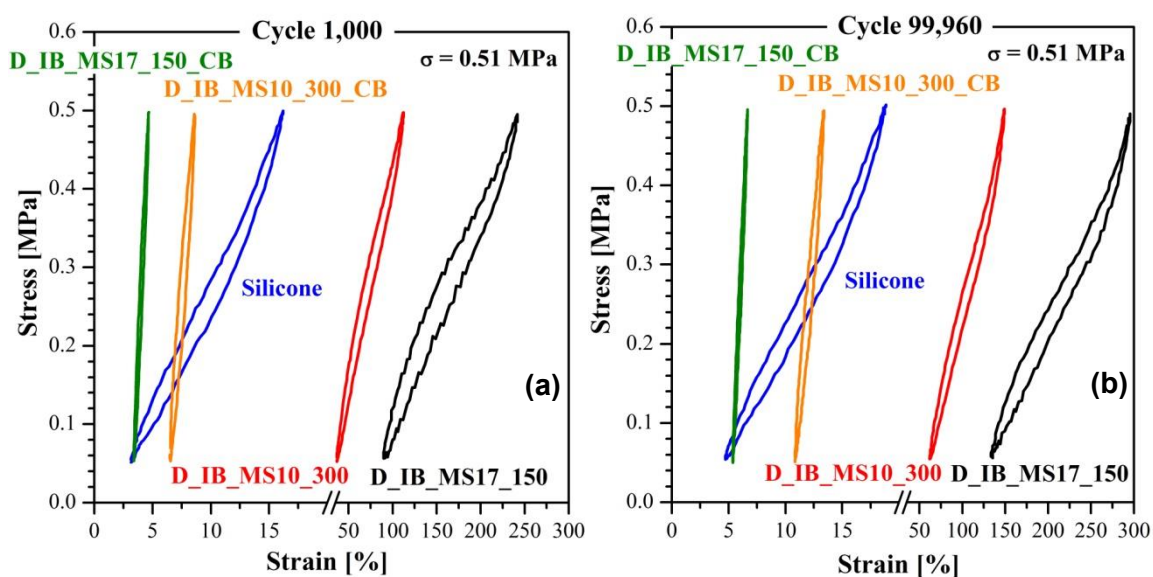


Figure 6.32: Hysteresis loops of various materials at the (a) early and (b) ending stages of SLT at $f = 1$ Hz, $R = 0.1$ and $\sigma = 0.5$ MPa.

6.3.1.5 Summary

This part of the work investigated the morphology, quasi-static and dynamic mechanical properties as well as thermal properties of a new class of styrenic thermoplastic elastomers. The neat polymers (D_IB_MS10_300 and D_IB_MS17_150) and its carbon black (CB) reinforced nanocomposite (D_IB_MS10_300_CB and D_IB_MS17_150_CB) were considered with a focus to examine the influence of CB on the material properties. As these materials are intended to be biomaterials, it is of great interest to understand their structure-property relationships and long-term dynamic creep response. Characterization approaches such as TEM, DMTA, DSC, TGA, tensile testing and hysteresis measurements (SILT/SLT) were employed to determine the morphological, thermal, quasi-static and dynamic behavior of these materials. From these evaluations, the properties of the materials were compared to a medical-grade silica-reinforced silicone rubber as a benchmark material for biomedical devices.

Morphological studies revealed that the size of discrete hard phases of the neat SIBS increased with the addition of 37.5 wt% of CB filler. Furthermore, the CB was well dispersed mainly in the hard phase, which appeared to form a secondary network that helped to reinforce this block copolymer and can be considered as real nanocomposite. Indeed, together with the good filler-matrix interaction, the use of CB filler led to an improvement in quasi-static tensile properties of both nanocomposite materials. This reinforcing effect is the result of enhanced polymer-filler interactions due to the inherent structure of the arbPIB-based TPEs. These strong polymer-filler interactions could also be seen in the thermal properties of the nanocomposites by the more pronounced high transition (hard phase) in the D_IB_MS10_300_CB and D_IB_MS17_150_CB. The reinforcing effects seen during DMTA measurements and static tensile tests could also be transferred to the dynamic fatigue performance of the nanocomposites. Already when the composites were investigated using SILT the mid-strain value of the composites were significantly reduced to be comparable to that of chemically crosslinked and silica-reinforced silicone rubber. Furthermore, the reinforcement effect of the CB filler was found to be even more pronounced during the dynamic fatigue investigation, by leading to a dynamic creep which was comparable to the chemically crosslinked reinforced benchmark silicone rubber.

In all, this study represents the first successful investigation to show that high CB contents can be used to reinforce dendritic IBS polymers resulting in an enhancement of the short-term and long-term mechanical material properties and provide an alternative material for medical grade silicon.

6.3.2 Composites – nanoclay

As a second approach to improve the mechanical performance of IBS materials, nanoclay was used. The major part of the work was to establish structure-property-relationships dependent on the polymer structure and filler content. Table 6.15 shows the detailed information about the various SIBS-clay systems used during this study.

Table 6.15: SIBS composite systems.

Polymer Matrix	Filler Types	Processing Approach	Filler Content (wt%)	Material Designation
D_IB-MS10	Clay (Cloisite [®] -20A)	Solution blending	0	D_IB-MS10
			10	D_IB-MS10_C10
			20	D_IB-MS10_C20
			30	D_IB-MS10_C30
L_SIBS34	Clay (Cloisite [®] -20A)	Solution blending	0	L_SIBS34
			10	L_SIBS34_C10
			20	L_SIBS34_C20
			30	L_SIBS34_C30

6.3.2.1 Morphology

Figure 6.33(a) and (b) present the TEM images of microtomed specimens of D_IB-MS10_C30 and L_SIBS34_C30, respectively. A good distribution of clay platelets can be observed in Figure 6.33(a) which suggests a good polymer-filler interaction in D_IB-MS10_C30. In contrast, Figure 6.33(b) shows clay agglomeration at various regions in the L_SIBS 34 matrix. This may be due to the low MW of L_SIBS34. With well exfoliated clay platelets evenly distributed, the clay fillers can form a secondary network to tie IBS polymer chains together. However, when the degree of dispersion becomes poor, the clays start to agglomerate like “a stack of cards”.

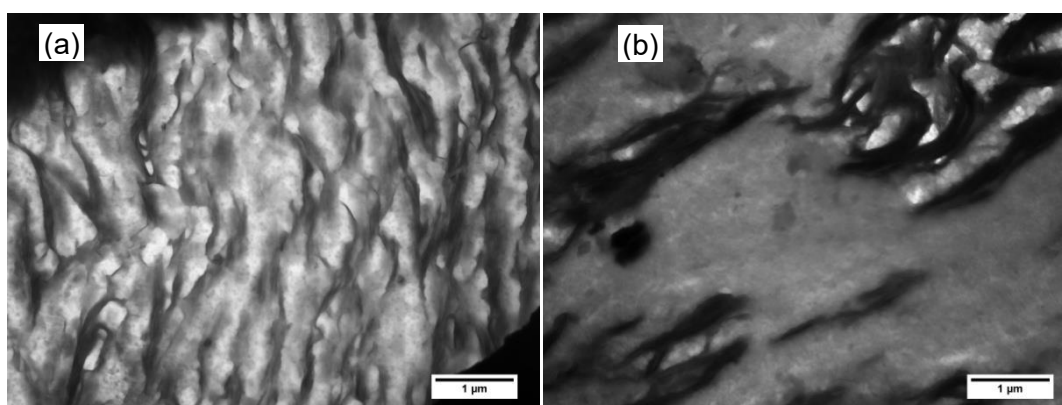


Figure 6.33: TEM micrographs of clay dispersion in D_IB-MS10_C30 (a) and L_SIBS34_C30 (b).

While the clay agglomerates can still stiffen the polymer, they nevertheless become “hot-spots” of stress concentration and can delaminate prematurely to lead to an overall material rupture, as illustrated and discussed in Chapter 6.3.2.3. Due to the secondary network, the composites

for both L_SIBS34 and D_IB-MS10 become more rigid against deformation to explain the lower ultimate tensile strain at failure.

6.3.2.2 Thermal properties

Table 6.16 summarizes the obtained DSC data. The two characteristics glass transitions (-65 °C and 100 °C corresponding to the PIB and hard phases (MS), respectively [192]) in L_SIBS34 remained unaffected by the introduction of Cloisite®-20A fillers. The high T_g transitions could not be observed in D_IB-MS10 and its clay composites, due to the low hard phase content.

Table 6.16: Thermal properties of SIBS and SIBS-clay composites.

Materials	Glass Transition Temperature	
	T_g^{PIB} (°C)	T_g^{PS} (°C)
L_SIBS34	-65.0	100.6
L_SIBS34_C10	-66.3	102.4
L_SIBS34_C20	-67.0	103.0
L_SIBS34_C30	-67.5	100.2
D_IB-MS10	-63.1	-
D_IB-MS10_C10	-63.4	-
D_IB-MS10_C20	-64.7	-
D_IB-MS10_C30	-64.3	-

Heating-cooling range: -150 – 250 °C; heating rate: 10 °C/min.

6.3.2.3 Mechanical characterization / tensile properties

The primary goal of adding clay fillers to IBS polymer is to enhance the mechanical properties of the material for a better performance and a wider scope of biomedical applications. Figure 6.34(a) and (b) provide the stress-strain plots and the comparison of the measured stress at certain strains (100 %, 200 % and 300 %) of filled and unfilled D_IB-MS10.

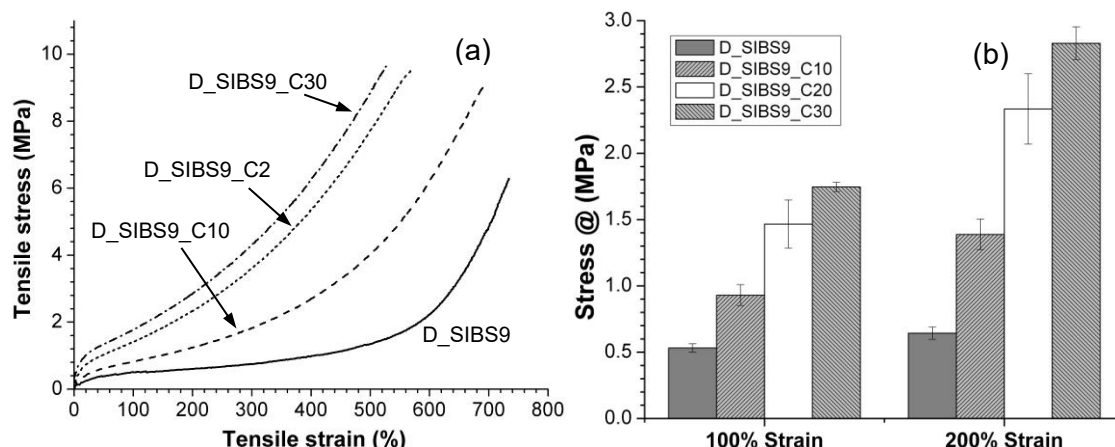


Figure 6.34: Stress-strain response (a) and stress at 100 % and 200 % strain (b) of D_IB-MS10 and its composites.

One can observe from Figure 6.34(a) that the neat D_SIBS exhibits an early elastic response from the start of the test to around 40 % strain, before an extended rubbery plateau. At about 600% elongation, the stress sharply increases until the sample breaks. This additional reinforcement of D_SIBS can be attributed to the phenomenon of strain-induced crystallization that is known to occur in stretched PIB, butyl rubber and L_SIBS [209].

It is interesting to see from Figure 6.34(a) that the rubbery plateau of the neat D_IB-MS10 (between 100 and 200 % strain) gradually disappears with increasing amount of clays. This suggests that the distribution of clay fillers has been effective to “hold” the entanglement points in place and reduce the mobility of polymer chains. In particular, Figure 6.34(b) and Table 6.17 show that the initial modulus at 100 % and 200 % strain of the D_IB-MS10 increased nearly four-fold at 30 wt% clay content. While Cloisite®-20A did reduce the ultimate elongation of D_IB-MS10, its ability to strengthen the polymer is shown evidently in Figure 6.34(a) and Figure 6.35, which plots the change of ultimate tensile stress and strain of D_IB-MS10 at various clay content. It needs to be mentioned that during the preparation of D_IB-MS10 clay composites, small amounts of polymer-clay agglomerates were observed at 30 wt% clay content. As a result, the ultimate tensile stress of D_IB-MS10 appears to be maximized at 20 wt% of Cloisite®-20A clays, with an overall increase of 50 %. The material remained translucent even at 30 wt% clay content.

Table 6.17: Quasi-static tensile properties of neat and filled D_IB-MS10 materials using micro-dumbbells at a testing rate of 500 mm/min.

Material	σ at 100 % [MPa]	σ at 200 % [MPa]	σ_{ult} [MPa]	ϵ_{max} [%]
D_IB-MS10	0.5 ± 0.0	0.6 ± 0.0	6.6 ± 0.6	737 ± 40
D_IB-MS10_C10	0.9 ± 0.1	1.4 ± 0.1	9.6 ± 1.9	648 ± 37
D_IB-MS10_C20	1.5 ± 0.2	2.3 ± 0.3	9.9 ± 1.1	594 ± 22
D_IB-MS10_C30	1.7 ± 0.0	2.8 ± 0.1	9.5 ± 1.4	534 ± 51

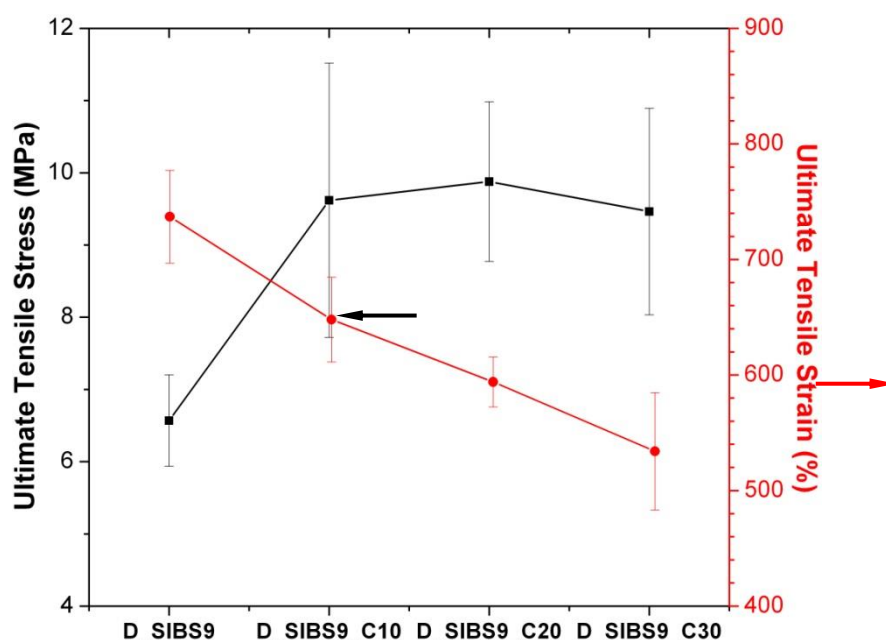


Figure 6.35: Ultimate tensile stress and strain of D_IB-MS10 and its composites.

Figure 6.36(a) and (b) show the tensile plots and the initial moduli of filled and unfilled L_SIBS34, respectively. Similarly to D_IB-MS10, L_SIBS34 has an initial elastic behavior and undergoes strain-induced crystallization, but at relatively lower extension. The moduli at 100 % and 200 % strain greatly increased, tripling at 30 wt% clay content. However, both the ultimate tensile stress and strain of L_SIBS34 decreased as more clay was introduced, as can be seen in Figure 6.36 and Table 6.18. Figure 6.37 presents the respective decrease in the ultimate tensile stress and strain of L_SIBS34 with various loadings of Cloisite®-20A clays. Hence, one can conclude that while Cloisite®-20A enhanced the tensile moduli of L_SIBS34, it weakened and embrittled the material.

Table 6.18: Quasi-static tensile properties of neat and filled L_SIBS34 materials using micro-dumbbells at a testing rate of 500 mm/min.

Material	σ at 100 % [MPa]	σ at 200 % [MPa]	σ_{ult} [MPa]	ϵ_{max} [%]
L_SIBS34	0.9 ± 0.0	1.4 ± 0.1	12.7 ± 0.7	548 ± 19
L_SIBS34_C10	2.1 ± 0.2	3.6 ± 0.3	9.2 ± 0.8	418 ± 18
L_SIBS34_C20	2.4 ± 0.1	3.9 ± 0.2	7.3 ± 1.3	359 ± 32
L_SIBS34_C30	2.9 ± 0.3	4.7 ± 0.5	6.5 ± 0.6	298 ± 17

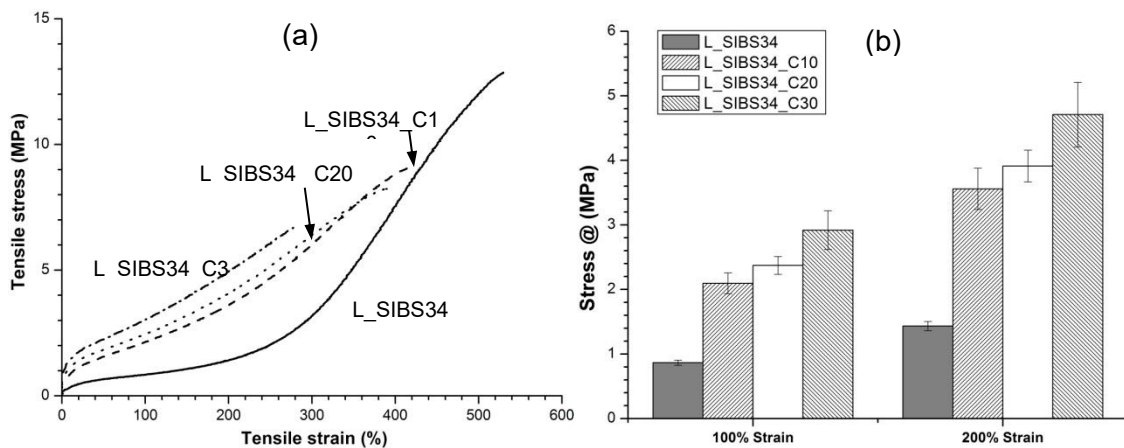


Figure 6.36: Stress-strain response (a) and stress at 100 % and 200 % strain (b) of L_SIBS34 and its composites.

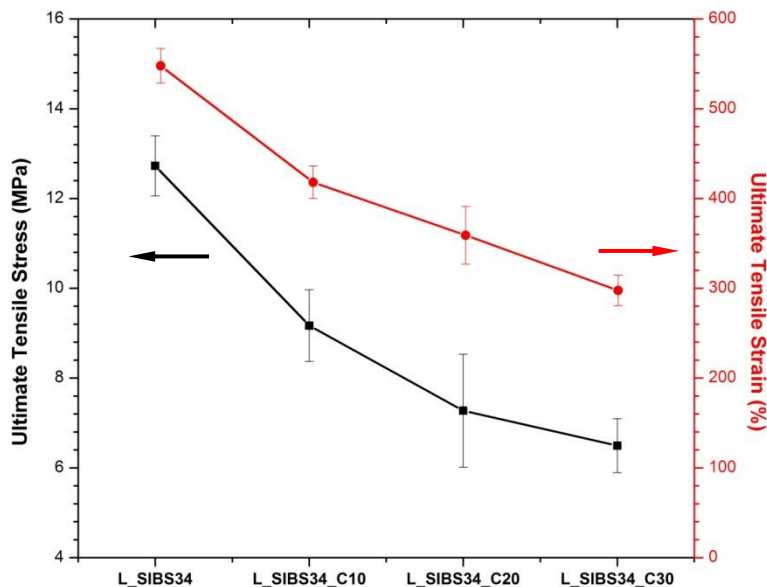


Figure 6.37: Ultimate tensile stress and strain of L_SIBS34 and its composites.

There is a contrast in the reinforcing capability by Cloisite®-20A for different IBS polymers. The nano-clay fillers stiffened all polymers, but only the dendritic polymers were reinforced. There is also an overall decreasing trend in the ultimate tensile strains (or ductility) of the polymers when more Cloisite®-20A nano-clays are added. As discussed in Chapter 6.3.2.1 (Polymer morphology) a good distribution of clay platelets can be observed in Figure 6.33(a), which suggests a good polymer-filler interaction in D_IB-MS10_C30. In contrast, there are clay agglomerations at various regions in the L_SIBS 34 matrix (see Figure 6.33(b)). While the clay agglomerates can still stiffen the polymer, they nevertheless become “hot-spots” of stress concentration and can delaminate prematurely to lead to an overall material rupture, as illustrated in Figure 6.36 and Figure 6.37. Due to the secondary network at work, the composites for both L_SIBS34 and D_IB-MS10 become more rigid against deformation to explain the lower ultimate tensile strain at failure.

In an empirical approach, the reinforcement effect of the Cloisite® can be described using the empirical reinforcement index (RI), which is defined as following:

$$RI = \frac{N}{N_0} / \frac{CB, content(\%)}{100} \quad \text{Eq. 6.1}$$

where N and N_0 , are the nominal tensile stress values obtained from the mechanical test with and without Cloisite® [210]. For the investigated composites, the RI values are denoted in Table 6.19.

Table 6.19: Calculated RI-values for D_IB-MS10 and L_SIBS34.

Cloisite® content [wt-%]	RI-value [-]	
	D_IB-MS10	L_SIBS34
10	14.55	7.24
20	7.50	2.87
30	4.80	1.71

The table demonstrates, that with increasing the Cloisite® the RI value is decreasing significantly, as expected when looking at the static tensile values. Interestingly the RI value as well as the tensile strength are the highest for 10 wt% Cloisite® content. As also the elongation at break is reduced in comparison to the neat material as well as the other composites, it is reasonable to claim that this content is sufficient to promote a secondary network structure in the polymer matrix. Further increasing the content will just stiffen the material, but the Cloisite® clay will agglomerate again and therefore reduces the mechanical performance. In contrast, for L_SIBS34 the RI-value is steadily decreasing with increasing Cloisite® content. In addition, the higher RI-value of the D_IB-MS10 composite show the higher effectiveness of using clay to reinforce the matrix compared to the linear material. Together with the static tensile results, this leads to the conclusion, that only in the dendritic SIBS matrix the nanoclay can be well dispersed to lead to a mechanical improvement. Based on this result, dynamic fatigue testing was not performed for these materials, because further research on the material and filler ratio is necessary.

6.3.2.4 Summary

This part of the work represents a study of the feasibility of using nanoclay (Cloisite®) to further modify the overall properties of both linear (L_SIBS) and dendritic (D_SIBS) PIB-based styrenic. The capability of nanoclays to stiffen and strengthen D_IB-MS10 is demonstrated in this study, while L_SIBS34 had poorer ultimate tensile strength with the addition of clay. The favorable modification of D_IB-MS10 by clay is due to the very good dispersion as shown by TEM, without any use of compatibilizers in the composite preparation other than the proprietary surface functionalization on the Cloisite®-20A clays. These data agree with literature reports that high molecular weight is needed for effective reinforcement. It must be noted that it is not possible to produce L_SIBS with higher than ~150,000 g/mol molecular weight.

7 Conclusions

This work presents the investigation of the influence of network structures on the dynamic fatigue behavior of innovative thermoplastic elastomers TPEs. In addition, it was successfully demonstrated how the approach of dynamic hysteresis measurements can be adjusted, to investigate the dynamic creep behavior of materials having different strength and compliance. Finally, using this modern methodology, it was firstly shown that high CB contents can be used to reinforce dendritic IBS polymers resulting in an enhancement of the short-term and long-term mechanical material properties. The study hence, lead to an innovative nano-composite based on dendritic poly(isobutylene-b-styrene) (IBS) block copolymers (D_IBS) including 37.5 wt% of CB (D_IB_MS17_150_CB), which provides an alternative material for medical grade silicon with increased fatigue properties.

The first part investigated the influence of additional chemical cross-links on the dynamic creep and fatigue performance of novel physically crosslinked TPE biomaterials. Therefore, nano-structured poly(aliphatic/aromatic-ester) multiblock copolymers (PEDs) were cross-linked post polymerization using various dosages of e-beam irradiation. The results indicated that chemical crosslinking mainly occurs within the PBT hard phase, shown by the decrease of the crystallinity as well as the shift of the higher glass transition measured during DMTA measurements. For these PEDs, an optimum of the irradiation dosage was found to be approximately 50 kGy, which leads to the formation of PBT hard phase agglomerations. This formation of an additional cross-linked network in the polymer is responsible for improving the mechanical properties (quasi-static and fatigue) of these PED multiblock copolymers. In general, PED multiblock copolymers can be considered as good candidates for medical applications. The additional e-beam irradiation step during the device fabrication, might demonstrate a disadvantage, due to the longer production time and hence, increased production costs per part. But as e-beam irradiation is widely used for sterilization of medical devices, a smart design of the device combining the e-beam irradiation for improving the material characteristics with the sterilization step can even lower the overall manufacturing steps and cost. This shows the high potential of these innovative class of biomaterials.

In contrast to the relatively hard PED multiblock copolymers, the softer SIBS copolymers were crosslinked during the polymerization process. Hence, it was found that for the samples with similar hard phase content (~30 wt%), the density of hard phases decreases with molecular weight, due to the increasing PIB molecular weight. More interesting was the finding concerning the dynamic creep and fatigue properties. When the materials are chemical similar, concerning the hard phase content (app. 30 wt.%) and the molecular weight M_n (app. 70,000 g/mol), a cross-linked structure has the potential to reduce the dynamic creep of these TPEs. For both PED and SIBS it could be shown that the mechanical performance was improved due to the presence of cross-links. But nevertheless the material performance is still far away from the commercial benchmarks medical grade thermoplastic urethanes (for PEDs) and medical grade silicone (for SIBS), which leads to the need of reinforcing the TPEs in order to qualify them for the use as biomaterial.

Therefore, the second part of this works showed how the addition of nano-scaled additives to the styrenic block copolymers affects their overall material performance. Both, carbon black and nanoclay significantly improved the mechanical performance of the SIBS materials. In case of the carbon black as well as the nanoclay filler, the reinforcing can be related the formation of a secondary reinforcing network. Using carbon black as an additive improved the dynamic fatigue behavior to a level comparable to medical grade cross-linked silicone rubber. In addition, this work shows the feasibility of nanoclays to stiffen and strengthen IBS block copolymers, while linear SIBS materials had poorer ultimate tensile strength with the addition of clay. The favorable modification of IBS by clay is due to the very good dispersion, which was

achieved without any use of compatibilizers in the composite preparation. For both classes of fillers it could be demonstrated, that a certain molecular weight of either the hard phase (carbon black) or the overall molecular weight (nanoclay) is necessary to obtain a fine filler distribution in the polymeric matrix. This is also the reason why linear SIBS materials cannot be reinforced using these nano-scaled fillers as it is not possible to produce L_SIBS with higher than ~150,000 g/mol molecular weight.

Furthermore, an independent study outside the thesis revealed that the carbon black as a filler reduced the water contact angle and also exhibited fine nano-scaled surface topography, most likely both contributing to the reduction of soft tissue capsule thickness *in vivo*. In conclusion, the results of these *in vitro* and *in vivo* biocompatibility studies demonstrated that the PIB-based thermoplastic elastomers reinforced with carbon represent a new and powerful concept in the development of innovative biomaterials [160] for soft tissue applications.

8 Outlook

The presented approach to investigate and improve the dynamic fatigue properties of poly(aliphatic/aromatic-ester) multiblock copolymers (PEDs) and SIBS copolymers by addition of a secondary network structure, showed the high potential of these TPEs to be used as novel biomaterials. Especially, using nano-scaled additives to reinforce SIBS copolymers lead the first time to an elastomeric biomaterial, which shows superior mechanical properties and a similar *in vitro* and *in vivo* biocompatibility compared to currently used silicones. From the introductory discussion on the “medical crisis” with silicone rubber breast implants (Chapter 1.1), it is clear that for the benefits of patients, new biopolymers are needed to be alternative shell materials with outstanding long-term fatigue properties to prevent dynamic rupture of the implant. In addition, the second major reason for implant explanations, the gel bleeding has to be addressed. In order to reduce or prevent gel bleeding of silicone breast implants the biomaterial needs enhanced barrier properties, to impede silicone oil from migrating through the implant into the host body. The developed PIB-based nano-composites can therefore contribute, as nano-additives can reduce the permeability of the material, by hindering the diffusion of molecules as depicted in Figure 8.1.



Figure 8.1: A good filler dispersion leads to a tortuous path, which impede fluid permeation.

To attain the goal of having a new biocompatible biomaterial with excellent barrier and fatigue properties, the choice of IBS polymers poses several main challenges. The first challenge will be in the preparation of IB-MS-clay nano-composites where there can be a high degree of filler dispersion and distribution in the IB-MS matrix. Figure 8.2 depicts the beneficial effect of a nano-scaled additive, here nano-clay, on the barrier properties (carrier gas CO₂) of a IBS block copolymer.

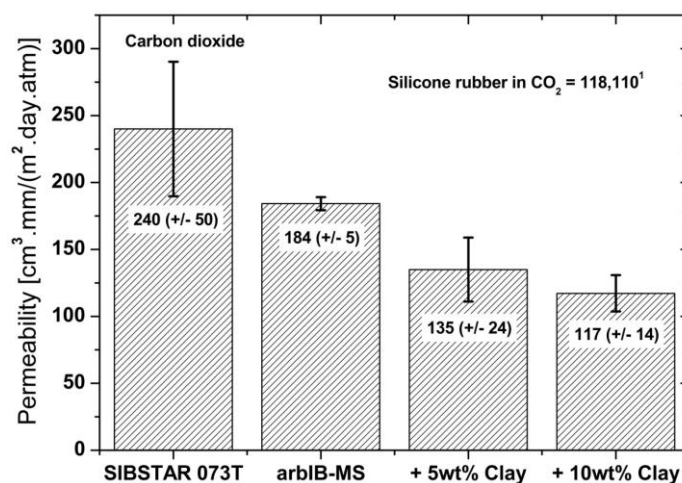


Figure 8.2: Influence of the nanoclay weight content on the permeability of a commercial linear SIBS (SIBSTAR 073T) and an IBS copolymer.

The second challenge lies in the biocompatibility of the nano-scaled filler and the IB-MS nanocomposites. Finally, the development of a cohesive research strategy to monitor and quantify also the changes in the barrier properties of the new materials after substantial dynamic fatigue cycles under an *in vivo* environment will be necessary to gain the certification as new biomaterial.

When the above approach is successful, it should be emphasized that the IB-MS-nanocomposites, are not restricted to the breast prosthesis, but can be readily applied to other medical devices, e.g. like venous vein valves.

9 Bibliography

- [1] Sastri, V.R., "Plastics in Medical Devices: Properties, Requirements and Applications," 3rd Edition, William Andrew Publishing, 2022
- [2] Cunningham, J.; Dolan, B.; Kelly, D. and Young, C. "National University of Ireland Galway Medical Device Sectoral Overview," Whitaker Institute for Innovation & Societal Change, Galway, 2015.
- [3] Population Reference Bureau, World Population Data sheet 2010.
- [4] Fortune Business Insights, Market Research Report Medical Device Market FBI100085, 2023 (Medical Devices Market Share, Growth, Trends | Forecast [2030] (fortunebusinessinsights.com)
- [5] Robert Koch Institute (ed.) and Association of Population-based Cancer Registries in Germany (ed.) Cancer in Germany 2011/2012. Incidence and Trends. 10th edition. Berlin, 2015.
- [6] German Centre for Cancer Registry Data, Robert Koch Institute: Database Query with estimates for cancer incidence, prevalence and survival in Germany, based on data of the population based cancer registries (DOI: 10.18444/5.03.01.0005.0017.0001 [Inzidenz, Prävalenz]; DOI: 10.18444/5.03.01.0005.0016.0001 [survival]). Mortality data provided by the Federal Statistical Office. www.krebsdaten.de/database, Latest Update: 13.09.2022, Retrieved: 19.01.2024
- [7] <http://www.hc-sc.gc.ca/hl-vs/iyh-vsv/med/implants-eng.php> (11 Oct 2010).
- [8] Peters W. and Pugash, R., *Ann. Plast. Surg.* 1993, 31(1), pp. 7-9.
- [9] Robinson, O. G.; Bradley, E. L. and Wilson, D. S., *Ann. Plast. Surg.* 1995, 34(1), pp. 1-6.
- [10] Yoshida, S.H.; Swan, S.; Teuber, S.S. and Gershwin, M. E., *Life Sci.* 1995, 56(16), pp. 1299-1310.
- [11] Jenkins, M.E.; Friedman, H.I. and Vonrecum, A. F., *J. Investig. Surg.* 1996, 9(1), pp. 1-12.
- [12] Ahn, C.Y.; Ko, C.Y. Wagar, E.A.; Wong, R.S. and Shaw, W. W., *Plast. Reconstr. Surg.* 1996, 98(7), pp. 1225-1229.
- [13] W Beekman, W.H.; Feitz, R.; Hage, J.J. and Mulder J.W., *Plast. Reconstr. Surg.* 1997, 100(7), pp. 1723-1726.
- [14] Peters, V.; Smith, D. and Lugowski, S., *Ann. Plast. Surg.* 1999, 43(3), pp. 324-330.
- [15] Ikeda, D.M.; Borofsky, H.B.; Herfkens, R.J.; Sawyer-Glover, A.M.; Birdwell, R.L. and Glover, G. H., *Plast. Reconstr. Surg.* 1999, 104(7), pp. 2054-2062.
- [16] Flassbeck, D.; Pfeleiderer, B.; Klemens, P.; Heumann, K. G.; Eltze, E. and Hirner A. V., *Anal. Bioanal. Chem.* 2003, 375(5), pp. 356-362.
- [17] Tarantino, I.; Banic, A. and Fischer, T., *Plast. Reconstr. Surg.* 2006, 117(5), pp. 1387-1394.
- [18] U.S. Food and drug Administration, Breast Implant Complications Booklet, 2014
- [19] U.S. Food and drug Administration, Risk and Complications of Breast Implant (<http://www.fda.gov/MedicalDevices/ProductsandMedicalProcedures/ImplantsandProsthetics/BreastImplants/ucm064106.htm> (2023-12-15).
- [20] American Society of Plastic Surgeons, National Clearinghouse of Plastic Surgery Procedural Statistics, 2015
- [21] Young, V. L. and Watson, M. E., *Clin. Plast. Surg.* 2001, 28(3), pp. 451-483.
- [22] Christ, H.J. "Ermüdungsverhalten metallischer Werkstoffe." 2nd Edition, Wiley-VCH Verlag GmbH&Co. KGaA, 2009.
- [23] Varvani-Farahani, A. "Fatigue damage of materials. Southampton," WIT Press, 2003.
- [24] Swanson, S.R. "Handbook of fatigue testing." Philadelphia, American Society for Testing and Materials, 1974.
- [25] Schijve, J. "Fatigues of Structures and Materials", Kluwer AP, Dordrecht–Boston, 2001.
- [26] Coffin, Jr., L.F., *Appl. Math. Res.* 1962, 1, pp. 129-141.
- [27] Manson S.S. and Hirschberg, M.H. *Fatigue, an Interdisciplinary Approach*, Syracuse University, Syracuse (1964), pp. 133-178.
- [28] Schijve, J., *Mate. Sci.*, 2003, 39, pp.307-333.
- [29] Gough, H.J., *Proc. ASTM*, 1933, pp. 3–114.
- [30] Orowan, E., *Proc. Roy. Soc. (A)*, 1939, 171, p. 79.
- [31] Head, A. K., *Phil. Mag.*, 1953, 44, pp. 925–938.
- [32] Stroh, A.N., *Proc. Roy. Soc. (A)*, 1955, 223, p. 404.
- [33] Forsyth, P.J.E., *Roy. Aircraft Est., Tech. Note Met.*, 1957, 257.
- [34] Ryder, D.A., *Roy. Aircraft Est., Tech. Note Met.*, 1958, 288.
- [35] Cottrell A.H. and Hull, D. *Proc. Roy. Soc. (A)* 1957, pp. 211-213.

- [36] Mott, N.F., Proc. Roy. Soc., Math. Phys. Sciences, 1957, 242, No. 1229.
- [37] Averbach, B.L.; Felbeck, D.K.; Hahn, G.T. and Thomas, D.A. "Fracture," Proc. of the Internat. Conf. on the Atomic Mechanisms of Fracture, Techn. Press, 1959, MIT, Wiley.
- [38] Forsyth, P. J. E. "The Physical Basis of Metal Fatigue," Blackie and Son, London (1969).
- [39] Backofen, W.A. Proc. of the Internat. Conf. on the Atomic Mechanisms of Fracture, Techn. Press, MIT, Wiley (1959), pp. 435-449.
- [40] Irwin, G.R. Trans. ASME, J. Appl. Mech. 1957, 24, pp. 361-364.
- [41] Paris, P. C; Gomez, M.P. and Anderson, W.E., Trend Eng. 1961, 13, pp. 9-14.
- [42] ASTM International 1963. ASTM STP 91A, A guide for fatigue testing and the statistical analysis of fatigue data.
- [43] Bellows R.S.; Muju S. and Nicholas, T., Int. J. Fract. 1999, 21, pp. 687-697.
- [44] Renz, R.; Altstädt, V. and Ehrenstein, G.W., J. Reinf. Plast. Compos., 7, 1988. p.413-434
- [45] Macosko, C.W. "Rheology Principles Measurements and Applications." Wiley-VCH. Toronto. 1994.
- [46] Raue, F. and Ehrenstein, G.W., J. Elastomers Plast. 1999, 31(3), pp.194-204.
- [47] Orth, F.; Hoffmann, L.; Zilch-Bremer H. and Ehrenstein, G.W., Compos. Struct. 1993, 24, pp. 265-272.
- [48] El Fray, M. and Altstädt, V., Polymer 2003, 44(16), pp. 4635-4642.
- [49] Altstädt, V. "Hysteresismessungen zur Charakterisierung der mechanisch-dynamischen Eigenschaften von R-SMC.", PhD Dissertation University Kassel. 1987
- [50] El Fray, M. and Altstädt, V., Polymer 2004, 45(1), pp. 263-273.
- [51] El Fray, M. "Nanostructured elastomeric biomaterials for soft tissue reconstruction," Publishing House of the Warsaw University of Technology, 2003, Warszawa, pp. 1-144.
- [52] El Fray, M. and Altstädt, V., Polymer 2003, 44(16), pp. 4643-4650.
- [53] Park, J.B. and Lakes, R.S. "Biomaterials: An Introduction," Springer-Verlag New York, 2007.
- [54] Dumitriu, S. "Polymeric Biomaterials," Revised and Expanded, 2. Edition ed., New York: Marcel Dekker AG, 2001
- [55] Williams, D.F. "The Williams Dictionary of Biomaterials," Liverpool: Liverpool University Press, 1999.
- [56] Ratner, B.D.; Hoffman, A.S.; Schoen, F.J. and Lemons, J.E. "Biomaterial Science: an Introduction to Materials in Medicine," Academic Press, San Diego 1996.
- [57] Black, J. "Biological performance of Materials," Marcel Dekker, New York 1999.
- [58] Wise, D.L. "Biomaterials and Bioengineering Handbook," New York: Marcel Dekker Inc, 2000.
- [59] Misof, K.; Rapp, G. and Fratzl, P., Biophys. J. 1997, 72, pp. 1376-1381.
- [60] Ehrenstein, G.W. "Polymer-Werkstoffe," 3rd Edition, Carl Hanser Verlag, Munich 2011.
- [61] Murphy, W.; Black, J and Hastings, G. "Handbook of Biomaterial properties," Edition 2, Springer, 2016.
- [62] Gallagher, A.J.; Ní Anniadh, A.; Bruyere, K.; Otténio, M.; Xie, H. and Gilchrist, M.D.; IRCOBI Conference 2012; Dynamic Tensile Properties of Human Skin.
- [63] Yoganandan, N.; Nahum, A.M. and Melvin, J.W., "Accidental Injury – Biomechanics and Prevention," Springer-Verlag New York, 2015
- [64] Silver, F.H. "Biomaterials, Medical devices and Tissue Engineering", Chapman and Hall, London 1994.
- [65] Cronin T. and Gerow, F. "Augmentation mammoplasty: a new "natural feel" prosthesis." Excerpta Medica International Congress Series 1963, pp.41-49.
- [66] Lesesne, C.P., Aesthetic Plast. Surg. 1997, 21(2), pp.93-96.
- [67] Lantieri, L. A.; Cosnes, A.; Wechsler, J. and Baruch, J. P., Eur. J. Plast. Surg. 1999, 22(5-6), pp. 260-262.
- [68] <http://www.fda.gov/MedicalDevices/ProductsandMedicalProcedures/ImplantsandProsthetics/BreastImplants/ucm064461.htm> (25. Sep. 2013).
- [69] <http://www.fda.gov/MedicalDevices/ProductsandMedicalProcedures/ImplantsandProsthetics/BreastImplants/ucm063871.htm> (20 Sep 2013).
- [70] Wilks, E.S. "Industrial polymers handbook – products, processes, applications" (Vol. 3), Wiley-VCH Verlag GmbH, 2001, p. 1349.
- [71] Nusil Technology, Product Profile – MED82-5010 Series, Nusil Technology, 2007.
- [72] Morton, M. "Rubber technology," Springer Netherlands, Dordrecht, 1999.
- [73] Puskas, J.E. and Chen, Y.H., Biomacromolecules 2004, 5(4), pp. 1141-1154.

- [74] Lim, G.T.; Valente, S.A.; Hart-Spicerc, C.R.; Evancho-Chapman, M.M.; Puskas, J.E.; Horner, W.I. and Schmidt, S.P., *J. Mech. Behav. Biomed. Mater.* 2013, 21, pp. 47-56.
- [75] Holden, G.; Legge, N.R.; Quirk, N. and Schroeder, H.E. "Thermoplastic Elastomers," 3rd Edition, Hanser Publishers, Munich, 2004.
- [76] Hamley, I.W., *J. Phys. Condens. Matter.* 2001, 13 (33), pp. 643-673.
- [77] Puskas, J.E.; Antony, P.; El Fray, M. and Altstädt, V., *Eur. Poly. Journal.* 2003, 39 (10), pp. 2041-2049.
- [78] Shivers, J. S. (to DuPont). U.S. Patent 3023192, 27 February 1962.
- [79] Lelah, M.D. and Cooper, S.L. "Polyurethanes in Medicine," CRC Press: Boca Raton, Florida, 1986.
- [80] Lelah, M.D.; Lambrecht, L.K.; Young, B.R. and Cooper, S.L., *J. Biomed. Mater. Res.* 1983, 17, 1, pp.1 - 22.
- [81] Pinchuk, L., *J. Biomater. Sci. Polym. Ed* 1994; 6 (3), pp. 225–267.
- [82] Pinchuk, L. "Crack prevention of implanted prostheses; grafting a siloxane elastomer onto biocompatible surface.", U.S. Patent 4851009, 1989.
- [83] Pinchuk, L.; Esquivel, M.C. and J.B. Martin Jr., "Polyurethane/silicone composites for long-term implant in the human body." Proceedings of the society of plastic engineerings ANTEC, Montreal, May 1991, pp. 1802–1804.
- [84] Adhikari, R.; Gunatillake, P.A.; Maijs, G.F.; Martin, D.J.; Poole-Warren, L.A. and Schindhelm, K. "Synthesis and biostability of low modulus siloxane-based polyurethanes." Transactions of the society for biomaterials: sixth world biomaterials congress, Minneapolis, part II, 2000, p. 812.
- [85] Christenson, E.M. and Anderson, J.M. "the effect of silicone on the biostability of poly(ether urethanes). Transactions of the society for biomaterials: 28th annual meeting, Tampa, Florida, April 24 to 27, 2002.
- [86] Ebert, M.; Ward, R.; Anderson, J.; Tain, Y.; McVenes, R. and Stokes, K. "Chronic Environmental Stress Cracking Resistance of Polyurethanes with Polyether and Polysiloxane Soft Segments." Society of Biomaterials: 29th Annual Meeting Transactions, 2003. pp. 535.
- [87] Ebert, M.; Ward, R.; Anderson, J.; Tain, Y.; McVenes, R. and Stokes, K. "Screening of polyurethanes with polyether and polysiloxane soft segments for resistance to environmental stress cracking." Society of Biomaterials: 29th annual meeting transactions, 2003, pp. 542.
- [88] Ebert, M.; Ward, R.; Anderson, J.; Tain, Y.; McVenes, R. and Stokes, K. "Environmental stress cracking resistance of polyetherurethanes with fluorocarbon surface modifying endgroups." Society of Biomaterials: 29th annual meeting transactions, 2003, pp. 538.
- [89] Ebert, M.; Ward, R.; Anderson, J.; Tain, Y.; McVenes, R. and Stokes, K. "Chronic environmental stress cracking resistance of polyetherurethanes with polyethyleneoxide surface modifying endgroups." Society of biomaterials: 29th annual meeting transactions, 2003, pp. 536.
- [90] Zhou, Q.; Cass-Bejar, I.; Urbanski, P. and Stokes, K., *J. Biomed. Mater. Res.* 1995, 29, pp. 467-75.
- [91] Pinchuk, L.; Wilson, G.J.; Barry, J.J.; Schoephoerster, R.T.; Parel, J.-P. and Kennedy, J.P., *Biomaterials* 2008, 29, pp. 448-460.
- [92] Kimberly, A.C.; Buckalew, A.J.; Schley, J.L.; Chen, X.; Jolly, M.; Alkatout, J.A.; Miller, J.P.; Untereker, D.F.; Hillmyer, A.M. and Bates, F.S., *Macromolecules*, 2012, 45 (22), pp. 9110-9120
- [93] Kaszas, G.; Puskas, J.E.; Hager, W. and Kennedy, J.P. U.S. Patent 4 946 897, 1990.
- [94] Kaszas, G.; Puskas, J.E.; Hager, W. and Kennedy, J.P., *J. Polym. Sci., Polym. Chem.*, 1991, 29, pp. 427-435.
- [95] Puskas, J.E. and Kaszas, G., *Rubber Chem. Techn.*, 1996, 69 (3), pp. 462-475.
- [96] Jacob, S. and Kennedy, J.P., *Adv. Polym. Sci.* 1999, 146, pp. 1-38.
- [97] Puskas, J.E.; Pattern, W.; Wetmore, P.W. and Krukoniš, V., *Rubber Chem. Techn.* 1998, 72, pp. 559.
- [98] Roovers, J. "Branched Polymers I"; Springer Link, Berlin, 1999.
- [99] Kwon, Y.; Antony, P.; Paulo, C. and Puskas, J.E., *Polym. Prepr.* 2002, 43, pp. 266.
- [100] TS Polymer (Data Sheet) Kuraray Co., Ltd., Tsukuba Research Lab 1997.
- [101] Taxus Express 2 Paclitaxel-Eluting Coronary Stent System (Monorail and Over the Wire); Publication PO30025; U.S. Food and Drug Administration; U.S. Government Printing Office: Washington, DC, 2004.
- [102] Györ, M.; Fodor, Z.; Wang, H.C. and Faust, R., *J. Macromol. Sci., Pure Appl. Chem.* 1994, 31 (12), pp. 2055-2065.

- [103] Puskas, J.E.; EL Fray, M.; Tomkins, M.; Dos Santos, L.M.; Fischer, F. and Altstädt, V., *Polymer* 2009, 50 (1), pp. 245-249.
- [104] El Fray, M.; Prowans, P.; Puskas, J.E. and Altstädt, V., *Biomacromolecules* 2006, 7, pp. 844-850.
- [105] Legocka, I.; Zimek, Z. and Wozniak, A., *Radiat. Phys. Chem.* 1998, 52, pp. 277-281.
- [106] Legocka, I.; Zimek, Z.; Mirkowski, K. and Nowicki, A., *Radiat. Phys. Chem.* 2000, 57, pp. 411-416.
- [107] Rouif, S., *Nucl Instrum Meth B.* 2005, 236, pp. 68-72.
- [108] Stein, H. *ASM International* 2 (1992) pp. 167-171.
- [109] Gronsky, M.; Ranganathan, R. and Pruitt, L., *Polymer* 1996, 37 (14), pp. 2909-2913.
- [110] Woo, L. and Sandford, C. L., *Radiat. Phys. Chem.* 2002, 63, pp. 845-850.
- [111] Elzubair, A.; Suarez, J.C.M; Bonelli, C.M.C and Mano, E.B., *Polym. Test.* 2003, 22 (6), pp. 647-649.
- [112] International Topical Meeting on Nuclear Research Applications and Utilization of Accelerators IAEA, Viena (Austria), 4th – 8th May 2009.
- [113] Ranogajec, F.; Mlinac-Misak, M. and Hell, Z., *Polimeri* 2008, 29 (4), pp. 236-243.
- [114] El Fray, M.; Bartkowiak, A.; Prowans, A. and Slonecki, J., *J. Mater. Sci. Mater. Med.* 2000, 11, pp. 757-762.
- [115] Grossman, R.F. "Antioxidants, polymer modifiers and additives." Marcel Dekker, Basel 2001.
- [116] Clough, R.L. and Shalaby, S.W. "Irradiation of Polymers: Fundamentals and Technological Applications," American Chemical Society, Washington DC 1999.
- [117] Bhowmick, A.K. and Stephens, H.L. "Handbook of Elastomers." Merceel Dekker, New York 2001.
- [118] Kojima, Y.; Usuki, A.; Kawasumi, M.; Okada, A.; Fukushima, Y.; Karauchi, T. and Kamigaito, O., *J. Mater. Res.* 1993, 6, pp.1185-1189.
- [119] Sengupta, R.; Chakraborty, S.; Bandyopadhyay, S.; Dasgupta, S.; Mukhopadhyay, R.; Auddy, K.; Deuri, A.S., *Polym. Eng. Sci.* 2007, 47 (11), pp. 1956-1974.
- [120] Jakab, E. and Omastová, M., *J. Anal. Appl. Pyrolysis.* 2005, 74, pp. 204-214.
- [121] Puskas, J.E.; Dos Santos, L.M.; Kaszas, G. and Kulbaba, K. J., *Polym. Sci. Pol. Chem.* 2009, 47, pp. 1148-1158
- [122] Jayasree, T.K. and Predeep, P., *J. Elastomers Plast.* 2008, 40, pp. 127-146.
- [123] Yamauchi, K.; Akasaka, S.; Hasegawa, H.; Koizumi, S.; Deeprasertkul, C.; Laokijcharoen, P.; Chamchang, J. and Kornduangkaeo, A., *Compos. - A: Appl. Sci. Manuf.* 2005, 36, pp. 423-429.
- [124] Teoh, S.H. *Polymer* 1990; 31, pp. 2260-2266.
- [125] Teoh, S.H.; Cherry, B.W. and Kausch, H.H., *Int. J. Damage Mech.* 1992, 1, pp. 245-256.
- [126] Teoh, S.H., *Biomaterials* 1993, 14(2), pp. 132-136.
- [127] Teoh, S.H. "Predicting the life and design stresses of medical plastics under creep conditions." in: Kambic H.E., Yokobori A.T. Jr, editors. *ASTM STP 1173: Biomaterials' mechanical properties.* American Society of Testing and Materials: Philadelphia, 1994, 77-86.
- [128] Teoh, S.H. *Int. J. Fatigue* 2000, 22, pp. 825-837.
- [129] Kurtz, S.M. "The UHMWPE Handbook," Elsevier Academic press, SanDiego, 2004
- [130] Baker, D.A.; Hastings, R.S. and Pruitt, L., *J. Biomed. Mater. Res.* 1999, 46(4), pp. 573-581.
- [131] Baker, D.A.; Hastings, R.S. and Pruitt, L., *Polymer* 2000, 41 (2), pp. 795-808.
- [132] Baker, D.A.; Bellare, A and Pruitt, L., *J. Biomed. Mater. Res.* 2003, 66A, pp. 146-154.
- [133] Edidin, A.A.; Pruitt, L.; Jewett, C.W.; Crane, D.J.; Roberts, D and Kurtz, S.M., *J. Arthroplasty* 1999, 14(5), pp. 616-627.
- [134] Hastings, R.S., Pruitt, L., *J. Biomed. Mater. Res.* 1999, 46 (4), pp. 573-581.
- [135] Kurtz, S.M.; Pruitt, L.; Jewett, C.W.; Crawford, R.P.; Crane, D.J. and Edidin, A.A, *Biomaterials* 1999, 19(21), pp. 1989-2003.
- [136] Meyer, R and Pruitt, L., *Polymer*, 2001, 42, pp 5293-5306.
- [137] Pruitt, L. and Suresh, S., *Phil. Mag. A* 1993, 67, pp. 1219-1245
- [138] Pruitt, L. and Bailey L., *Polymer* 1998, 39, pp. 1545–1553.
- [139] Gencur, S.J.; Rimnac, C.M. and Kurtz, S.M., *Biomaterials* 2003, 24 pp. 3947-3954.
- [140] Gomoll, A.; Wanich, T. and Bellare, A., *J. Orthop. Res.* 2002, 20, pp. 1152-1156.
- [141] O'Connor, D.O.; Muratoglu, O.K.; Bragdon, C.R.; Lowenstein, J.; Jasty, M. and Harris W.H.. "Wear and high cycle fatigue of highly crosslinked UHMWPE." In: *Transactions of 44th Annual Meeting of the Orthopaedic Research Society*; 1999; Anaheim, CA. pp. 816.
- [142] Furmanski, J.; Feest, E. and Pruitt, L. "Static Mode Fatigue of UHMWPE" (Paper presented at the 2nd International Congress on the Mechanics of Biomaterials and Tissues, Kauai, HI, 2007).

- [143] Furmanski, J.; Rimnac, C.M. and Pruitt, L. "Brittle Fatigue Crack Propagation of UHMWPE and Its Implications for Total Joint Replacements" (Paper presented at the 14th International Conference on Deformation, Yield and Fracture of Polymers, Kerkrade, The Netherlands, (2009)
- [144] Pruitt, L. and Fumanski, J., JOM 2009, 61 (9), pp. 14-30.
- [145] Galetz, M.C.; Goetz, C.; Adam, P. and Glatzel, U., Adv. Eng. Mater. 2007, 9(12), pp. 1089-1096.
- [146] Chen, K.; Kang, G.; and Lu, F., J. Polym. Res. 2015, 22 (11) pp. 217-225.
- [147] ASTM International 2006. ASTM D1708, Standard test method for tensile properties of plastics by use of microtensile specimens.
- [148] Puskas, J.E.; Antony, P. and Paulo, C. U.S. Patent 6 747 098, 2004
- [149] Puskas, J.E., Kwon, Y.; Antony, P. and Bhowmick, A.K., J. Polym. Sci. A, 2005, 43(9), pp. 1811-1826.
- [150] Fakirow, S. "Handbook of Condensation Thermoplastic Elastomers," Weinheim Wiley-VHC Verlag GmbH & Co. KGaA, 2005.
- [151] El Fray, M. and Prowans, P., Sci Papers Institute of Organic and Polymer Technology (Wroclaw), 2003, 52, pp. 481-484.
- [152] Prowans, P.; El Fray, M. and Slonecki, J., Biomaterials 2002, 23(14), pp. 2973-2978.
- [153] Renke-Gluszko, M. and El Fray, M., Biomaterials 2004, 25(21) pp. 5191-5198.
- [154] Kaszas, G.; Puskas, J.P. and Kennedy J.P., Polym. Bull. 1987, 18(2), pp. 123-130.
- [155] Kennedy J.P., U.S. Patent 4 946 899, 1990.
- [156] Ranade, S.V.; Miller, K.M.; Richard, R. E.; Ken, C. A.; Allen, M.J. and Helmus, M.N., J. Biomed. Mat. Res. 2004, 71A, pp. 625-634.
- [157] Puskas, J.E. and Grasmüller, M., Makromol. Chem. Macromol. Symp. 1998, 132, pp. 117-126.
- [158] Puskas, J.E.; Paulo C. and Altstädt V., Rubber Chem. Technol. 2002, 75, pp. 853-864.
- [159] Foreman, E.A.; Puskas, J.E. and Kaszas, G., J. Polym. Sci., Part A: Polym. Chem. 2007, 45, pp. 5847-5856.
- [160] Puskas, J.E.; Foreman-Orlowski, E.A.; Lim, G.T.; Porosky, S.E.; Evancho-Chapman, M.M.; Schmidt, S.P.; El Fray, M.; Piatek, M.; Prowans, P. and Lovejoy, K., Biomaterials 2010, 31, pp. 2477-2488.
- [161] Ratner, B.D.; Hoffman, A.S.; Schoen, F.J. and Lemons, J.E., Biomaterials Science, 3rd Edition. San Diego, CA: Elsevier, 2013.
- [162] Puskas, J.E.; Dos Santos, L.M.; Fischer, F.; Goetz, C.; El Fray, M.; Altstädt, V. and Tomkins, M., Polymer 2009, 50 (2), pp. 591-597.
- [163] NuSil Technology, Material Data Sheet MED-4050, 2009
- [164] NuSil Technology, Material Data Sheet MED-4750, 2009.
- [165] Dow Plastic, Material Data Sheet Pellethane® 2363-80A, 2009.
- [166] Kaneka Corporation, Material Data Sheet SIBSTAR 073T, 2012.
- [167] Kaneka Corporation, Material Data Sheet SIBSTAR 103T, 2012
- [168] DIN ISO 53504, Determination of tensile stress/strain properties of rubber, 2005.
- [169] El Fray, M. and Slonecki, J., Angew. Makromol. Chem. 1999, 266, pp. 30-36.
- [170] Sawyer, L.C.; Grubb, D.T. and Meyers, G.F. "Polymer Microscopy" 3rd Ed., Springer New York, 2008.
- [171] Hesketh, T.R.; van Bogart, J.W.C. and Cooper, S.L., Polym. Eng. Sci. 1980, 20, pp. 190-197.
- [172] Koberstein, J.T.; Galambos, A.F. and Leung, L.M., Macromolecules 1992, 25, pp. 6195-6204.
- [173] Jimenez, G.; Asai, S.; Shishido, A. and Sumita, M., Eur. Polym. J. 2000, 36, pp. 2039-2050.
- [174] ASTM International 2006. ASTM D 5026, Standard test method for plastics: Dynamic mechanical properties: in tension.
- [175] ASTM International 2006. ASTM D412-06a: Standard test method for vulcanized rubbers and thermoplastic elastomers – Tension.
- [176] Schechtman, H. and Bader, D.L., Eng. In. Med. 1994, 208, pp. 241-248.
- [177] Schechtman, H. and Bader, D.L., J. Biomech. 1997, 30, pp. 829-835.
- [178] Götz, C.; Handge, U.A.; Piatek, M.; El Fray, M. and Altstädt V., Polymer 2009; 50 (23), pp. 5549-5507.
- [179] Grellmann, W. and Seidler, S. "Deformation and fracture behaviour of Polymers" Springer, Heidelberg, 2001.
- [180] Oral, E.; Wannomae, K.K.; Rowell, S.L. and Muratoglu, O.K., Biomaterials 2006, 27(11) pp. 2434-2439.
- [181] Packer, L., Am. J. Clin. Nutr. 1991, 53, pp. 1050S-1055S.

- [182] Packer, L. and Kagan, V.E. "Vitamin E: the antioxidant harvesting center of membranes and lipoproteins." In: L. Packer and J. Fuchs, Editors, Vitamin E in health and disease, New York: Marcel Dekker, Inc., 1993.
- [183] Burton, G. and Ingold, K., *J. Am. Chem. Soc.* 1981, 103, pp. 6472-6477.
- [184] Oertel, G., "Polyurethane Handbook" 2nd Ed. Hanser Gardner Publication, Cincinnati, 1996.
- [185] Takahara, A.; Hamada, K.; Kajiyama, T. and Takayanagi, M., *J. Biomed. Mater. Res.* 1985, 19, pp.13- 34.
- [186] Takahara, A.; Hamada, K.; Kajiyama, T. and Takayanagi, M., *J. Biomed. Mater. Res.* 1985, 26, pp. 987-996.
- [187] Szycher, M. "Handbook of Polyurethanes" CRC Press Inc., Boca Raton, Florida (1986).
- [188] Götz, C.; Lim, G.T.; Puskas, J.E. and Altstädt, V., *J. Mech. Behav. Biomed. Mater.*, 2012, 10C, pp. 206-215.
- [189] Kaszas, G., *Polym. Mat. Sci. Eng.* 1993, 68, pp.375-376.
- [190] Puskas, J.E.; Muñoz-Robledo, L.; Hoerr, R.A.; Foley, J.; Schmidt, S.P.; Evancho-Chapman, M.; Dong, J.; Frethem, C. and Haugstad, C. „Drug Eluting Stent Coatings." *Wiley Interdisciplinary Reviews WIRE* 2009, 1(4), pp. 451-462.
- [191] Storey, R.F. and Baugh, D.W., *Polymer*, 2000, 41(9), pp. 3205-3211.
- [192] Mark, J. E. "Polymer Data Handbook," 2nd Ed. Oxford: Oxford University Press, 2009.
- [193] Sperling, L.H. "Introduction to Physical Polymer Science," Bethlehem:John Wiley & Sons, Inc., 4th ed. 2006.
- [194] Hill, R.M. and Dissado, L.A., *J. Polym. Sci. Pol. Phys.* 1984, 22(12), pp. 1998-2008.
- [195] Drobny, J.G. "Handbook of Thermoplastic Elastomers." Norwich, NY: William Andrew Publishing, 2007.
- [196] Duck, F. A., "Physical Properties of Tissue: A Comprehensive Reference Book," 1990, pp.143-160.
- [197] Götz, C.; Handge, U.A.; Piatek, M.; El Fray, M. and Altstädt; V., *Kautsch. Gummi Kunstst.* 2009, 62 (7/8), pp. 396-398.
- [198] McCrum, N.G.; Buckley, C.P. and Bucknall, C.B. "Principles of Polymer Engineering," 2nd ed., Oxford University Press, Oxford, 1997.
- [199] Götz, C.; Lim, G.T.; Puskas, J.E. and Altstäd, V., *J. Mech. Behav. Biomed. Mater.* 2014, 39, pp. 355-365.
- [200] Lim, G.T.; Foreman-Orlowski, E.; Pavka, P.; Götz, C.; Altstädt V. and Puskas, J.E., *Rubber Chem. Technol.*, 2009, 82, pp. 461-472.
- [201] Cavallo, A.; Müller, M.; Wittmer, J.P.; Johner, A. and Binder, K., *J. Condens. Matter Phys.* 2005, 17(20), pp. 1697-1709.
- [202] Rittigstein, P. and Torkelson, J.M., *J. Polym. Sci., Part B: Polym. Phys.* 2006, 4, pp. 2935-2943.
- [203] Starr, F.W.; Schröder, T.B. and Glotzer, S.C., *Phys. Rev* 2001, E64, pp. 21802.
- [204] Starr, F.W.; Schröder, T.B. and Glotzer, S.C., *Macromolecules* 2002, 35(11), pp. 4481-4492
- [205] Kalfus, J. and Jancar, J. *Polymer* 2007,48(14), pp. 3935-3937.
- [206] ASTM International 2007. ASTM F703-07: Standard specification for implantable breast prostheses.
- [207] Mai, Y.W. and Yu, Z.Z., "Polymer nanocomposites" Cambridge: Woodhead Publishing Limited 2006.
- [208] Leyva, M.E.; Barra, G.M.O.; Moreira, A.C.F.; Soares, B.G. and Khastigir, D., *J. Polym. Sci., Part B: Polym. Phys.* 2003, 41, pp. 2983-2997.
- [209] Xu, P. and Mark, J.E. *Polym. Gels Netw.*, 1995, 3, pp. 255-266.
- [210] Markovic, G.; Devic, S.; Marinovic, M.; and Budinski-Simendic, J., *Kautsch. Gummi Kunstst.* 2009, 62(6), pp 299-305.

10 Curriculum Vitae

Personal Data

Christian Götz

Date of Birth: 7th January 1981, in Bayreuth

Family Status

Married, two children

Nationality

German

Education

07/2000

Abitur (Bayreuth)

09/2006

Dipl.-Ing. Univ. (Bioengineering) University of Bayreuth

01/2007 - 03/2011

Scientific staff at University Bayreuth, Department of Polymer Engineering

Civilian Service

8/2000 to 6/2001

Bavarian Red Cross "Blood Transfusion Service"

Professional Experience

06/2011 – 01/2017

Tüv Süd Product Service GmbH
Non-active Medical Devices (PS-MHS-NAM4) - Product Specialist, Senior Product Specialist and Lead-Auditor

02/2017 – 02/2020

Tüv Süd Product Service GmbH
Non-active Medical Devices (PS-MHS-CCV1)
Teamleader Center of Cardiovascular Excellence

03/2020 - today

Tüv Süd Product Service GmbH
Non-active Medical Devices (PS-MHS-TD1)
Department Manager Non-Active Medical Devices

11 List of publications

Refereed Journals

C. Götz, G.T. Lim, J.E. Puskas, V. Altstädt

The effect of carbon black reinforcement on the dynamic fatigue and creep of polyisobutylene-based biomaterials

Journal of the Mechanical Behavior of Biomedical Materials 39, pp. 355–365, 2014.

C. Götz, G.T. Lim, J.E. Puskas, V. Altstädt

Investigation of structure–property relationships of polyisobutylene-based biomaterials: Morphology, thermal, quasi-static tensile and long-term dynamic fatigue behavior

Journal of the Mechanical Behavior of Biomedical Materials 10C, pp. 206–215, 2012.

U. A. Handge, A. Galeski, S. C. Kim, D. J. Dijkstra, C. Götz, F. Fischer, G. T. Lim, V. Altstädt, C. Gabriel, M. Weber, H. Steininger

Melt Processing, Mechanical and Fatigue Crack Propagation Properties of Reactively Compatibilized Blends of Polyamid 6 and an Acrylonitrile-Butadien-Styrene Copolymer;

Journal of Applied Polymer Science, Vol. 124 Issue 1, pp. 740–754 , 2011

J.E. Puskas, L.M. Dos Santos, F. Fischer, C. Götz, M. El Fray, V. Altstädt, M. Tomkins

Fatigue Testing of Implantable Specimens: Effect of Sample Size and Branching on the Dynamic Fatigue Properties of Polyisobutylene-based Biomaterials

Polymer 50(2), pp. 591–597, 2009

C. Götz, U.A. Handge, M. Piatek, M. El Fray, V. Altstädt;

Influence of E-Beam Irradiation on the Dynamic Creep and Fatigue Properties of Poly(aliphatic/aromatic-ester) Copolymers for Biomedical Applications;

Polymer 50, pp. 5499–5507, 2009

C. Götz, U.A. Handge, M. Piatek, M. El Fray, V. Altstädt

Influence of E-Beam Irradiation on Poly(aliphatic/aromatic-ester) Multiblock Copolymers Used as Biomaterials;

Kautschuk Gummi Kunststoffe, Jahrgang 62, 7-8, pp. 396-398, 2009

G.T. Lim, E. Foreman-Orlowski, P. Pavka, C. Götz, V. Altstädt and J. E. Puskas

Novel Polyisobutylene-based Biocompatible TPE Nanocomposites

Rubber Chemistry and Technology, Vol. 82, pp. 461-472, 2009

M. Galetz, C. Goetz, P. Adam, U. Glatzel;

Hysteretic Heating During Cyclic Loading of Medical Grade Ultra High Molecular Weight Polyethylene;

Advanced Engineering Materials, Vol. 9, pp. 1089-1096, 2008

Oral Presentations on National and Internationals Conferences

V. Altstädt, C. Götz, M. Kempf, R. Zeiler, F. Wolff-Fabris, F. Fischer

Analysing the Fatigue Behaviour of Polymers Using Modern Investigation Methods

0. Jahrestagung der Gesellschaft für Umweltsimulation e.V. Pfinztal (März / April 2011)

V. Altstädt, C. Götz, F. Wolff-Fabris

Fatigue Behavior of Polymer Nanocomposites

The 18th International Conference on Composite Materials Jeju, Korea (August 2011)

V. Altstädt, F. Fischer, C. Götz, F. Wolff-Fabris

Fatigue Behaviour of Polymer Blends and Nanocomposites

14th International Scientific Conference on „Polymeric Materials“ Halle / Saale (September 2010)

C. Götz, F. Fischer, P. Pavka, G.T. Lim, F. Wolff-Fabris, J.E. Puskas, V. Altstädt;

Long-term Fatigue Performance of Biocompatible Polyisobutylene-based Nanocomposites; 26th Annual Meeting of the Polymer Processing Society; Banff, Canada (Juli 2010)

C. Götz, F. Fischer, P. Pavka, G.T. Lim, J.E. Puskas, V. Altstädt;

Long-term Fatigue and Dynamic Creep Performance of Dendritic Polyisobutylene-based Nanocomposites for Biomedical Devices;

European Conference on Composite Materials; Budapest, Ungarn (Juni 2010)

G.T. Lim, S.E. Porosky, C. Götz, V. Altstädt, J.E. Puskas;

Novel Translucent/Transparent Thermoplastic Elastomeric Nanocomposites for Breast Prosthesis; Annual Meeting of the Society For Biomaterials; Seattle, WA, USA (April 2010)

C. Götz, V. Altstädt;

Electrets used as Functional Materials;

1. International Workshop on Novel developments and Applications in Sensor Technology; Coburg (September 2009)

G.T. Lim, E. Foreman-Orlowski, P. Pavka, C. Goetz, V. Altstädt, J. E. Puskas;

Novel High Temperature Styrenic TPE Nanocomposites;

175th Technical Meeting of the Rubber Division of the American Chemical Society, Inc.; Louisville, KY, USA (October 2008)

C. Götz, F. Fischer, M. El Fray, M. Piatek, G.T. Lim, V. Altstädt;

Dynamic Creep and Fatigue Performance of Thermoplastic Elastomers as Biomaterials;

24th Annual Meeting of the Polymer Processing Society; Salerno, Italy (June 2008)

Poster Sessions on National and Internationals Conferences

U. Handge, C. Sailer, H. Steininger, G.H. Michler, C. Götz, F. Fischer, G.T. Lim, V. Altstädt; **Mechanical and Fatigue Crack Propagation Properties of Reactively Compatibilized Blends of Polyamide 6 and Styrenic Polymers;**

12. Problemseminar "Deformation und Bruchverhalten von Kunststoffen";
Merseburg (2009)

U. Handge, C. Sailer, H. Steininger, G.H. Michler, C. Götz, F. Fischer, G.T. Lim, V. Altstädt, **Micromechanical Processes and Fatigue Behaviour of Compatibilized PA 6 / ABS Blends;**
DGM-Verbundwerkstoffe, 17. Symposium Verbundwerkstoffe und Werkstoffverbunde; Bayreuth (2009)

P. Pavka, C. Götz, G.T. Lim, U.A. Handge, J.E. Puskas, V. Altstädt; **Effect of Architecture on the Fatigue Properties of SIBS Biomaterials;**
Ohio Innovation Summit 2009; Dayton, Ohio, USA (April 2009)

C. Götz, U.A. Handge, M. Piatek, M. El Fray, V. Altstädt; **Influence of E-Beam Irradiation on Poly(aliphatic/aromatic-ester) Multiblock Copolymers Used as Biomaterials;**
International Rubber Conference 2009; Nürnberg (June 2009)